Spatial and Temporal Analysis of Water Siltation Caused by Artisanal Small-scale Gold Mining in the Tapajós Water Basin, Brazilian Amazon: An Optics and Remote Sensing Approach

by

Felipe de Lucia Lobo
B.Sc., Universidade de São Paulo (USP), 2007
M.Sc., Instituto Nacional de Pesquisas Espaciais (INPE), 2009

A Dissertation Submitted in Partial Fulfillment
of the Requirements for the Degree of

DOCTOR OF PHILOSOPHY

in the Department of Geography

© Felipe de Lucia Lobo, 2015
University of Victoria

All rights reserved. This dissertation may not be reproduced in whole or in part,
by photocopy or other means, without the permission of the author.

Supervisory Committee

Spatial and Temporal Analysis of Water Siltation Caused by
Artisanal Small-scale Gold Mining in the Tapajós Water Basin, Brazilian Amazon:
An Optics and Remote Sensing Approach

by

Felipe de Lucia Lobo
B.Sc., Universidade de São Paulo (USP), 2007
M.Sc., Instituto Nacional de Pesquisas Espaciais (INPE), 2009

Supervisory Committee

Dr. Maycira P. F. Costa (Department of Geography)
Supervisor

Dr. Frederick J. Wrona (Department of Geography)
Departmental Member

Dr. Kevin Telmer (School of Earth and Ocean Sciences)
Outside Member

Abstract

Supervisory Committee

Dr. Maycira P. F. Costa (Department of Geography)
Supervisor

Dr. Frederick J. Wrona (Department of Geography)
Departmental Member

Dr. Kevin Telmer (School of Earth and Ocean Sciences)
Outside Member

The main goal of this research was to investigate the spatial and temporal impacts of water siltation caused by Artisanal Small-scale Gold Mining (ASGM) on the underwater light field of the Tapajós River and its main tributaries (Jamanxim, Novo, Tocantinzinho, and Crepori rivers). In order to accomplish this, two fieldwork research trips were undertaken to collect data associated with water quality and radiometric data. This data provided information to quantify the underwater light field in water affected by a gradient of mining tailings intensity, clustered into five major classes ranging from 0 to 120 mg/L of total suspended solids (TSS) (Chapter 3). In general, with increased TSS from mining operations such as in the Crepori, Tocantinzinho, and Novo rivers, the scattering process prevails over absorption coefficient and, at sub-surface, scalar irradiance is reduced, resulting in a shallower euphotic zone where green and red wavelengths dominate. The effects of light reduction on the phytoplankton community was not clearly observed, which may be attributed to a low number of samples for proper comparison between impacted and non-impacted tributaries and/or to general low phytoplankton productivity in all upstream tributaries.

In Chapter 4, aiming to extend the information derived from Chapter 3 over a 40-year period (1973-2012), the TSS concentration along the Tapajós River and its main tributaries was quantified based on *in situ* data and historical Landsat-MSS/TM/OLI data. Measurements of radiometric data were used to calibrate satellite atmospheric correction and establish an empirical relationship with TSS. The regression estimates TSS with high confidence from surface reflectance ($\rho_{\mathrm{surf}}(red)$) up to 25%, which corresponds to

approximately 110 mg.L^{-1}. The combination of the atmospheric correction and the robust reflectance-based TSS model allowed estimation of TSS in the Tapajós River from the historical Landsat database (40 years).

In Chapter 5, the role of the temporal changes of ASGM area in the water siltation over the last 40 years was investigated in four sub-basins: the Crepori, Novo, and Tocantins sub-basins (mined); and the Jamanxim sub-basin (non-mined), considering the landscape characteristics such as soil type and proximity to drainage system. ASGM areas were mapped for five annual dates (1973, 1984, 1993, 2001, and 2012) based on Landsat satellite images. Results showed that ASGM increased from 15.4 km^2 in 1973, to 166.3 and 261.7 km^2 in 1993 and 2012, respectively. The effects of ASGM areas on water siltation depends on several factors regarding ASGM activities, such as the type of mining, type of gold deposits, and intensity of gold mining, represented by number of miners and gold production.

Table of Contents

List of Tables

List of Figures

Acknowledgments

First of all, I am very thankful to my supervisor, Dr. Maycira Costa, for giving me the opportunity to pursue the long sought dream of a doctorate degree in a foreign country. Thank you for your patience, wisdom and determination. Also, this project would not happened without the contribution, tutoring and co-supervision of Dr. Evlyn Novo, who has guided me on the research career for the last eight years, and the experience of Kevin Telmer with ASGM. Thank you so much.

I would also like to thank all my lab mates (both Stephens, Tyson, Justin, Jeane, Adriana, Eddie), with whom I have shared not only scientific knowledge, but also amazing moments. Special acknowledgment to Dr. Thiago Silva, for helping me on the immigration process and being a great example of PhD Student. I would like to thank all faculty and staff members of the Department of Geography, in special to, Darlene for academic instructions, and Diane, for great English revisions. I am very grateful to those who helped me in the fieldworks specially Joaquim (INPE), and Haroldo Marques (ICMBio). Thank you so much, Haroldo, for the hard work in the Tapajós. I am also grateful to Dr. Vera Huszar for phytplankton analysis. A very special thank you for my mother, Mariangela. The most amazing person that encouraged and supported me in all endeavours of my life. A very very special thank you for my partner, Lauren Pansegrouw, whom have encouraged with her patience, care, and love.

Funding for Felipe Lobo has been provided by Science Without Borders (Brazilian Council for Scientific and Technological Development (CNPq) (237930/2012-9). Fieldwork supported by FAPESP (Brazil, Process 2011/23594-8). In addition, NSERC (Canada) grant to Dr. Maycira Costa for research development and lab analysis.

Thesis objective

The motivation for this research was the lack of detailed information about the temporal and spatial effects of ASGM on the in-water light field of impacted rivers. Specifically, ASGM has occurred in the Brazilian Amazon for many years, affecting aquatic systems with the use of methods that are destructive to the river systems with little or no remediation undertaken. In the Tapajós Region, most research regarding the effects of ASGM has focused on mercury contamination, which has caught the world's attention due to extreme social and environmental impacts. At present, little is known about the spatial and temporal consequences of water siltation caused by ASGM activities to aquatic communities, river navigation, and tourism in the Amazon.

In order to address some of the knowledge gap about ASGM impacts on aquatic systems, the main goal of this research was to investigate the spatial and temporal optical impacts of water siltation derived from ASGM in the Tapajós River Basin and main tributaries. More specifically, three objectives can be drawn:

i) Quantify the spectral changes caused by ASGM on the underwater light field in the Tapajós River Basin and main tributaries based on *in situ* measurements of optical and suspended solids data. In addition, investigate whether the spectral optical changes affect phytoplankton biovolume and diversity aiming to understand the effects of water siltation on primary production (Chapter 3).

ii) Quantify the TSS concentration along the Tapajós River and its main tributaries based on *in situ* data and historical Landsat-MSS/TM/OLI data aiming to extend the information derived from Objective (i) over a 40-year period (1973-2012) (Chapter 4).

iii) Define the temporal changes of ASGM area over the past 40 years in four sub-basins – Crepori, Novo, and Tocantins (mined); and the Jamanxim sub-basin (non-mined) – aiming to examine the role of ASGM areas on the water siltation observed in the previous chapters. Specifically, map ASGM areas for five annual dates (1973, 1984, 1993, 2001, and 2012) based on Landsat satellite images, and investigate the source of mining tailings considering landscape characteristics such as soil type and proximity to drainage system (Chapter 5).

Thesis structure

The document is organized into six chapters, with chapters 3 to 5 addressing the specific objectives (i) to (iii), respectively (as stated above). Each of these three chapters corresponds to a published or submitted peer-reviewed journal article.

Chapter 1 introduces the subjects related to the investigation of impacts of water siltation caused by ASGM, including a description of ASGM, environmental effects (i.e., the optical changes and their consequences to the aquatic systems), and introduces how the sediment plume can be monitored with the use of remote sensing data. Chapter 2 describes the Study Area with information concerning the biogeochemistry of the water basin, information about the history of ASGM and main mining techniques applied in this region. Lastly, Chapter 6 presents specific and general conclusions regarding the outcomes of the present study.

Chapter 1 – Introduction

1.1 Artisanal and Small-scale Gold Mining

Artisanal and Small-scale Gold Mining (ASGM) refers to the mining using rudimentary technology practised by individuals, groups, or communities. In the past 200 years, two main gold rushes of ASGM have occurred in the world. The first gold rush occurred over a time-span of 80 years (1849 to 1929), mostly in the British Colonies (USA, Canada, Australia, and South Africa). In these countries, the government extensively supported ASGM, as it was part of their social-economic development. The modern global gold rush started in 1970 with a peak in 1980 (Telmer and Persaud, 2013). Unlike the first gold rush, the modern gold rush is taking place in at least 70 countries, mostly developing countries, where ASGM is marginalized or not officially supported by the local governments, and thus contributing less to local development than in the countries involved in the 19th century rush (Veiga, 1997; Sousa and Veiga, 2009; Telmer and Stapper, 2007).

Currently, ASGM activities may fluctuate with variations in gold commodity prices (Telmer, 2013). For example, in the Amazon, substantial ASGM activities started small in the 1950s at only a few sites, called 'garimpos.' The mining activities increased during the 1970s due to a combination of increasingly efficient low-budget techniques and the rise of the price of gold (adjusted to inflation) to US $2100/oz in 1980 (Araújo Neto, 2009). The gold mining activities, however, decreased during the late 1990s and early 2000s due to a reduction in the gold price (US $330/oz). Today, hundreds of thousands of people are directly involved in ASGM in the Amazon Basin because of the relatively high gold price (US $668/oz) (Sousa and Veiga, 2009; Silva, 2012; Fernandes *et al.*,

2014). In Brazil today, ASGM gold production is responsible for approximately 40 tonnes per year, or about 10% of the world ASGM production (Telmer and Veiga, 2009), of which nearly 26% is produced in the Tapajós River Basin by approximately 50,000 miners distributed in more than 300 mining sites (CPRM, 2009; Araújo Neto, 2009; Silva, 2012; Fernandes *et al.*, 2014). ASGM activity provides income for an extensive chain that includes not only miners, but also security, retail merchants, gold shops, gold refiners, financiers, and many other service providers. Estimation of the secondary economy related to ASGM is five times the value of the gold produced, which represents about 100 billion dollars in 2012 worldwide (Telmer and Persaud, 2013).

1.2 Environmental impacts

Despite its contribution to local economies, modern ASGM is often carried out informally and is associated with a range of negative social and environmental impacts. Migration, family abandonment, substance abuse, sex trade, and child labour are among the social impacts (Telmer and Persaud, 2013; Fernandes *et al.*, 2014). The main environmental impacts include water pollution, deforestation, and mercury contamination (Sousa and Veiga, 2009).

Several studies have reported adverse changes in the aquatic environment due to ASGM activities (Davies-Colley *et al.*, 1992; Mol and Ouboter, 2004). Besides mercury contamination, which is very well documented (Rodrigues *et al.*, 1994; Veiga, 1997; Telmer and Veiga, 2009), artisanal gold mining can cause contamination by cyanide, which is used as a leaching reagent in the production process (Rodrigues *et al.*, 1994). In addition, the gold production process leads to increased water siltation, leading to

geomorphological alterations and biodiversity reduction (Castilla, 1983; Mol and Ouboter, 2004). As the miners exploit a particular area of the alluvial plain, new pits open and the mining tailings (water + sediment) is usually discharged back into the river drainage, or to adjacent small ponds/lakes. In those cases, water siltation is caused not only during mining operations, but also after the mining operation ends as the mining tailings left behind can be transported into the rivers and increase water siltation (Sousa and Veiga, 2009). The discharge of sediment into the water has severe impacts on the water quality, such as decreasing light availability for primary production (Roland and Esteves, 1998; Guenther and Bozelli, 2004; Davies-Colley *et al.*, 1992), and changing benthic (Tudesque *et al.*, 2012) and fish communities (Mol and Ouboter, 2004). In the Brazilian Amazon, for example, sediments from mining tailings in streams and rivers may vary between 1 and 2 tonnes per gram of gold produced (Sousa and Veiga, 2009). Such practices likely have a significant impact on water systems, considering that ASGM gold production in the Brazilian Amazon reaches an average of 50 tonnes annually (Araújo Neto, 2009).

1.3 Underwater light field and remote sensing

One of the effects of water siltation is light attenuation by suspended particles, which can directly affect phytoplankton productivity by limiting underwater Photosynthetic Available Radiation (PAR), and indirectly leads to environmental imbalance and biodiversity change in rivers impacted by gold mining (Tudesque *et al.*, 2012). Specifically in the Amazon Basin, a major decrease in phytoplankton density has been documented in the Batata Lake as a consequence of sediment plume derived from

mining activities (Roland and Esteves, 1998). Additionally, Guenther and Bozelli (2004), studying the same system, suggested that this decrease in phytoplankton densities might be related to a decrease in growth rates caused by light attenuation; other factors such as nutrient availability and phytoplankton grazing (top-down) were not considered in the analysis.

The underwater light field available for photosynthesis, estimated by E_o, is primarily controlled by the absorption and scattering coefficients (Inherent Optical Properties, IOPs) of the major optically active components in the water, such as algal particles (estimated by *chl-a* concentration), non-algal particles or *tripton* (estimated by TSS concentration), and dissolved organic matters (commonly *CDOM*) (Mobley *et al.*, 2002; Kirk, 2011). Given the scattering nature of inorganic matter such as fine inorganic particles *(tripton)* (Mobley *et al.*, 2002; Kirk, 2011; Lobo *et al.*, 2014), the input of such material reduces light penetration and increases the back-scattering coefficient (Figure 1.1).

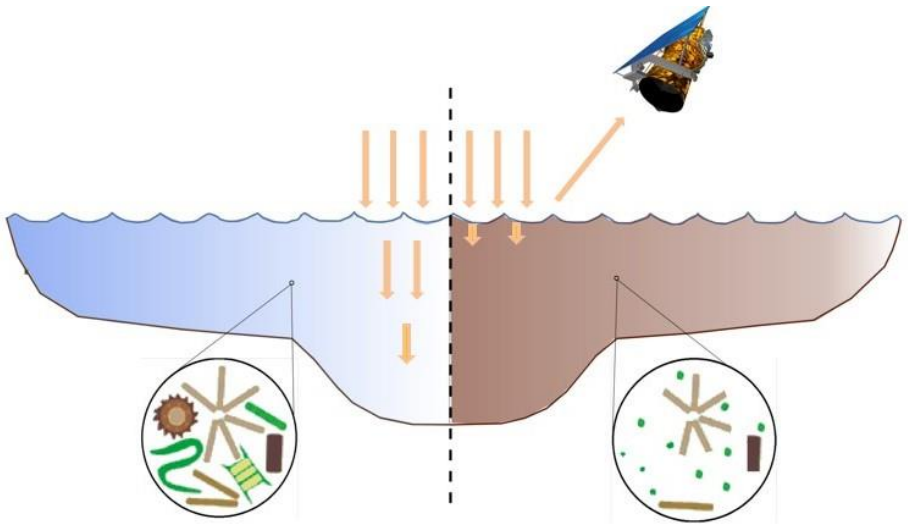

Figure 1.1: Schematic representation of optical changes caused by water siltation. In clear waters (left), incoming light penetrates deeper layers when compared to turbid

waters. In turbid waters (right), part of the light attenuated is reflected back to remote sensors enabling detection of the sediment plume. This light attenuation can possibly cause reduction of phytoplankton biovolume and diversity.

While some evidence shows the impacts of mining tailings on underwater light (Roland and Esteves, 1998; Guenther and Bozelli, 2004), the data on changes in the spectral underwater light field in Amazonian waters is still lacking. Understanding the underwater light field, more specifically the total scalar irradiance, E_o, is important. Firstly, because it informs the total energy available for photosynthesis in a hyperspectral interval between 400 and 700 nm. Knowing the spectral distribution of the light field allows for spectral analysis on specific phytoplankton absorption efficiency (Markager and Vincent, 2001). Secondly, knowing the total scalar irradiance also allows for the description of bio-optical parameters that can be used in remote sensing approaches to retrieve water quality parameters from satellite images for monitoring purposes (Pahlevan and Schott, 2013; Li *et al.*, 2013; Odermatt *et al.*, 2012).

The Landsat family (MSS, TM, and ETM+), for example, have been effectively used to estimate total suspended solids (TSS) in coastal and inland waters (Harrington Jr. *et al.*, 1992; Binding *et al.*, 2005). Detection of water leaving radiance from turbid waters with high confidence is possible, first because the sensor's spatial resolution (up to 80m on MSS) allows imaging rivers and estuarine areas, and second because of the signal-to-noise ratio of these sensors (250:1) (Dekker *et al.*, 2002). Studies showed that green and red bands correlate well with TSS up to approximately 100 mg/l (Dekker *et al.*, 2002; Binding *et al.*, 2005). Under higher concentrations, however, these bands saturate and NIR bands present a better predictor of TSS (Wang *et al.*, 2009; Doxaran *et al.*, 2012).

Given the recently launched OLI (Operational Land Imager) sensor on board Landsat-8, with similar characteristics of a TM sensor, the capability of using time series based on Landsat imagery for evaluation of temporal changes and monitoring purposes is extended to the present; a time series of at least 40 years (1973 to present) of Landsat imagery is currently available. However, given differences in the sensor's resolution and in atmospheric conditions at the time of imagery acquisition, a proper comparison between water leaving radiance requires accurate atmospheric effects and inter-image normalization or reference targets (Hadjimitsis and Clayton, 2009).

Chapter 2 – Study area

2.1 Biogeochemistry of the Tapajós River Basin

The lower section of the Tapajós River Basin covers about 130,370 km^2 (Figure 2.1) and drains mostly lixiviated Pre-Cambrian rocks, which results in waters that are transparent/greenish in colour with low amounts of suspended solids, and are generally called ‘clearwaters’ by the research community (Sioli, 1984; Junk, 1997). The river basin can be generally separated into two geomorphological sections: the upstream riverine section (lotic system), from the headwaters down to the Aveiro City region; and the downstream section (semi-lentic system), from Aveiro City to the mouth of the river where it merges with the Amazon at Santarém City (Figure 2.1).

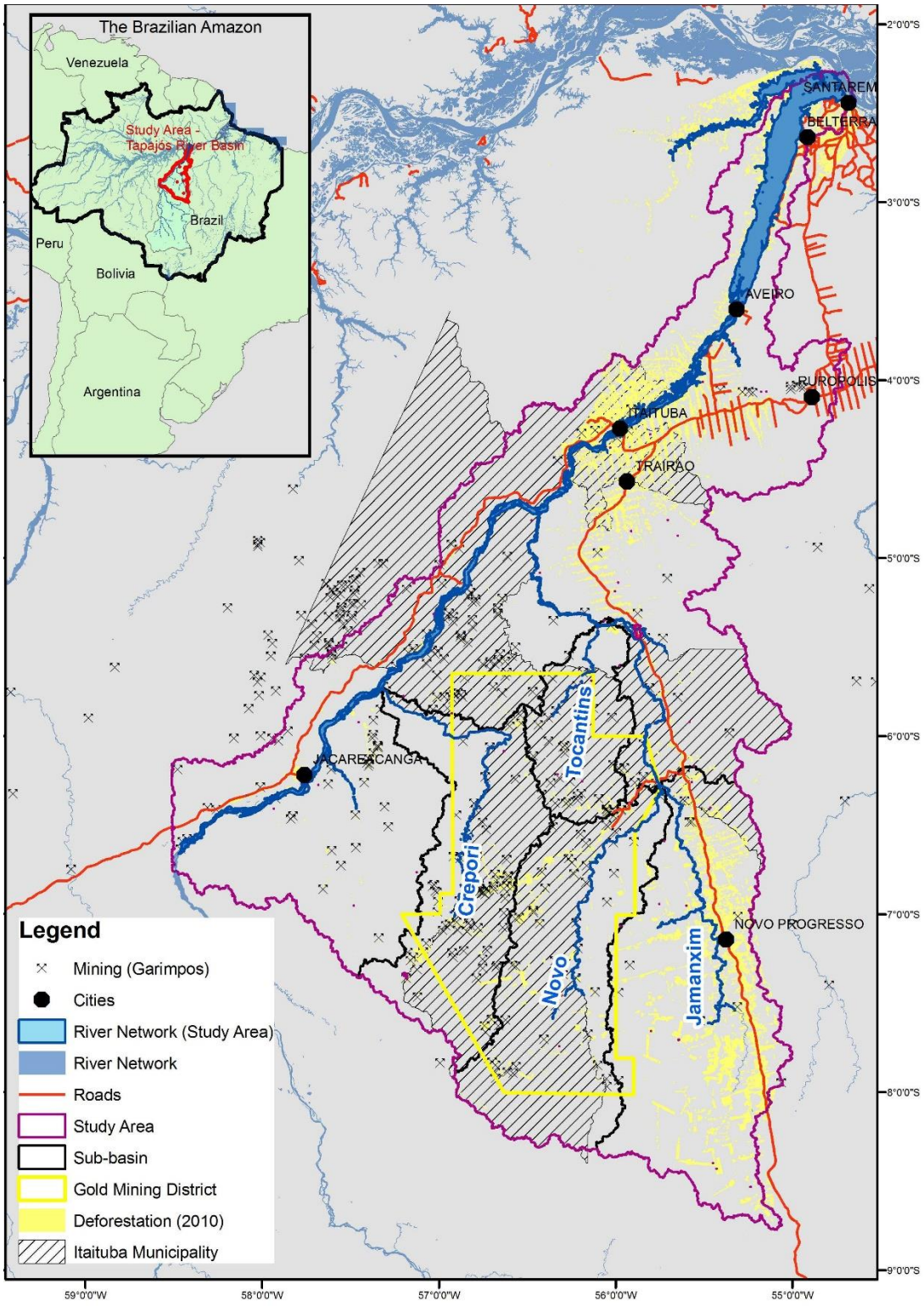

Figure 2.1: Location of the Study Area within the Tapajós River Basin in the Brazilian Amazon showing the main cities, Itaituba Municipality, main tributaries, deforestation (INPE, 2011), gold-mining district, and mines (CPRM, 2009).

The downstream river section is fairly wide (10-15 km) with low water velocity, creating a semi-lacustrine condition, which can support planktonic growth. Chlorophyll-*a* (*chl-a*) concentrations vary from 5.0 to 25.1 $\mu g.L^{-1}$ (Rudorff *et al.*, 2009a; Novo *et al.*, 2006a), and cyanobacteria blooms occur as a consequence of urban-derived diffuse nutrient inputs at the margins of the Tapajós River mouth at Santarém (Sá *et al.*, 2010).

Along with phyplankton, suspended sediments in the downstream section are composed primarily of terrestrial fine particulate matter discharged from upstream (Roulet *et al.*, 2001; Farella *et al.*, 2001; Gibbs, 1967). The biogeochemistry and optical data from the downstream region have been recently reported by Costa *et al.* (2013), showing TSS concentrations up to 4.1 $mg.L^{-1}$ during rising and receding water levels. The authors also reported average absorption by a_{cdom} (440nm) to be relatively lower (3.2 m^{-1}) than values measured in Amazonian black water rivers (8.6 m^{-1}), for example. As a result of the natural clear water conditions of the downstream section of the Tapajós River, the diffuse attenuation coefficient (K_d *PAR*) is around 2.0 m^{-1} in both rising and falling periods, whereas for black and white waters, K_d increases to 3.7 and 5.1 m^{-1}, respectively (Costa *et al.*, 2013).

It is worth stating that most of the research reported has taken place in the downstream section of the Tapajós River, called the Tapajós Lake (Costa *et al.*, 2013; Roulet *et al.*, 1998; Seyler and Boaventura, 2003; Rudorff *et al.*, 2009a), with little information about the biogeochemistry (Roulet *et al.*, 2001; Telmer *et al.*, 2006) and the hydrological optics of the upstream section of the river. As opposed to the semi-lentic conditions of the Tapajós Lake section, the upstream section starting from Aveiro City (Figure 2.1) is narrower (2-4 km), with a strong advection current (Farella *et al.*, 2001). In

such systems, plankton development is likely suppressed by the low residence time and turbulence of running waters (Reynolds, 2006). As a result, the suspended sediment content is composed mostly of allochthonous matter, such as quartz, plant debris, and clay clusters, rather than autochthonous matter (Roulet *et al.*, 1998; Bernardes *et al.*, 2004). Water that reaches the downstream section is mostly composed of fine particles represented by kaolinite (varying from 70-90%), and the coarse fraction (2-20 μm) is composed mostly of quartz (Guyot *et al.*, 2007).

Consistent with the precipitation regime in the western Pará State, which has a rainy season from November to April, the upstream river basin is subjected to a flood pulse with strong influence on the biochemical cycles and land/water interactions (Junk, 1997). At the Itaituba ANA station, the highest water level (8.0 m) occurs at the end of the rainy season (March-May), when water flow and average velocity reaches 22,822 $m^3.s^{-1}$ and 1.15 $m.s^{-1}$, respectively. On the other hand, from September to November the water level drops to 4.5 m, and the flow decreases to 5,054 $m^3.s^{-1}$ with average velocity of 0.55 $m.s^{-1}$ (ANA, 2013).

2.2 Small-scale Gold Mining in the Tapajós Region

The first mining activities recorded in this region date from 1958, when alluvial gold deposits were discovered in the Tropas and the Crepori rivers, attracting thousands of miners (‘garimpeiros’) to the Tapajós River Basin. During the 1960s, ASGM was rudimentary, based on manual efforts, without any mechanization (Nery and Silva, 2002). In 1978, mechanization was introduced when miners started using dredges, mostly in the Tapajós and large tributaries. In the case of rafts and dredges, the exploitation occurs in

active riverbeds with the use of pumps (Telmer *et al.*, 2006). The rafts remove material from the bottom using a suction hose with a caliber of about 25 cm. These activities occur at the margins of the rivers, causing severe water siltation levels due to the discarded material going back into the rivers (Figure 2.2a and b).

a) 

b) 

c) 

d) 

e) 

f) 

Figure 2.2: Methods of ASGM in the Tapajós region. Rafts or dredges (a) use a motor pump for suction of the sediment from the bottom of the rivers (image source: Silva, 2012). This practice releases high volumes of suspended sediment into the waters after passing through sluice boxes (b) (image source: http://oglobo/brasil/.../ rio-tapajos-8710538). The water-jet systems (c and d) use two sets of pumps and hoses, one to dislodge the topsoil, and the second to create the suction of the sediment to the sluice boxes. Currently, several working pit-loaders are being used in the Tapajós region (d), which increases the capacity of sediment processing (images c and d by Oldair Lamarque). In the case of mining the primary deposits, the use of high mechanization such as hammer mills is often reported (e). Recently, the use by medium-sized companies of cyanide for amalgamation of gold has increased in the Tapajós region (f) (image source: Silva, 2012).

In the 1980s, colluvial ore deposits were discovered and exploitation began with water-jet systems (Rodrigues *et al.*, 1994). This approach requires two water-jet motors, one to remove the overburden, and the second to suck the gravel (Figure 2.2c and d). The advent of this efficient, low-budget technique, associated with the rise in the price of gold in 1980, resulted in a boom of the mining population, which reached approximately 150,000 in 1989 (Rodrigues *et al.*, 1994), with gold production of approximately 25 tonnes a year. During this decade, more than 400 airstrips and over 600 mining sites (‘garimpos’) were reported (Rodrigues *et al.*, 1994). The gold rush in Tapajós made the Brazilian government create the ‘Gold Mining Reserve’ in 1983, along with other policies to support local miners and to reduce socio-environmental impacts, with no satisfactory results (Fernandes *et al.*, 2014). The ASGM boom during the 1980s is notorious for severe environmental impacts, including mercury contamination and water quality degradation, not to mention below-standard working conditions and social impacts (Fernandes *et al.*, 2014).

In the late 1990s, ASGM decreased drastically, mainly discouraged by the low price of gold and the exhaustion of easy-access alluvial gold deposits. Consequently, gold production reduced gradually to approximately 10 tonnes per year in 2000. Parallel to these developments, primary gold mineralization was discovered in 1998, attracting international mining companies to initiate exploitation of 'quartz vein' deposits (Silva, 2012). At this point, a clarification of the definition of primary and secondary gold is necessary. Whereas primary gold is associated with igneous and intrusive metamorphic rocks (indicated by the geological formation), secondary gold is associated with alluvial deposits along rivers, derived either from natural transportation or from mining tailings (Nery and Silva, 2002). To exploit primary deposits, mining companies usually apply highly mechanized methods such as the use of trucks and pit-loaders to transport the material to hammer-mills (Figure 2.2e), where the rocks are broken down into finer material. This material is then transported to large tanks where the amalgamation of gold using cyanide occurs (Figure 2.2f).

Currently, more than 300 small-scale mines with participation of more than 50,000 miners produce gold within three main sub-basins: the Novo, the Crepori, and the Tocantinzinho (abbreviated to Tocantins) (see Figure 2.1for locations). Recent investments by gold mining companies and local miners have introduced more than 50 pit-loaders in the region, increasing the capacity for mineral processing compared to water-jet systems, and potentially increasing the discharge of mining tailings into the rivers as well (Silva, 2012; ICMBIO, 2010).

The sediment plume generated during small-scale mining operations is composed mostly of fine inorganic particles (TSS up to 300 $mg.L^{-1}$) that can carry significant

amounts of mercury and are mostly discharged into the rivers. The grain size of tailings varies from coarse (2 mm) to as fine as clay (<0.002 mm), indicating that this fine and light sediment can be carried for long distances in the rivers (Telmer *et al.*, 2006).

Chapter 3 – Effects of Artisanal Small-scale Gold Mining tailings on the underwater light field in the Tapajós River Basin[1]

[1] To be submitted to *Limnology and Oceanography*

3.1 Abstract

Currently, due to high gold prices in the market, approximately 16 million people are directly involved with ASGM throughout the world. Despite its contribution to local economies, ASGM has severe socio-environmental impacts such as violence, mercury contamination, and water siltation, but little is known about their impacts on local communities, and water quality. In order to fill the gap of knowledge related to ASGM impacts on water quality, this paper investigates the effects of water siltation on the underwater light field of various tributaries of the Tapajós River Basin, and its consequences to the phytoplankton community. Two field campaigns were conducted in the Tapajós River Basin to measure IOPs, AOPs, and biogeochemical data in March/April 2011 during high water level (27 sample points) and September 2012 during low water level (13 sample points). Results showed that the inorganic nature of mine tailings is the main factor affecting the underwater scalar irradiance in the Tapajós River Basin. The TSS concentration varies seasonally during the year in a synergism between water level and mining activities: during low water level, mining activities intensify and, associated with low water volume, TSS rapidly increases, which in turn changes the optical characteristics of the water. For waters with low or no influence from mine tailings, light absorption dominates over scattering. With increased TSS loadings from mining operations, the scattering process prevails over absorption coefficient and, at sub-surface, scalar irradiance is reduced, resulting in a shallower euphotic zone, and green and red wavelengths dominate. Based on the match between the available PAR and specific absorption, we demonstrated that cyanobacteria (*Synechocystis sp*.) could be more efficient at absorbing the available spectral light in both impacted and non-impacted waters in comparison to diatoms (*Chaetoceros sp.*). However, the dominance of diatoms in the tributaries suggests that the spatial and temporal distribution of phytoplankton in the Tapajós River Basin is not simply a function of light availability, but rather depends

on a synergism of factors including flood pulse, water velocity, seasonal variation of incoming irradiance, and nutrient availability.

3.2 Introduction

The increase in the price of gold over the past 10 years has stimulated small-scale gold mining in Africa, Asia, and South America, resulting in an annual production of around 400 tonnes of gold by approximately 16 million miners (Seccatore, 2014). Despite the contribution of approximately 10% of total global gold production (Veiga, 1997), artisanal gold mining has many negative social and environmental impacts (Grätz, 2009). Mercury contamination (Telmer and Veiga, 2009; Nevado *et al.*, 2010; Dorea and Barbosa, 2007), geomorphological changes (Rodrigues *et al.*, 1994), and water siltation are among the main direct impacts of small-scale gold mining (Dambacher *et al.*, 2007).

Water siltation caused by gold mining is commonly reported throughout the world (Asia, Africa, and South America) (Mol and Ouboter, 2004) because most of the mining activities take place in rivers or at their margins. In the Brazilian Amazon, for example, sediments from mining tailings in streams and rivers may vary between 1 and 2 tonnes per gram of gold produced (Sousa and Veiga, 2009). Such practices likely have a remarkable impact on water systems, considering that ASGM gold production in the Brazilian Amazon reaches an average of 50 tonnes annually (Araújo Neto, 2009).

One of the effects of water siltation is light attenuation by suspended particles, which can directly affect phytoplankton productivity by limiting Photosynthetic Available Radiation (PAR), and indirectly leads to environmental imbalance and biodiversity change in rivers impacted by gold mining (Tudesque *et al.*, 2012). Specifically in the Amazon Basin, a major decrease in phytoplankton density has been

documented in the Batata Lake as a consequence of an increase in suspended matter due to mining activity (Roland and Esteves, 1998). Additionally, (Guenther and Bozelli, 2004), studying the same environment, suggested that this decrease in phytoplankton densities might be related to a decrease in growth rates caused by light attenuation. Moreover, Tudesque *et al.* (2012) have reported changes in the phytoplankton community with a rise in the proportion of benthic diatoms with mobility capacity due to an increase in water siltation in streams impacted by small-scale gold mining in French-Guiana.

While some studies show the impacts on underwater light conditions caused by mining tailings (Roland and Esteves, 1998; Guenther and Bozelli, 2004), the quantification of the impact on the spectral underwater light field in Amazonian waters is still lacking. Quantifying the underwater light field, more specifically the total scalar irradiance, E_o, is important. Firstly, it informs the total energy available for photosynthesis in a hyperspectral interval between 400 and 700 nm. Knowing the spectral distribution of the light field allows for spectral analysis on specific phytoplankton absorption efficiency. For example, an underwater light field rich in blue-green light will favour phytoplankton with pigments that absorb light in the blue-green spectra (Markager and Vincent, 2001). Secondly, knowing the total scalar irradiance also allows for the description of bio-optical parameters that can be used in remote sensing approaches to retrieve water quality parameters from satellite images for monitoring purposes (Pahlevan and Schott, 2013; Li *et al.*, 2013; Odermatt *et al.*, 2012).

Considering the relevance of understanding the possible changes in the light field of waters impacted by gold mining tailings, and consequences to phytoplankton

communities diversity and specific absorption, the objectives of this study are to: 1) quantify the optical effects of sediment loading on the underwater light field along the Tapajós River Basin (Brazilian Amazon); 2) evaluate to what extent the characteristics of the light field and the light attenuation caused by water siltation impacts the characteristics of the phytoplankton communities and critical depth; 3) assess the absorption efficiency of two major phytoplankton groups (cyanobacteria and diatom) given the different *in situ* light conditions observed along the river network. To address these objectives, biogeochemical and *in situ* optical measurements including Inherent (IOPs) and Apparent Optical properties (AOPs) were collected during two field campaigns. The optical data was used to run and validate a radiative transfer model, Hydrolight, to compute E_o, which in turn was applied to assess the critical depth for photosynthesis, and the spectral absorption efficiency by specific cyanobacteria (*Synechocystis sp*) and diatoms (*Chaetoceros sp*). The analysis on absorption efficiency was conducted based on the assumption that *in situ* absorption by phytoplankton is a function of the *in situ* irradiance and the specific absorption coefficient of different phytoplankton groups (Markager and Vincent, 2001). The calculated *in situ* irradiance were combined with the specific absorption coefficients for cyanobacteria and diatoms reported by Bricaud *et al.* (1988). Despite the strong emphasis on underwater light conditions, this paper also provides a discussion on phytoplankton community and its distribution as a function of other important factors, such as hydrological regime, current velocity, depths, and nutrient concentration.

3.3 Methods

The methodological component of this study consisted of three major parts: 1) acquisition of *in situ* optical and biogeochemical data at high (2011) and low (2012) water levels; 2) calibration and validation of a bio-optical model, Hydrolight, to derive total scalar irradiance; 3) evaluation of critical depth for phytoplankton productivity based on E_o, and assessment of spectral absorption efficiency of two dominant groups, diatom and cyanobacteria, identified in this study. Figure 3.1 summarizes the different components of this research.

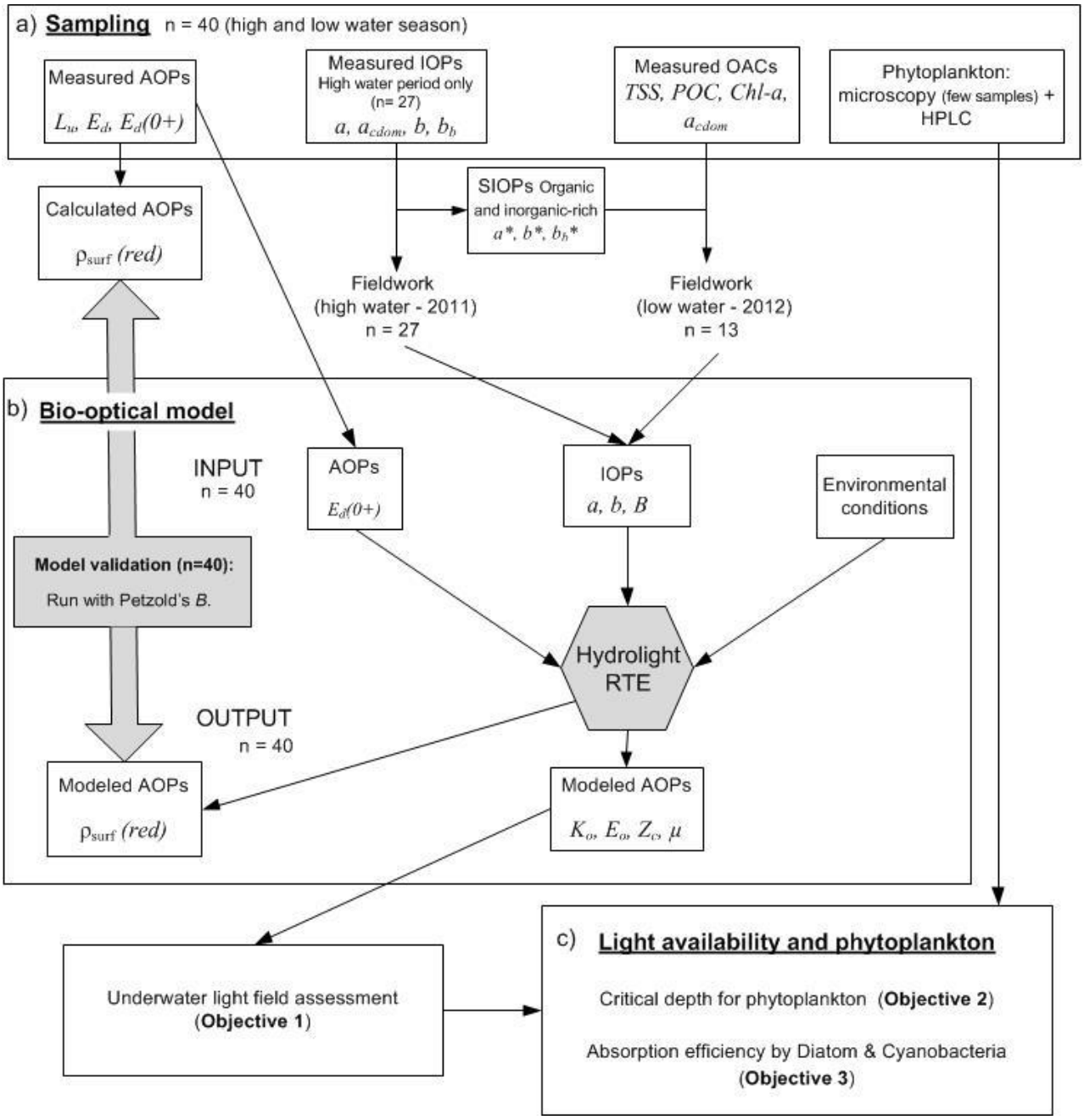

Figure 3.1: Flowchart of the methods comprises: a) field campaigns for optical properties and OAC (Optically Active Components) measurements; b) bio-optical model input including measured AOPs (Apparent Optical Properties), IOPs (Inherent Optical Properties; high water – 2011) and SIOPs (Specific IOPs; low water – 2012) for underwater light field quantification; c) assessment of light availability for phytoplankton, including critical depth and *in situ* absorption efficiency analyses. See Table 3.1 for definition of symbols.

3.3.1 Sampling

Two field campaigns were conducted in the Tapajós River Basin to measure IOPs, AOPs, and biogeochemical data in March/April 2011 during high water level (27 sample points) and September 2012 during low water level (13 sample points, no IOPs data due to loss of optical equipment in the Tapajós River at the beginning of the field work) (see Figure 3.2 for sample point locations). Locations of the sample points were defined in order to cover the spatial distribution along the Tapajós River and main tributaries, including mined (Crepori, Tocantins, and Novo) and non-mined tributaries (Jamanxim). As reference, IOPs of two non-mined (called pristine) small streams alongside the Crepori River were also sampled. Dense vegetation canopy prevented AOPs measurement in these streams.

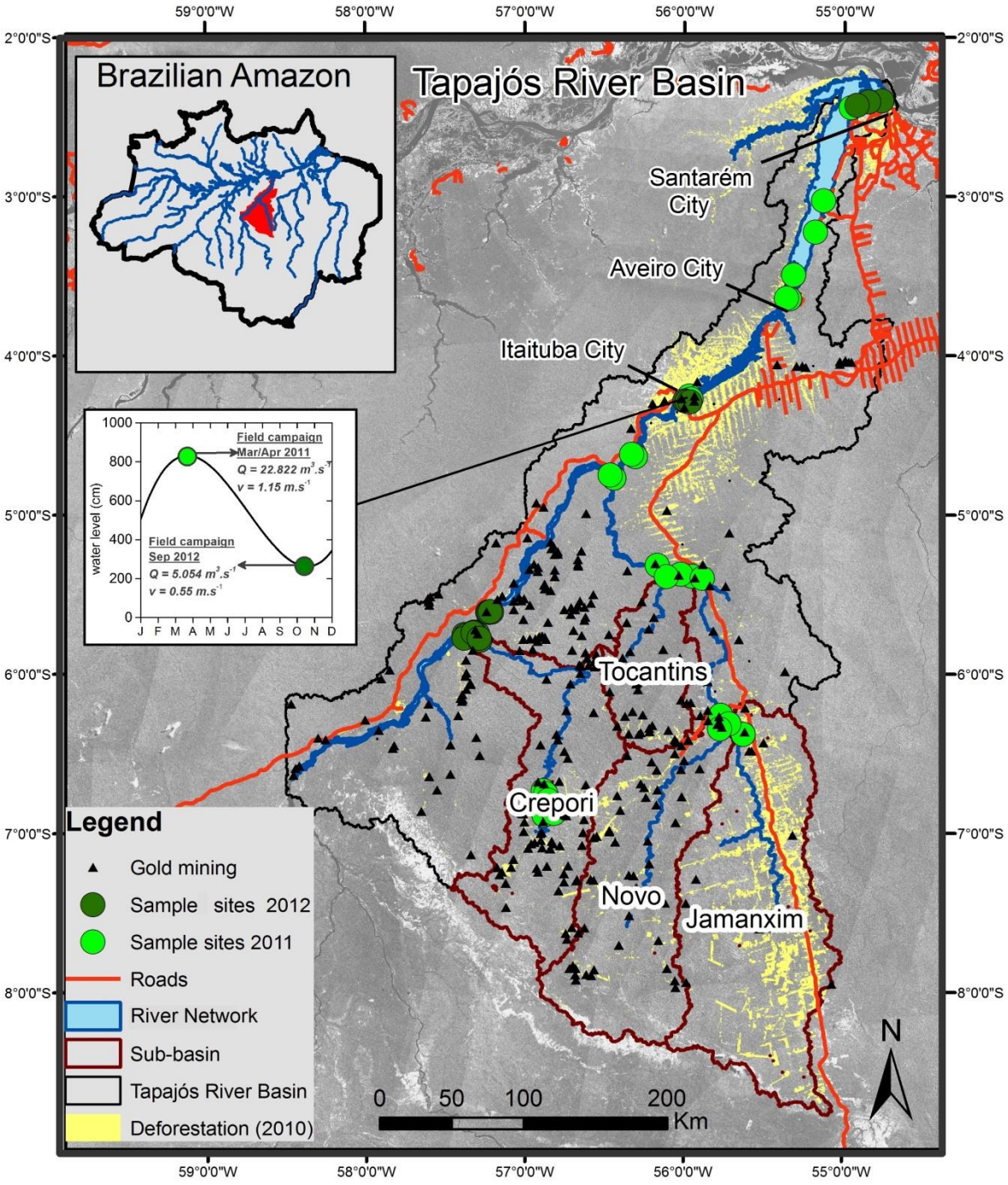

Figure 3.2: Location of the sample sites within the Tapajós River Basin taken during two field works: May, 2011 (High water level season); and September, 2012 (Low water level season). Background image: grey scale of Landsat GeoCover (https://zulu.ssc.nasa.gov/mrsid).

3.3.2 Biogeochemical data

For each sampled location (n=40), two water samples (at least 500 ml sampled volume) were taken at a depth of 0.3 m and at $Z_{1\%}$ (depth where downwelling irradiance reaches 1% of surface irradiance) to determine TSS concentrations according to the gravimetric method (APHA, 2005). The surface (0.3 m) and at $Z_{1\%}$ depths were chosen to cover the water column where phytoplankton productivity can occur at each sample site. For each water sample, triplicates of pre-weighed GF/F (0.7 μm) filters were preserved in the dark and cold until laboratory analysis. After TSS analysis, half of those filters were used for particulate organic carbon (POC) determination according to the high-temperature combustion method with TOC-V analyzer (Shimadzu Inc.) (Hansell, 2001). The other filters were used for determining the percentage of organic content by applying the Loss On Ignition (LOI) technique (APHA, 2005). Water samples were also filtered (500 ml) with GF/F (0.7 μm) for determination of *chl-a* and auxiliary pigments by HPLC (High-Performance Liquid Chromatography) (APHA, 2005). The pigments on the filters were extracted with acetone 90%, centrifuged, and processed in liquid chromatography (Dionex P680) analysis within 24 hours after extraction to avoid pigment degradation (Buchaca, 2004).

Discrete surface water samples were taken from a subset (n=15 including both campaigns) of the total sampled locations in mined and non-mined tributaries for quantitative and qualitative analyses of phytoplankton populations using the settling technique (Utermöhl, 1958). The units, corresponding to cells, colonies, and filaments, were enumerated to at least 100 specimens of the most frequent species at 400x magnification (Lund *et al.*, 1958). Specific phytoplankton biovolume (mm^3L^{-1}) was

estimated according to (Hillebrand *et al.*, 1999). Six water samples of approximately 200 ml each were taken along the two main rivers, Tapajós and Crepori, during the low water campaign for nutrient (nitrate and phosphate) determination (APHA, 2005).

3.3.3 Optical data

IOP measurements were only acquired during the high water level campaign (April, 2011, n = 27) because instruments (ac-S) were lost in the river at the beginning of the high water campaign. Total beam attenuation $c(\lambda)$ and total absorption $a(\lambda)$ coefficients were measured *in situ* with a WetLabs ac-S instrument at 80 wavelengths from 390 to 750 nm. Total beam attenuation coefficient $c(\lambda)$ is the sum of the total absorption $a(\lambda)$ and total scattering coefficient $b(\lambda)$. Absorption coefficient is defined as the sum of the absorption coefficients by water $a_w(\lambda)$, particulate material $a_p(\lambda)$, and coloured dissolved organic matter $a_{cdom}(\lambda)$. Similarly, the total scattering is the sum of its component scattering coefficient of water $b_w(\lambda)$ and particulate material $b_p(\lambda)$, with the general assumption that scattering due to CDOM is negligible (Mobley, 1994).

$$c(\lambda) = a(\lambda) + b(\lambda) \quad \text{(Eq. 3.1)}$$

$$a(\lambda) = a_w(\lambda) + a_{cdom}(\lambda) + a_p(\lambda) \quad \text{(Eq. 3.2)}$$

$$b(\lambda) = b_w(\lambda) + b_p(\lambda) \quad \text{(Eq. 3.3)}$$

The ac-S output was calibrated using ultra-clean water from the Barnstead E-pure water purification system before and after field campaigns to minimize measurement deviation caused by sensor transportation. The output was also corrected for temperature and for scattering in

the absorption tube using the manufacturer protocol (Wet Labs, 2013). The $a_{cdom}(\lambda)$ coefficient over PAR was acquired after filtering sampled water with a Pall 0.2 µm sterile

filter. Spectral measurements of the filtered water were taken *in situ* with the Ocean Optics UV-4000 equipment (Tilstone *et al.*, 2012). The measured absorbance was first corrected for blank offset measured with deionized water, and secondly converted to $a_{cdom}(\lambda)$ according to Kirk (2011). Attached in the same cage along with ac-S, the Environmental Characterization Optics-Backscattering (ECO-BB) by Wetlabs© measured particle backscattering ($b_{bp}(\lambda)$) at three wavelengths (470, 532, and 660 nm). For each wavelength, $b_{bp}(\lambda)$ was determined as follows:

$$b_{bp}(\lambda) = 2\pi . x . \beta_{bp}(117°) \qquad \text{(Eq. 3.4)}$$

where $b_{bp}(\lambda)$ is the particulate backscattering coefficient, β_b (117°, λ) is the volume scattering function for a specific angle (117°) and wavelength (λ), and x is 1.1 as determined by Boss and Pegau (2001).

AOPs were measured using two profiling Satlantic hyperspectral radiometers and one above-water hyperspectral radiometer during both field campaigns (n = 40). The radiometer HyperPro-3000 measures in-water downwelling irradiance ($E_d(0^-, \lambda)$) and upwelling radiance ($L_u(0^-, \lambda)$) *in situ*, as well as above-water downwelling surface irradiance ($E_d(0^+, \lambda)$) in the interval from 396 to 800 nm with a resolution of 10 nm. Radiometric data were processed using Satlantic's Prosoft (Satlantic, 2011). After being corrected and binned to depth intervals, $L_u(0^-, \lambda)$ values were then used to calculate upward irradiance $E_u(0^+, \lambda)$ as follows (Satlantic, 2011):

$$E_u(0^+, \lambda) = 4.5 \cdot L_u(0^-, \lambda) \cdot (1 - r(\lambda, \theta)/n_w^2(\lambda)) \qquad \text{(Eq. 3.5)}$$

where $r(\lambda, \theta)$ is reflective index (0.021) and n_w^2 is refractive index (1.34) (Mobley, 1994). Next, surface reflectance was calculated for each profile according to:

$$\rho_{surf}\ (\lambda) = E_u(0^+, \lambda)/E_d(0^+, \lambda) \quad \text{(Eq. 3.6)}$$

Further, diffuse attenuation coefficient $K_d\ (\lambda)$ was calculated as:

$$K_d(\lambda) = ln\ \left(\frac{E_d2(\lambda)}{E_d1(\lambda)}\right) \frac{1}{\Delta z} \quad \text{(Eq. 3.7)}$$

where $E_d2(\lambda)$ is the downwelling irradiance at depth 2, and $E_d1(\lambda)$ is the downwelling irradiance at depth 1, and Δz is the depth difference between these two measurements (Kirk, 2011). To normalize all the $K_d\ (\lambda)$ to the light conditions at the moment of measurements, downwelling irradiance above-surface ($E_d\ (0+)$) was used as $E_d1(\lambda)$ in the Eq. 3.7.

3.3.4 Bio-optical modeling and validation

To assess the quantity and quality (spectral distribution) of the light available for photosynthesis in an increasing TSS aquatic environment, underwater total scalar irradiance, $E_o\ (0^-,\lambda)$ (λ = 400-700 nm), is required because unlike measured $E_d\ (0^-,\lambda)$, which accounts for downwelling irradiance only, $E_o(0^-,\lambda)$ integrates radiances over all angles around a point underwater. Given that phytoplankton cells are able to utilize irradiance from all directions, $E_o(0^-,\lambda)$ is required for quantifying light availability for primary production (Kirk, 2011).

$$E_o(0^-, \lambda) = E_d\ (0^-, \lambda) + E_u(0^-, \lambda) \quad \text{(Eq. 3.8)}$$

where $E_u\ (0^-,\lambda)$ and $E_d\ (0^-,\lambda)$ are upwelling and downwelling scalar irradiance, respectively. $E_o(0^-,\lambda)$ is also needed to calculate the average cosine, $\bar{\mu}\ (PAR)$, which informs the prevailing light scattering angle and helps to describe the underwater light field:

$$\bar{\mu}\,(PAR) = \frac{E_d\,(PAR) - E_u\,(PAR)}{E_o\,(PAR)} \qquad \text{(Eq. 3.9)}$$

E_o (0^-,λ) was derived from Hydrolight (version 5), a radiative transfer model that computes radiance distribution and derives apparent quantities such as scalar irradiance for water bodies as a function of wavelength and depth.

Hydrolight input data are environmental conditions, above-water downward irradiance (E_d 0^+,λ), IOPs (a_{cdom}, a_p, b_p, and volume scattering function-VSF). The environmental conditions (such as sun angle), $E_d(0^+,\lambda)$ and $a_{cdom}(\lambda)$ were acquired at every site (n = 40). For the samples taken during the high water season, *in situ* IOP measurements (n=27) were available. For the low water campaign (n=13), given that IOPs were not measured, the specific IOPs (SIOPs) calculated based on the high water season measurements were used to calculate IOPs for the samples collected during low water season. This is a valid approach considering that SIOPs represent the specific inherent optical properties of the suspended particles in a given water body or region (Mobley, 2002). Specific particulate absorption, a^*_p [$m^{-2}.g^{-1}$], for example, is defined as follows:

$$a_p^*(\lambda) = \frac{a_p(\lambda)}{TSS} \qquad \text{(Eq. 3.10)}$$

where a_p [m^{-1}] and TSS [$mg.L^{-1}$] are the particulate absorption coefficient and total suspended solids, respectively.

Considering the variable nature and composition of the suspended matter in the different sampled rivers during high water season (n=27), SIOPs data were clustered in two groups according to composition and concentration of suspended solids: (i) waters with relatively low suspended solids concentration (up to 10 $mg.L^{-1}$) and percentage of

organic matter higher than 20%, such as Jamanxim and Tapajós/Santarém sites (n=21), which are characterized by clear waters; and (ii) water with high suspended solids concentration (TSS >20 $mg.L^{-1}$) and organic matter lower than 15%, such as the Crepori and Tocantins rivers (n = 6). The specific particle absorption and scattering coefficients for these two groups are illustrated in Figure 3.3. The suitable SIOP set was used along with TSS concentrations for each sample point measured during the high water period in September 2012 (n = 13) to further calculate IOPs as input for Hydrolight (Figure 3.3). The derived magnitude and spectral shapes are comparable to specific coefficients reported in literature (Campbell *et al.*, 2011; Mobley *et al.*, 2010).

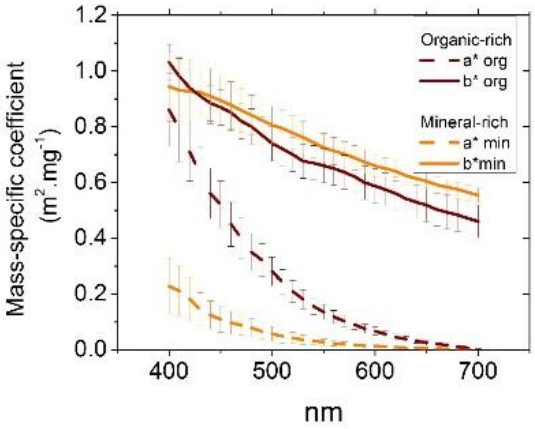

Figure 3.3: Specific IOPs based on a high water dataset plotted as a function of wavelength for inorganic matter (n = 6) and organic-rich waters (n=21). The inorganic set was used as input on the bio-optical model for samples taken at Crepori River, whereas the organic-rich set was used for the remaining samples taken along the Tapajós River (see Figure 3.2).

The volume scattering phase function (VSF) used in Hydrolight can either be chosen among several available functions, including the Petzold's VSF (Petzold, 1972), or it can be estimated using the measured backscattering ratio, *B* (Table 3.1) (Mobley *et al.*, 2002). In this study, as a proxy for VSF, we evaluated the Petzold's VSF function and *B* based on measured *b* and b_b. These two options were evaluated based on the

comparison between *in situ* $\rho_{surf}\ (red)$ and Hydrolight modeled $\rho_{msurf}\ (red)$. The red spectra were chosen because (i) are less influence by a_{cdom} compared with the blue and green spectra, and (ii) are generally more affected by sediment scattering (Sun *et al.*, 2012; Dekker *et al.*, 2002).

Modeled $\rho_{surf}\ (red)$ resulting from measured *B* showed an overestimation of approximately 30% when compared to measured $\rho_{surf}\ (red)$ (Figure 3.4). Since Petzold's VSF output showed lower RMSE, R^2, and slope closer to the 1:1, all the Hydrolight models used in this research were derived based on the Petzold's VSF model, which considers a default *B* of 0.018. This value has been used by several authors working in complex water conditions (Albert and Mobley, 2003; Mobley *et al.*, 2002; Stramski *et al.*, 2001).

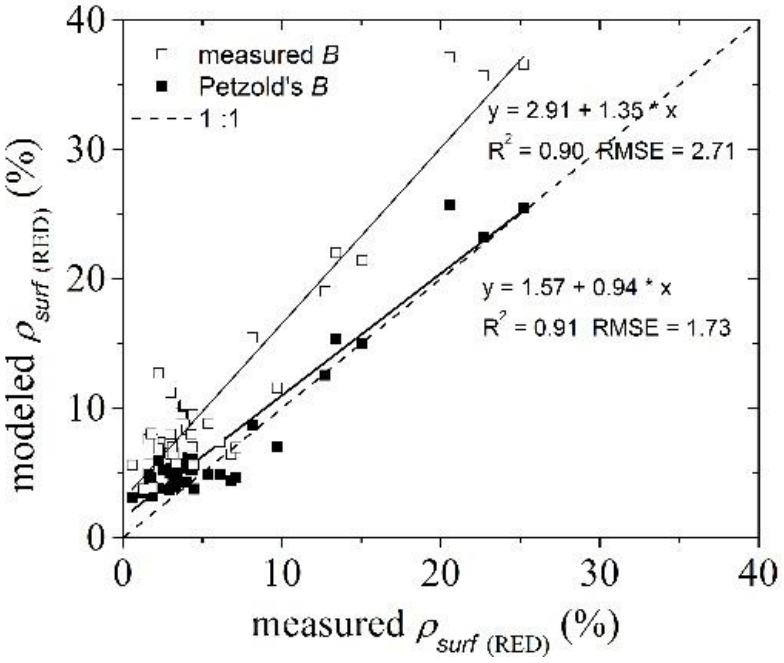

Figure 3.4: Validation of Hydrolight output performed by evaluating the relationship between measured and modeled $\rho_{surf}\ (red)$ (n = 40). Modeled values were performed

using measured *B* and Petzold's *B* as input. Lower RMSE and a slope closer to 1 are observed for Petzold's *B* when compared to measured *B*.

3.3.5 Critical depth for photosynthesis and *in situ* absorption coefficient

Once the $E_o(0^-,400\text{-}700nm)$ was modeled and validated, the critical depth and the absorption efficiency of phytoplankton were estimated for the different groups of water. Compensation depth or critical depth, (Z_c), is the depth at which the photosynthetic production by a phytoplankton community is equal to the energy loss on processes such as respiration. In other words, given optimum conditions of nutrient concentration, Z_c is the depth at which irradiance is the minimum necessary for photosynthesis. Z_c is calculated as follows (Kirk, 2011):

$$Z_c\ (PAR) = \frac{ln\, E_o\ (0-,PAR) - ln\, E_c\ (PAR)}{K_o\ (PAR)} \qquad \text{(Eq. 3.11)}$$

where E_o (0^-, PAR) is the sub-surface scalar irradiance modeled by Hydrolight; K_o (PAR) is the average scalar attenuation coefficient for PAR from surface to $Z_{1\%}$ (similar to Equation 3.7); and E_c (PAR) is the species-specific compensation irradiance. To calculate Z_c in this study, we adopted E_c (PAR) based on the freshwater phytoplankton minimum light requirement described by Deblois *et al.* (2013). The authors reported that *Chlamydomonas sp.* (Chlorophyta) (identified in this study) shows a growth rate close to zero when exposed to irradiance of 14 $\mu Em^{-2}s^{-1}$, whereas other species, such as *Aulacoseira granulate* (diatom) and *Cryptomonas obovata* (Cryptophyta), present a growth rate of up to 0.2 divisions/day when submitted to the same light regime. For freshwater phytoplankton communities, a minimum E_c of 14 $\mu Em^{-2}s^{-1}$ was defined as a

general compensation irradiance as described in Deblois *et al.*, (2013), and therefore used as input to calculate Z_c in Eq. 3.11.

Furthermore, analyses of critical depth have to take into account the depth of the mixing layer (Z_m). If the depth of the mixed layer is lower than or equal to Z_c, there is sufficient light to drive net production, and phytoplankton might grow (Sverdrup, 1953). On the other hand, if the Z_m is greater than Z_c, light can become a limiting factor for net production in deeper layers. In river systems, where high current velocity and turbulence mixes the water homogenously, the Z_m usually coincides with the total water depth (Z). In turbid and deep rivers such as the Amazon, phytoplankton is only exposed to light for a short period of time on the upper layers, which can reduce phytoplankton productivity, as indicated by Dustan (2009). For oceans and lakes, thermal stratification can occur, reducing the mixed layer to depths lower than Z_c and favouring phytoplankton growth and bloom (Siegel *et al.*, 2002).

The calculation of Z_c (Eq. 3.11) takes into account integrated PAR spectra (i.e., the Z_c is not specified per wavelength). However, the available underwater light field, from surface to the bottom, is generally not evenly distributed over the PAR range, especially in turbid waters of the Amazon (Costa *et al.*, 2013). Moreover, phytoplanktonic groups have different pigments assemblage, and as such, light available at different parts of the spectra can determine survival or domination of phytoplankton groups over others (Kishino, 1986). For example, an underwater light field rich in blue-green light will favour phytoplankton that has pigments that absorb light in the blue-green spectra (Markager and Vincent, 2001). The *in situ* specific absorption coefficient of phytoplankton, *in situ* $a^*_{ph}(\lambda)$, defines the wavelength efficiency of the phytoplankton

to absorb light within the PAR spectra, and therefore can be a better indicator of the relationship between spectral light availability and limitations for phytoplankton productivity (Deblois *et al.*, 2013)). *In situ* specific absorption coefficient is an apparent parameter that depends on how the specific absorption couples with *in situ* light spectrum (Markager and Vincent, 2001). *In situ* $a^*_{ph}(\lambda)$ is calculated as (Kishino, 1986; Markager and Vincent, 2001):

$$in\ situ\ a^*_{ph}(\lambda) = \bar{E}_o(z,\lambda) \cdot a^*_{ph}(\lambda) \qquad \text{(Eq. 3.12)}$$

where $\bar{E}_o(z,\lambda)$ represents modeled E_o (z,λ) normalized to measured E_d $(0^+, \lambda)$-, and $a^*_{ph}(\lambda)$ is the phytoplankton specific absorption coefficient. The specific absorption (a^*_{ph}) of two phytoplankton species reported by Bricaud *et al.* (1988) were used in this study: a cyanobacteria (*Synechocystis sp.*), which is a freshwater species identified in this study, and a diatom (*Chaetoceros sp.*), found in the oceans (Figure 3.5). Although not identified in this research, we used the a^*_{ph} for *Chaetoceros* as an example of diatom for two reasons. First, because of the lack of measured a^*_{ph} for freshwater that coincides with the species identified in this study; and second, because Bricaud *et al.* (1988) used similar methods for cross-section measurements of *Synechocystis sp.* and *Chaetoceros sp.*, thus avoiding disparate methodological issues. The a^* for these species show differences; specifically, cyanobacteria shows a prominent absorption peak at 625 nm due to phycocyanin, and diatoms shows slightly higher absorption in the blue wavelengths due to carotenoids such as fucoxanthin (Fujiki and Taguchi, 2002; Bricaud *et al.*, 1988).

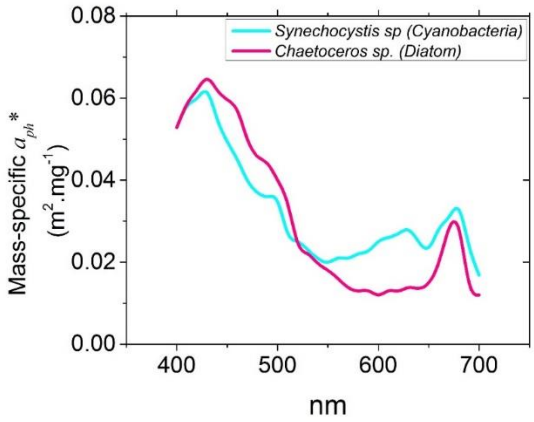

Figure 3.5: Spectral distribution of specific-absorption coefficient of phytoplankton based on Bricaud *et al.* (1988) for *Chaetoceros sp.* (diatom) and *Synechocystis sp*. (cyanobacteria).

The light field at two specific depths, sub-surface (z = 0.3 m) and at 2.0 m, were used to calculate *in situ* absorption efficiency of the two phytoplankton groups. The 2.0 m depth was used because preliminary analysis of data showed that light penetration was limited to this depth in inorganic-rich waters. Therefore, beyond this depth, comparison of phytoplankton absorption efficiency among water classes would not be possible.

Table 3.1: Compilation of all optical parameters used in this paper, including measured, calculated, and modeled optical properties and respective symbol, unit, and calculation formula.

Inherent Optical Property	**Symbol**	**Unit**	**Formula**
Attenuation coefficient	$c(\lambda)$	m^{-1}	Eq. (3.1)
Absorption coefficient	$a(\lambda)$	m^{-1}	Eq. (3.2)
Scattering coefficient	$b(\lambda)$	m^{-1}	Eq. (3.3)
Backscattering coefficient	$b_b(\lambda)$	m^{-1}	Eq. (3.4)
Specific absorption coefficient	$a^*_x(\lambda)$	$m^2.g^{-1}$	Eq. (3.10)
Specific scattering coefficient	$b^*_x(\lambda)$	$m^2.g^{-1}$	-
Backscattering ratio	$B(\lambda)$	-	$B = b_b/b$
Apparent Optical Property			
Upwelling radiance	L_u	$W.m^{-2}.sr^{-1}$	-
Downwelling irradiance	E_d	$W.m^{-2}$	-
Downwelling irradiance (above water)	$E_d\ (0+)$	$W.m^{-2}$	-
Upwelling irradiance	E_u	$W.m^{-2}$	Eq. (3.5)
Irradiance surface reflectance	ρ_{surf}	-	Eq. (3.6)
Scalar irradiance	E_o	$W.m^{-2}$	$E_o = E_u + E_d$
Downwelling irradiance attenuation coefficient	K_d	m^{-1}	Eq. (3.7)
Scalar irradiance attenuation coefficient	K_o	m^{-1}	Eq. (3.7)
Average cosine	$\bar{\mu}$	-	Eq. (3.9)
Normalized scalar irradiance	$\bar{E}_o$	-	Eq. (3.8)
Critical depth	$Z_c\ (PAR)$	m	Eq. (3.11)
in situ specific absorption coefficient	*in situ* $a^*_{ph}(\lambda)$	$m^2.mg^{-1}$	Eq. (3.12)

3.4 Results

3.4.1 Biogeochemical data

The biogeochemical data was stratified into five classes according to the intensity of water siltation, aiming to facilitate the interpretation of the results (Table 3.2). *Class 1* includes both, water bodies not subjected to mining activities and water bodies subjected to very low gold mining tailings, with concentrations of TSS up to 5.0 $mg.L^{-1}$. *Class 2* includes samples in which TSS concentrations vary from 5.0 to 10.0 $mg.L^{-1}$. Next, *Class 3*, *Class 4*, and *Class 5* represent waters with medium (10.0 to 20.0 $mg.L^{-1}$), high (20.0 to 50.0 $mg.L^{-1}$), and very high (50.0 to 150.0 $mg.L^{-1}$) concentrations of TSS caused by gold mining tailings, respectively. The spatial and temporal distribution of TSS concentration is schematically summarized in Figure 3.6. All the biogeochemical and optical data presented in Table 3.2 refers to mean values from triplicates. The standard deviation of each variable was omitted for an easier presentation of the results.

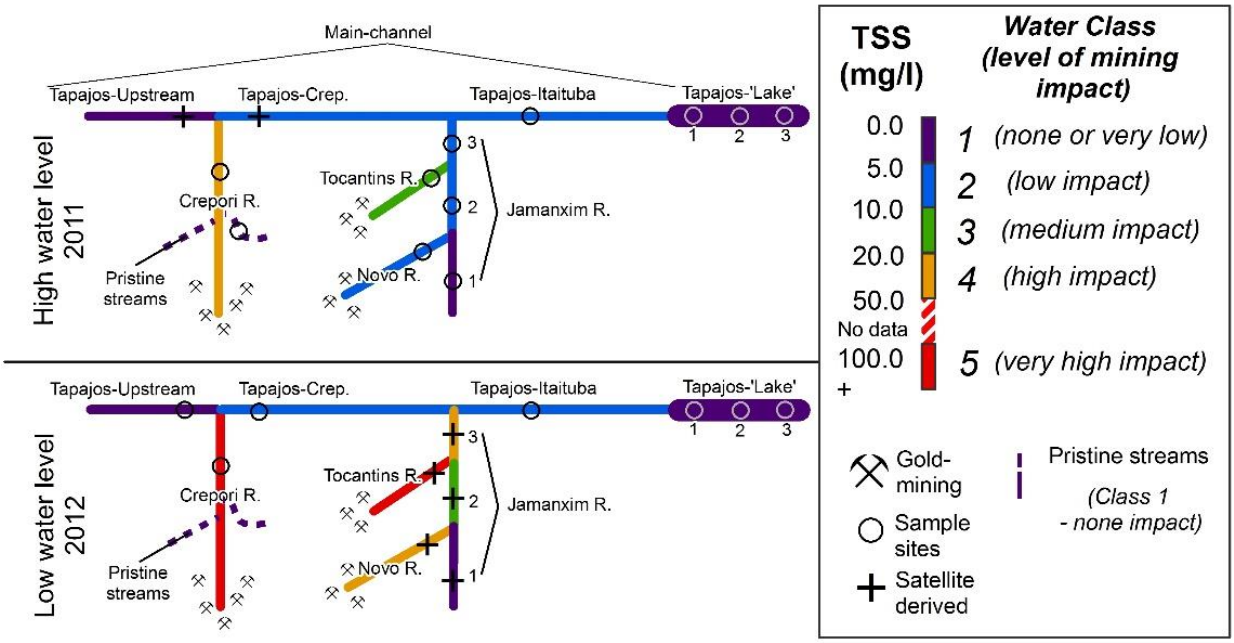

Figure 3.6: Schematic representation of TSS concentrations along the Tapajós River and its tributaries for high (April 2011) and low (September 2012) water levels. The river and its tributaries were classified according to TSS (mg.L^{-1}) concentrations. TSS for Tocantins, Novo, and Jamanxim rivers during the low water season were retrieved from Landsat $\rho_{surf}\,(red)$. Numbers represent location from upriver (1) to downriver (3) on the Jamanxim River and Tapajós 'Lake' section (figure not to scale). Satellite derived TSS concentration from Lobo *et al.* (2015). Level of mining impact was defined according to the author's expert knowledge and local knowledge considering the level of mining activities in the rivers.

Table 3.2: Values of suspended solids, *chl-a,* and optical properties for the water classes represented in Figure 3.6. *IOPs for low water samples were estimated based on linear regressions established for the measurements taken during the high water period (next pages). The standard deviation of each variable was omitted for an easier presentation of the results.

	local	season	depth Z (m)	Suspended Matter				Measured IOPs*			
				TSS	Org. Matter	POC	*chl-a*	a_{CDOM} (440)	a_p (440)	b_p (660)	b_{bp} (660)
				mg.L^{-1}	% of TSS	% of TSS	µg.L^{-1}	m^{-1}	m^{-1}	m^{-1}	m^{-1}
1	Pristine stream	high	3.1	2.9	24	10	0.02	2.8	0.4	1.3	0.05
	Jamanxim1	high	5.0	3.6	37	17	0.03	3.2	1.7	2.2	0.10
	Tapajós_Upstream	low	5.8	4.2	27	12	1.18	3.0	1.6	2.4	0.10
	Tapajós_Crep_left	low	5.4	3.6	30	14	0.96	2.5	1.6	2.1	0.09
	Tapajós-Lake1	high	6.3	3.7	31	16	0.82	3.2	1.8	2.7	0.10
	Tapajós-Lake2	high	8.3	3.4	40	15	1.08	2.9	1.6	2.4	0.10
	Tapajós-Lake3	high	9.8	3.5	37	11	0.56	2.7	1.7	2.8	0.09
	Tapajós-Lake3	low	15.3	1.8	58	28	1.20	2.5	1.5	1.3	0.06
	min		**3.1**	**1.8**	**24**	**10**	**0.02**	**2.5**	**0.4**	**1.3**	**0.05**
	max		**15.3**	**4.2**	**58**	**28**	**1.20**	**3.2**	**1.8**	**2.8**	**0.10**
	average (n=17)		**7.4**	**3.3**	**35**	**15**	**0.73**	**2.9**	**1.5**	**2.1**	**0.08**
	SD		**3.8**	**0.7**	**11**	**6**	**0.48**	**0.3**	**0.4**	**0.6**	**0.02**
2	Tapajós_Upstream	low	6.0	5.6	22	9	1.09	3.5	1.7	3.2	0.12
	Jamanxim2	high	5.5	6.1	28	10	0.05	3.1	1.7	3.3	0.13
	Jamanxim3	high	7.2	6.7	24	7	0.08	3.4	2.1	4.4	0.16
	Novo	high	5.0	6.8	28	9	0.08	3.3	1.7	3.7	0.16
	Tapajós_Itaituba	low	5.2	6.6	16	8	0.75	2.9	1.8	3.8	0.14
	Tapajós_Itaituba	high	4.9	6.2	28	10	0.67	3.2	2.1	4.0	0.12
	min		**4.9**	**5.6**	**16**	**7**	**0.05**	**2.9**	**1.7**	**3.2**	**0.12**
	max		**7.2**	**6.8**	**28**	**10**	**1.09**	**3.5**	**2.1**	**4.4**	**0.16**
	average (n=17)		**5.6**	**6.3**	**24**	**9**	**0.45**	**3.2**	**1.8**	**3.7**	**0.14**
	SD		**0.9**	**0.5**	**4**	**1**	**0.44**	**0.2**	**0.2**	**0.4**	**0.02**
3	Tapajós_Crep_right	low	5.0	13.4	11	4	1.10	3.1	2	7.7	0.26
	Tocantins	high	6.5	14.7	16	5	0.03	3.0	2.0	8.6	0.30
	average (n=2)		**5.8**	**14.0**	**13**	**4**	**0.57**	**3.1**	**2.0**	**8.2**	**0.28**
	SD										
4	Crepori	high	5.1	33.4	14	3	0.12	2.1	2.6	18.7	0.56
	Crepori	high	5.1	35.8	12	3	0.06	2.0	3.1	21.3	0.61
	Crepori	high	5.0	38.0	11	3	0.03	2.1	3.0	22.4	0.65
	average (n=3)		**5.1**	**35.7**	**12**	**3**	**0.07**	**2.1**	**2.9**	**20.8**	**0.6**
	SD		**0.1**	**2.3**	**1**	**-**	**0.04**	**0.1**	**0.3**	**1.9**	**0.0**
5	Crepori	low	2.1	109.4	3	2	0.65	2.2	6.1	63.2	1.88
	Crepori	low	2.1	111.1	2	2	0.64	2.8	6.1	64.3	1.91
	Crepori	low	2.0	113.6	2	2	0.73	2.4	6.2	65.5	1.95
	average (n=3)		**2.1**	**111.3**	**2**	**2**	**0.67**	**2.5**	**6.1**	**64.4**	**1.91**
	SD		**0.1**	**2.1**	**1**	**-**	**0.05**	**0.3**	**0.1**	**1.1**	**0.04**

	local	Measured AOPs					Modeled AOPs								
		$E_{d\ (+0)\ Blue}$	$E_{d\ (+0)\ Green}$	$E_{d\ (+0)\ Red}$	$K_{d\ (-0,\ PAR)}$	$R_{(+0,\ red)}$	$E_{o\ (0.3m,\ Blue)}$	$E_{o\ (0.3m,\ Green)}$	$E_{o\ (0.3m,\ Red)}$	$K_{d\ (-0,\ PAR)}$	$R_{(+0,\ red)}$	$E_{o1\%\ PAR}$	$K_{o\ (PAR)}$	$Z_{c\ (Chlamydomonas)}$	Z_m/Z_c
		$\mu E.^{-2}.s^{-1}$	$\mu E.^{-2}.s^{-1}$	$\mu E.^{-2}.s^{-1}$	m^{-1}	%	$\mu E.^{-2}.s^{-1}$	$\mu E.^{-2}.s^{-1}$	$\mu E.^{-2}.s^{-1}$	m^{-1}	%	$\mu E.^{-2}.s^{-1}$	m^{-1}	m	-
1	Pristine stream				-	-	308	653	712	1.5	3.2	-	0.71	7.0	0.4
	Jamanxim1	289	296	252	2.8	2.9	94	250	291	2.0	3.7	8.4	0.8	4.9	1.0
	Tapajós_Upstream	199	208	181	1.2	3.6	82	201	219	1.6	4.3	5.9	0.9	4.2	1.4
	Tapajós_Crep_left	298	318	278	1.1	2.1	112	268	292	1.6	4.5	9.4	0.8	5.1	1.1
	Tapajós-Lake1	432	467	412	2.7	3.2	109	339	414	2.1	4.7	17.0	0.9	5.1	1.2
	Tapajós-Lake2	289	295	251	2.5	2.2	86	237	281	1.9	3.9	8.9	0.9	4.7	1.8
	Tapajós-Lake3	280	293	253	2.7	1.7	82	262	333	2.2	4.8	6.8	1.0	3.8	2.5
	Tapajós-Lake3	585	647	578	1.0	1.3	242	570	632	1.5	3.3	19.0	0.7	6.7	2.3
	min	**199**	**208**	**181**	**1.0**	**1.3**	**82**	**201**	**219**	**1.5**	**3.2**	**5.9**	**0.7**	**3.8**	**0.4**
	max	**585**	**647**	**578**	**2.8**	**3.6**	**308**	**653**	**712**	**2.2**	**4.8**	**19.0**	**1.0**	**7.1**	**2.5**
	average (n=17)	**339**	**361**	**315**	**2.0**	**2.4**	**139**	**347**	**397**	**1.8**	**4.0**	**10.8**	**0.8**	**5.2**	**1.5**
	SD	**128**	**148**	**135**	**0.9**	**0.8**	**86**	**169**	**180**	**0.3**	**0.6**	**5.1**	**0.1**	**1.1**	**0.7**
2	Tapajós_Upstream	80	83	69	1.1	4.4	33	86	92	1.9	5.2	2.3	0.97	2.90	2.1
	Jamanxim2	275	289	252	3.2	4.2	87	287	349	2.2	5.2	8.0	1.00	3.80	1.4
	Jamanxim3	377	429	394	3.7	3.7	122	367	451	2.6	6.3	12.6	1.10	3.89	1.9
	Novo	288	294	250	3.6	3.8	85	268	332	2.5	5.4	8.3	1.02	4.01	1.2
	Tapajós_Itaituba	657	726	650	1.5	6.7	269	727	824	1.7	4.6	20.3	0.94	5.32	1.0
	Tapajós_Itaituba	595	659	590	3.1	3.0	186	606	779	2.6	5.4	13.8	1.11	3.96	1.2
	min	**80**	**83**	**69**	**1.1**	**3.0**	**33**	**86**	**92**	**1.7**	**4.6**	**2.3**	**0.94**	**2.90**	**1.0**
	max	**657**	**726**	**650**	**3.7**	**6.7**	**269**	**727**	**824**	**2.6**	**6.3**	**20.3**	**1.11**	**5.32**	**2.1**
	average (n=17)	**379**	**413**	**368**	**2.7**	**4.3**	**124**	**359**	**430**	**2.2**	**5.3**	**10.9**	**1.02**	**3.98**	**1.5**
	SD	**216**	**244**	**222**	**1.1**	**1.3**	**79**	**231**	**280**	**0.4**	**0.5**	**6.1**	**0.07**	**0.78**	**0.4**
3	Tapajós_Crep_right	559	613	546	3.2	9.7	201	631	749	2.3	7.0	17.2	1.23	3.91	1.3
	Tocantins	377	429	394	3.8	8.1	123	465	601	2.9	8.7	12.0	1.24	3.59	1.8
	average (n=2)	**468**	**521**	**470**	**3.5**	**8.9**	**162**	**548**	**675**	**2.6**	**7.9**	**14.6**	**1.24**	**3.75**	**1.5**
	SD														
4	Crepori	575	613	538	6.0	12.8	149	677	971	3.5	12.6	17.3	1.69	2.85	1.8
	Crepori	297	304	259	6.2	15.1	60	320	483	4.1	15.0	8.6	1.82	2.26	2.3
	Crepori	292	299	256	5.9	13.4	58	320	491	4.2	15.4	8.5	1.86	2.21	2.3
	average (n=3)	**388**	**406**	**351**	**6.0**	**13.7**	**89**	**439**	**648**	**4.0**	**14.3**	**11.4**	**1.79**	**2.44**	**2.1**
	SD	**162**	**180**	**162**	**0.2**	**1.2**	**52**	**206**	**280**	**0.4**	**1.5**	**5.0**	**0.09**	**0.36**	**0.3**
5	Crepori	634	668	628	9.0	19.8	33	490	1114	7.0	23.2	19.3	2.74	1.80	1.2
	Crepori	657	726	650	9.8	20.5	45	563	1123	7.4	25.7	20.3	3.13	1.59	1.3
	Crepori	640	704	628	9.8	22.7	35	502	1119	7.3	25.5	19.7	3.08	1.61	1.2
	average (n=3)	**643.7**	**699.3**	**635.4**	**9.6**	**21.0**	**37**	**519**	**1119**	**7.2**	**24.8**	**19.8**	**2.98**	**1.66**	**1.2**
	SD	**12.1**	**28.9**	**12.4**	**0.5**	**1.5**	**7**	**39**	**4**	**0.2**	**1.3**	**0.5**	**0.21**	**0.12**	**0.1**

Class 1 includes pristine streams (not mined), which were used as reference for comparison with mined rivers throughout the paper, upstream Jamanxim (Jamanxim 1), Tapajós_Upstream, and the Tapajós Lake section of the river (Figure 3.6), corresponding to a total of 17 samples. Although all samples belong to clear water, their hydrodynamic characteristics vary from lotic upriver to a semi-lentic system at the Tapajós Lake region. For that reason, they will be presented and discussed separately.

The pristine headwaters, sampled during high water, exhibited low concentrations of TSS (2.9 $mg.L^{-1}$), $a_{cdom(440)}$ (2.8 m^{-1}), and *chl-a* concentrations not higher than 0.1 $\mu g.L^{-1}$. Sampled in the same period, the Jamanxim 1 site showed slightly higher biogeochemical concentrations than the pristine streams, with $a_{cdom}(440)$ of 3.2 m^{-1} and maximum values of TSS of 3.6 $mg.L^{-1}$ with 37 % of organic content (POC = 17%), whereas pristine streams organic matter were approximately 24% (POC = 10%). Tapajós_Upstream, sampled during the low water period, showed similar suspended sediment and organic content concentrations as those of Jamanxim 1, but with a higher average *chl-a* concentration (1.1 $\mu g.L^{-1}$).

At the lower section of the Tapajós Lake, TSS values of 2.0 $mg.L^{-1}$ were measured during the low water level, and approximately 3.0 $mg.L^{-1}$ in the high water period. The organic content in the Tapajós Lake was consistently higher than that in upstream tributaries and Tapajós_Upstream in both seasons, with an average of 50% (POC ~ 13%). Differences were not observed for $a_{cdom(440)}$. c*hl-a* followed the values observed at the upstream Tapajós River, with concentrations up to 1.4 $\mu g.L^{-1}$.

Class 2 includes 15 sites with TSS between 5.0 and 10.0 $mg.L^{-1}$, and comprises water samples taken at the Jamanxim River, after discharge from the Novo (Jamanxim 2)

and Tocantins rivers (Jamanxim 3), acquired during the high water period, and waters of the Tapajós River at Itaituba (Tapajós_Itaituba), sampled during both periods (see Figure 3.6). TSS was relatively higher (6.3 $mg.L^{-1}$ in average) than in *Class 1* (3.3 $mg.L^{-1}$), which decreased the relative organic and POC content to 24% and 9%, respectively. On the other hand, $a_{cdom(440)}$ (3.2 m^{-1}) values were statistically similar ($p>0.05$) for both classes. The average *chl-a* concentration within *Class 2*, however, was higher (1.1 $\mu g.L^{-1}$) at the Tapajós_Itaituba river section than at the tributaries (0.1 $\mu g.L^{-1}$ in average).

Class 3, which includes tributaries subjected to gold mining impact, is represented by only two samples, one collected during the high water period at the Tocantins River and another collected during low water level at the Tapajós River, after receiving the Crepori River inflow (named Tapajós_Crepori). Although this class characterized a distinct water mass with TSS between 10.0 and 20.0 $mg.L^{-1}$, the low number of samples (n=2) prevented statistical tests among other classes. Overall, $a_{cdom(440)}$ were similar to those from previous classes, and organic matter decreased to 13% (POC = 4%), indicating an increased influence of inorganic sediment input from mining tailings to the TSS when compared to *Classes 1* and *2*.

Class 4 and *Class 5* comprise samples of the Crepori River at the high (n=3) and low water (n=3) periods, respectively. During the high water level period, TSS concentrations of approximately 33.0 $mg.L^{-1}$ were measured in three locations; during the low water period, TSS increased to 111.0 $mg.L^{-1}$. On the other hand, $a_{cdom(440)}$ decreased to 2.1 and 2.5 m^{-1}, respectively. The organic matter content for *Class 4* was not different from those observed in *Class 3*, but it decreased to 2% for *Class 5* mostly POC (Table 3.2). In terms of *chl-a*, the Crepori River presented relatively higher *chl-a* (0.7 $\mu g.L^{-1}$)

concentration during low water level when compared to samples acquired during high water level (0.1 µg.L^{-1}).

3.4.2 Phytoplankton and pigments

The phytoplankton microscopy analysis indicated some general tendencies. First, a higher biovolume ($mm^3.L^{-1}$) was measured during the low water period compared to the high water period. However, due to sampling restrictions, a direct seasonal comparison was only possible for the Crepori and Tapajós_Itaituba sites, which both indicated lower productivity during the high water compared to the lower water period (Figure 3.7a). Second, changes were observed in the phytoplankton community from upstream tributaries, where the phytoplankton biovolume was lower and composed mostly of diatoms and cryptomonads when compared to the Tapajós Lake section where most of the phytoplankton biovolume is higher and represented by cyanobacteria cells.

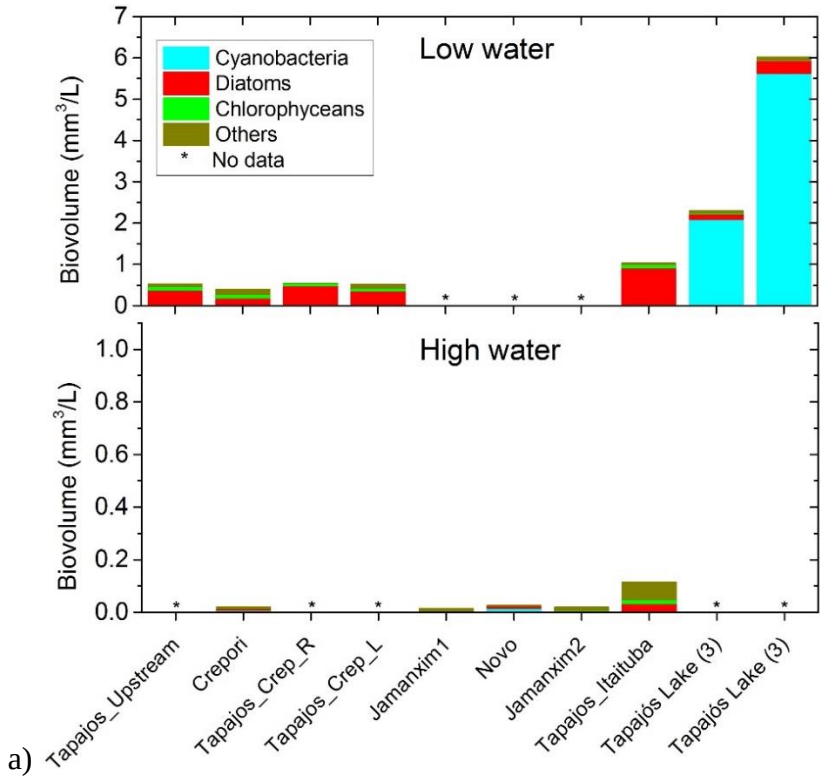

a)

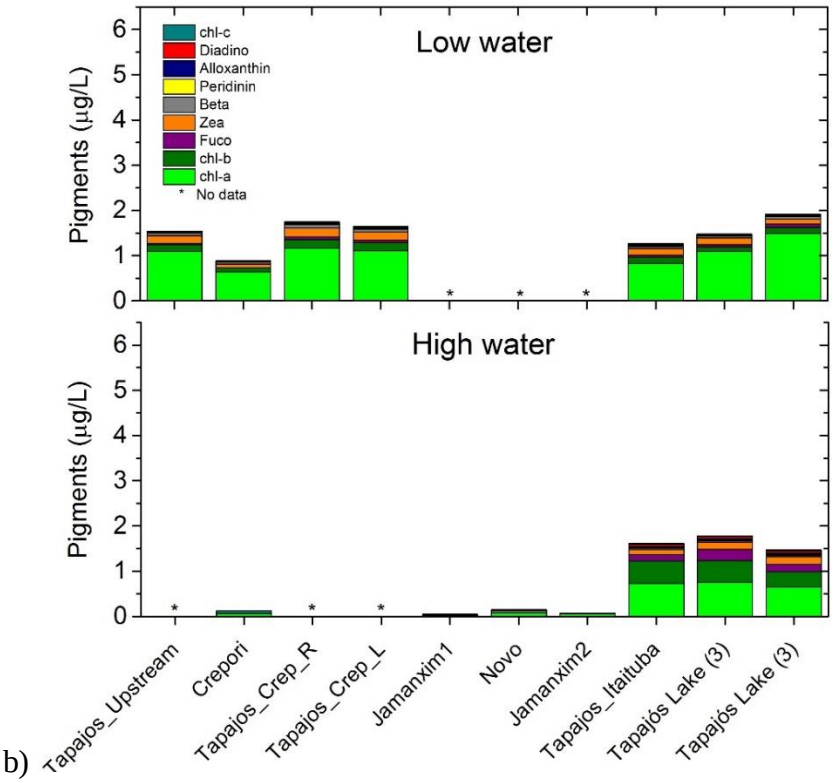

b)

Figure 3.7: Spatial distribution of (a) phytoplankton groups (mm^3/ml), and (b) pigments concentration ($\mu g.L^{-1}$) along the Tapajós River for high and low water level periods.

During the low water period, the Crepori River and the Tapajós_Upstream sites had biovolume of approximately 0.7 $mm^3.L^{-1}$ and were dominated by diatoms (*Aulacoseira granulata,* for example) and cryptophyceae (*Cryptomonas sp*). A similar phytoplankton community was identified at Tapajós_Itaituba site, with an average biovolume of 1.1 $mm^3.L^{-1}$. At the Tapajós Lake 3 section, however, biovolume reached 6.0 $mm^3.L^{-1}$, with prevalence of cyanobacteria species, such as *Synechocystis aquatilis* and *Aphanocapsa sp*. During the high water period, the Tapajós_Itaituba site showed a maximum biovolume of 0.1 $mm^3.L^{-1}$, which was mostly composed of diatoms and cryptomonads. The upstream tributaries (Crepori, Jamanxim, and Novo rivers), however, presented smaller biovolumes (< 0.1 $mm^3.L^{-1}$) composed of an assemblage of different taxonomic groups including chrysophyceae, diatom, cryptomonads, and cyanobacteria.

Similarly to the biovolume seasonal differences observed in the Crepori and Tapajós_Itaituba sites, direct comparison of pigments composition indicated lower productivity during the high water period (Figure 3.7b). In terms of spatial distribution, the total pigments concentration presented relatively higher magnitudes (up to 1.9 $\mu g.L^{-1}$) in the main Tapajós channel compared to the tributaries (< 0.1 $\mu g.L^{-1}$). The relative contribution of auxiliary pigments in relation to *chl*-a ([*pigm.*]/[*chl-a*]) at Tapajós_Itaituba and Tapajós Lake was *chl-b* (42%), *zeaxanthin* (18%), and *fucoxanthin* (11%). This pigment assemblage indicates that the majority of the phytoplankton groups were composed of cyanobacteria (zeaxanthin marker) and diatoms (fucoxanthin) (Mackey, 1996).

During the low water level, total pigment contents varied between 1.0 and 2.0 $\mu g.L^{-1}$ for all samples, with no clear difference in pigment contents in Tapajós Lake when

compared with those at the main channel and tributaries (Crepori). The total pigment concentration in the Crepori River was higher during the low water level than at the high water period, similar to the biovolume data. Overall, the relative contribution of auxiliary pigments was consistent throughout the samples, showing *chl-b* (14%), *zeaxanthin* (14%), and *fucoxanthin* (4%) among the main contributors. The pigments composition indicated the dominance of similar phytoplankton groups in both hydrographic phases, for example, fucoxanthin, indicating diatoms and chrysophyta, and zeaxanthin, indicating cyanobacteria. At both water level periods, *chl-b*/*chl-a* presented relative high concentrations (up to 43%), thus indicating the presence of green algae (chlorophyta), which was confirmed with the microscopy analysis.

3.4.3 Nutrients

The variability of the nutrient concentrations, specifically phosphate and nitrate, along the Tapajós River with Crepori confluence (Tapajós_Crepori), for the low water season, is shown in Figure 3.8. These values represent single measurements at each sample site. The upstream section of the Tapajós River was characterized as a typical oligotrophic system (Junk, 1997; Sioli, 1984) with low nutrient concentrations (phosphate ~ 6.2 $\mu g.L^{-1}$; and nitrate ~1.8 $\mu g.L^{-1}$) (. The Crepori River, however, showed characteristics of a eutrophic system (Junk, 1997; Sioli, 1984), with high concentrations of phosphate (33.0 $\mu g.L^{-1}$) and nitrate (132.0 $\mu g.L^{-1}$). Just below the Crepori River confluence (Tapajós_Crepori), phosphate and nitrate concentrations in Tapajós River increase to 7.7 and 13.2 $\mu g.L^{-1}$, respectively, due to the nutrient-rich Crepori discharge.

Downstream, at the Tapajós Lake 3, phosphate and nitrate concentrations remained slightly higher at 6.9 and 6.8 µg.L^{-1}, respectively.

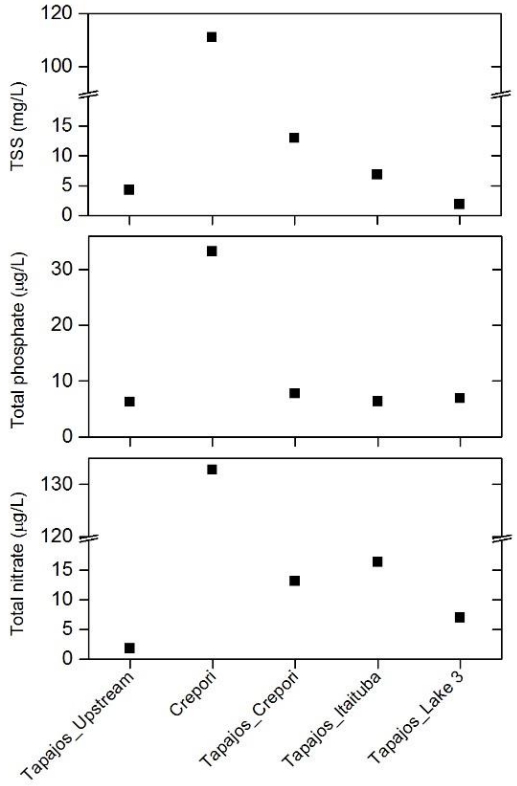

Figure 3.8: Concentration of the main nutrients along the Tapajós River including the Crepori River close to the Tapajós River. The locations of the sites are indicated in the Figure 3.2 and Table 3.2. Data available only for the low water level.

3.4.4 Bio-optical data

Measured IOPs

The absorption spectra by coloured dissolved organic matter (CDOM) has a typical power-law function, decreasing from blue towards red wavelengths (Figure 3.9a), and similar ($p>0.05$) $a_{cdom(440)}$ magnitudes (~2.7 m^{-1}) among the different classes of water, except for *Class 4*, which showed slightly lower $a_{cdom(440)}$ (2.0 m^{-1}) (Table 3.2).

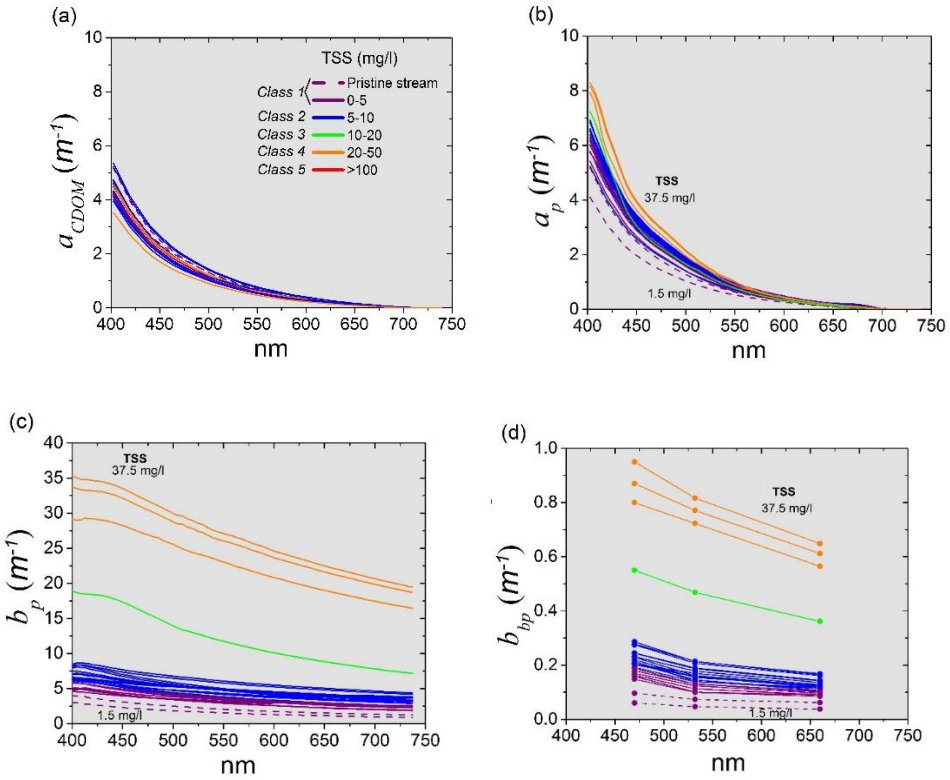

Figure 3.9: Spectral distribution of *in situ* IOPs for different water classes: absorption by particles (a) and CDOM (b); and particulate scattering (c) and backscattering (d). Coloured curves represent the five classes of water as explained in section above. Note that *Class 5* (red curve) is not shown in b, c, and d due to lack of data.

Overall, a_p, b_p, and b_{bp} showed a larger variability, similar to the TSS trend; that is, as the TSS increased, the IOPs increased linearly with correlation coefficients as high as 0.99 for both b_p and b_{bp} ($p<0.05$) (Table 3.3). Particulate absorption, $a_{p(440)}$, ranged from 1.4 m^{-1} for *Class 1* to 1.9, 2.0, and 2.9 m^{-1} for *Class 2*, *3*, and *4*, respectively (Figure 3.9b). In terms of scattering properties, $b_{p\ (660)}$ was lower than 1.5 m^{-1} in pristine streams, and increased to values of 2.7, 3.8, 8.6, and 20.8 m^{-1} for *Class 1*, *2*, *3*, and *4*, respectively (Figure 3.9c). Further, the contribution of $b_{p(660)}$ to total attenuation, $c_{(660)}$ vary from 34% for *Class 1*, 43% for *Class 2*, 60% for *Class 3*, to > 80% for *Classes 4* and *5*. The backscattering coefficient, $b_{bp(660)}$, also exhibited a similar trend. In pristine streams, b_{bp}

$_{(660)}$ was 0.05 m^{-1}, and an average of 0.10 m^{-1}, 0.13 m^{-1}, 0.30 m^{-1}, and 0.60 m^{-1} for *Classes 1*, *2*, *3*, and *4*, respectively. The $B_{(660)}$ values varied from 0.029 to 0.046, with an overall average of 0.036 (n = 40) and no significant difference ($p<0.05$) among the classes (Table 3.3).

Measured AOPs

Above-water reflectance showed very contrasting wavelength trends, both in magnitude and shape (Figure 3.10). As TSS increased, the observed maximum peak of ρ_{surf} shifted from green wavelengths for *Classes 1* and *2*, to red wavelengths for *Classes 4* and *5*. $\rho_{surf}\ (red)$ varied from 2.6% for *Class 1* up to 4.2, 8.9, 13.7, and 21.0%, for *Classes 2*, *3*, *4*, and *5*, respectively, thus showing a strong linear correlation with TSS ($r = 0.93$, $p<0.05$, n = 38). The correlation with TSS decreased from strong and significant at green ($r = 0.88$, $p<0.05$, n = 38) towards weak and not significant at the blue band ($r = 0.10$, $p>0.05$, n = 38) wavelengths. For the other optical active components, $a_{cdom}(440)$ and *chl-a*, no significant correlations were observed with ρ_{surf} at the blue, green, or red spectra (Table 3.4).

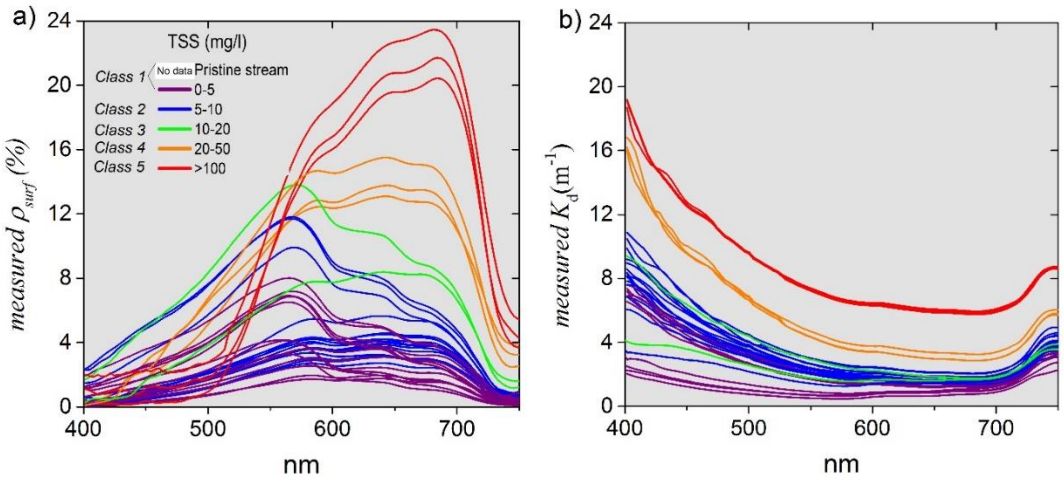

Figure 3.10: a) Measured surface reflectance, ρ_{surf} (λ) and b) diffuse attenuation coefficient K_d (λ), for both field campaigns for the different classes (n = 38).

The spectra for diffuse attenuation of downwelling irradiance (K_d) exhibited high values at blue wavelengths, decreasing towards red wavelengths (Figure 3.10-b), similar to the IOPs spectra. Considering the PAR range, *Class 1* presented a $K_{d(\mathrm{PAR})}$ of 1.9 m^{-1}, *Class 2* showed an average $K_{d(\mathrm{PAR})}$ of 2.8 m^{-1}, and *Classes 3*, *4*, and *5* values were as high as 3.5, 6.0, and 9.6 m^{-1}, respectively. Not surprisingly, $K_{d(PAR)}$ showed a strong linear correlation with TSS at all wavelengths, red (r = 0.96), green (r = 0.94), and blue (r = 0.84, $p<0.05$, n = 38). Again, similar correlations were not observed for *chl-a* and $a_{cdom(440)}$ data (Table 3.4).

Table 3.3: Correlation coefficients between IOPs and suspended solids, *chl-a* and AOPs. Data from high water only (n = 27, except measured AOPs with no pristine data, resulting in n = 25). Correlation coefficients highlighted in red are significant (p<0.05).

	Suspended Solids		*Pigm.*	*Meas. AOP*	*Mod. AOPs*		
IOPs	*TSS*	*POC*	*chl-a*	$K_{d(PAR)}$	$K_{d(PAR)}$	$\bar{E}_{o\,(PAR)\,(0.3m)}$	$\bar{E}_{o\,(PAR)\,(2.0m)}$
$a_{p\,(440)}$	0.71	0.80	0.02	0.88	0.89	0.63	-0.86
$b_{p\,(660)}$	0.99	0.94	-0.27	0.94	0.90	0.91	-0.75
$b_{bp\,(660)}$	0.99	0.94	-0.32	0.95	0.90	0.92	-0.75
$B_{\,(660)}$	-0.41	-0.39	-0.31	-0.32	-0.42	-0.30	0.41

Table 3.4: Correlation coefficients between suspended sediment, *chl-a*, and a_{cdom}, with measured and modeled AOPs. Data from high and low water (n = 40, except measured AOPs with no pristine data, resulting in n = 38). Correlation coefficients highlighted in red are significant (p<0.05).

	Measured AOPS				*Modeled AOPs*		
	$K_{d(blue)}$	$K_{d(green)}$	$K_{d(red)}$	$K_{d(PAR)}$	$K_{d(PAR)}$	$\bar{E}_{o\,(PAR)\,(0.3m)}$	$\bar{E}_{o\,(PAR)\,(2.0m)}$
TSS	0.84	0.94	0.96	0.91	0.91	0.57	-0.71
POC	0.89	0.95	0.97	0.93	0.96	0.23	-0.84
a_{CDOM}	-0.48	-0.34	-0.25	-0.37	0.18	-0.39	-0.23
chl-a	-0.20	-0.20	-0.21	-0.19	-0.10	-0.24	0.22

Modeled scalar irradiance and the underwater light field

The magnitude of the modeled $E_{o\,(0.3m,\,\lambda)}$ values in $\mu E.m^{-2}$ are shown in Table 3.2 for averaged blue, green, and red bands. Table 3.2 also includes the *in situ* measured downwelling irradiance $E_{d(+0,\,\lambda)}$ used to normalize $E_{o(0.3m,\,\lambda)}$, which resulted in $\bar{E}_{o\,(0.3m,\,\lambda)}$ (Figure 3.11a). Overall, $\bar{E}_{o\,(0.3m,\,\lambda)}$ showed an average magnitude of 1.0 and a spectral

shape indicating and increasing from blue to red wavelengths. Values higher than 1.0 can occur when the upwelling irradiance, $E_{u\,(0.3m,\,\lambda)}$, contributes significantly to total scalar irradiance $E_{o(0.3m,\,\lambda)}$ (Kuhl, 1994). At sub-surface, pristine streams presented half of the incoming light at blue wavelengths and approximately 100% at the green and red wavelengths. In more highly turbid waters (*Classes 4* and *5*), short wavelengths decreased quickly at sub-surface, and on the contrary, green and mainly red wavelengths showed $E_{o\,(0.3m)}$ values up to 175% of incoming light, thus comprising most of the $\bar{E}_{o(0.3m,\,PAR)}$ at this depth (Table 3.2). At 2.0 m depth, most of the light availability for all classes is within the green and red wavelengths; blue light is fully attenuated, even in pristine streams (Figure 3.11-b). At this depth, *Class 5* presented only 0.1% of the incoming PAR light, increasing towards *Class 4* (0.4%), *Class 3* (10.1%), *Class 2* (13.5%), and *Class 1* (18.0%).

The average cosine ($\bar{\mu}$), which indicates the diffusivity of the underwater light field (Kirk, 2011), also revealed a clear trend: pristine streams showed an average cosine ($\bar{\mu}$) from surface to bottom of approximately 0.80; and, as water became more turbid, the average cosine decreased due to the increase on light diffusivity. *Class 1* showed an average cosine of 0.74; *Class 2*, 0.66; *Class 3*, 0.53; *Class 4*, 0.42; and lastly, *Class 5* presented an average cosine of 0.34 (Figure 3.11-d). This is in agreement with the $Z_{1\%}$ values, which showed that high $\bar{\mu}$ are associated with high $Z_{1\%}$. Overall, the depth in which $\bar{E}_{o\,(PAR)}$ is 1% ($Z_{1\%}$) varied from 6.4 m in pristine streams, to an average of 5.4, 4.3, 3.6, 2.8, and 1.9 m for *Classes 1* to *5*, respectively. The wavelength in which light penetrates the most at $Z_{1\%}$, shifted from 620 nm in *Classes 1* and *2*, to 660 nm in turbid waters, such as *Classes 4* and *5* (Figure 3.11c).

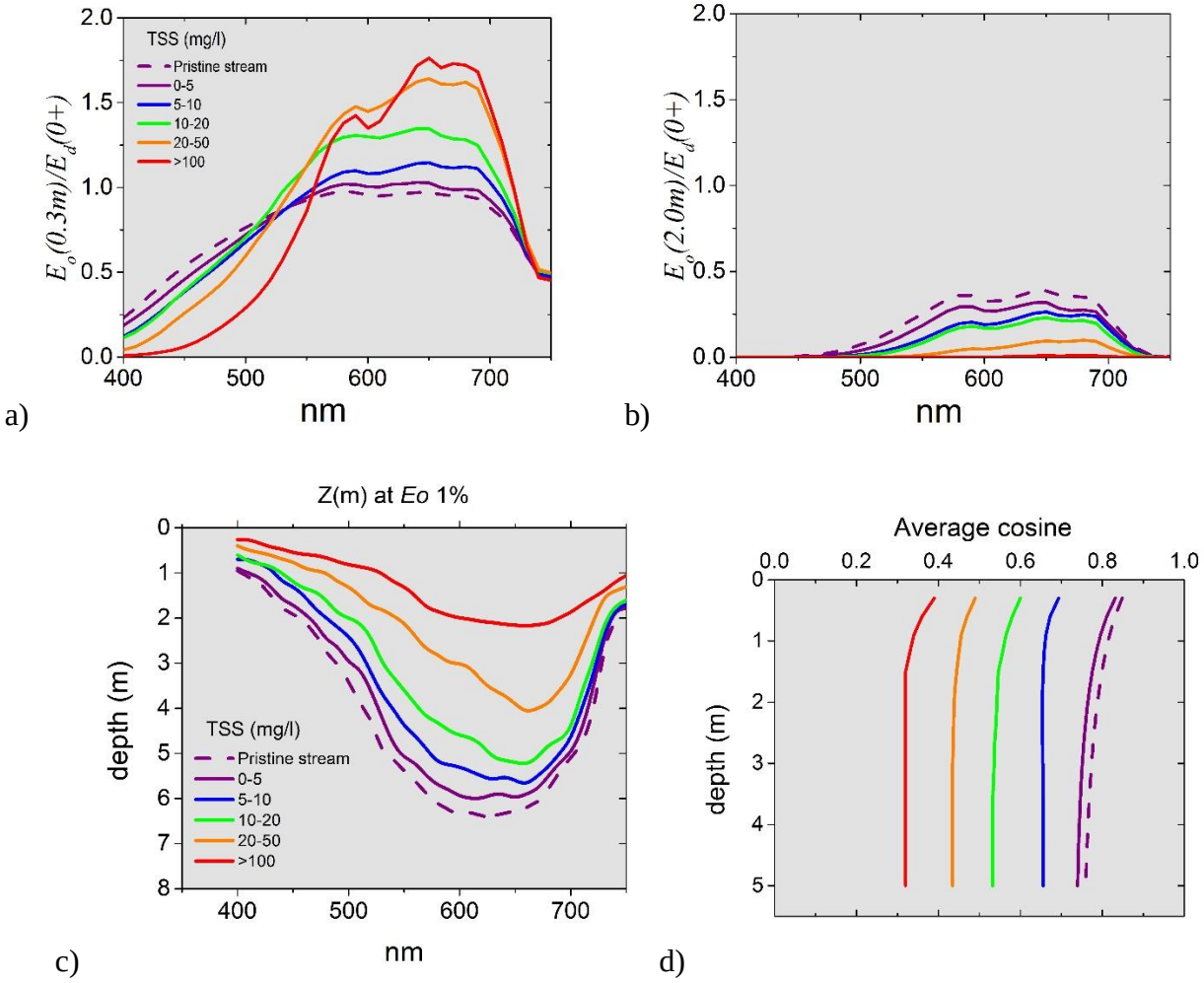

Figure 3.11: Normalized scalar irradiance at 0.3 m (a) and at 2.0 m deep (b) for all samples grouped by TSS. c) Spectral profile of $Z_{1\%}$ averaged for each class, and (d) vertical profile of $\bar{\mu}$ averaged for each class.

3.4.5 Critical depth and in situ specific absorption for phytoplankton

The light compensation depth or critical depth, Z_c, for *Chlamydomonas sp* indicated that enough light was available for photosynthesis up to 7.0 m depth in pristine streams. The critical depth decreased to ~5.2 m for the remaining samples within *Class 1*. As

expected, Z_c decreased with increasing K_o, thus resulting in a critical depth of 4.0, 3.7, 2.4, and 1.6 m for *Class 2, Class 3, Class 4*, and, *Class 5*, respectively (Table 3.2).

The estimated *in situ* specific absorption (*in situ* a^*_{ph}) for the two chosen examples of phytoplankton groups, diatom and cyanobacteria, showed slightly higher absorption in the blue region of the spectra for diatoms; however, cyanobacteria are generally more efficient at absorbing PAR than diatoms due to absorption peak at 622 nm (Figure 3.12). For example, at the sub-surface of pristine rivers, the *in situ* a^*_{ph} for diatoms was 0.62 $m^{-2}.mg^{-1}$, whereas for cyanobacteria it was 0.70 $m^{-2}.mg^{-1}$. For *Class 4*, at sub-surface, the *in situ* $a^*_{ph\ (PAR,\ diatom)}$ (0.61 $m^{-2}.mg^{-1}$) was similar to that of pristine streams (0.62 $m^{-2}.mg^{-1}$) due to very high absorption at 675 nm. However, for *Class 5*, the reduction of *in situ* a^*_{ph} at the blue spectra was no longer compensated by the very high absorption in the red spectra (*in situ* $a^*_{ph\ (PAR,\ diatom)}$ = 0.48 $m^{-2}.mg^{-1}$). At 2.0 m depth, the *in situ* $a^*_{ph\ (PAR,\ diatom)}$, for example, decreased from 0.11 $m^{-2}.mg^{-1}$ in pristine rivers to values close to 0.01 $m^{-2}.mg^{-1}$ in turbid waters due to the low light availability.

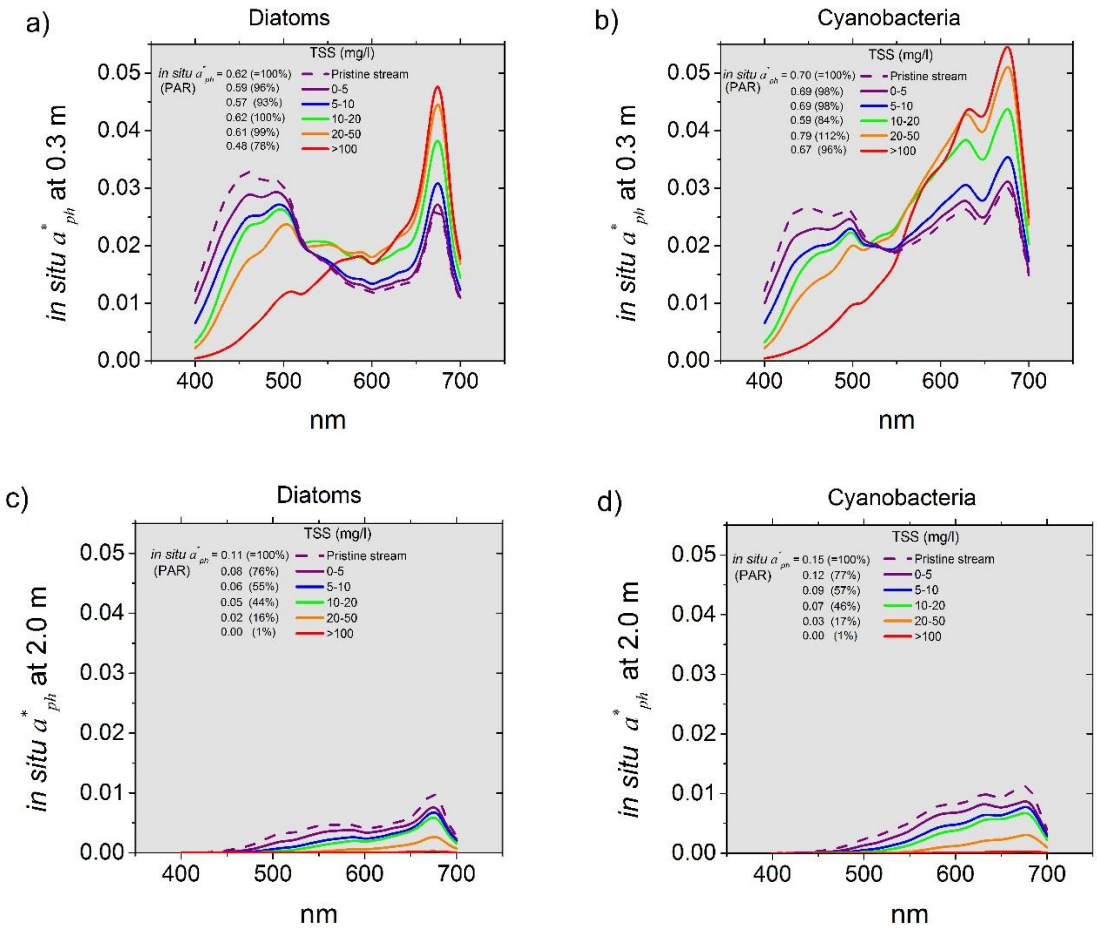

Figure 3.12: Spectral distribution of *in situ* $a^*_{ph\ (\lambda)}$ by diatom and cyanobacteria given the normalized E_o at sub-surface (0.3 m) and at 2.0 m deep. The integral of *in situ* $a^*_{ph\ (PAR)}$ for all curves are shown in the corresponding graph with relative percentage (%) based on pristine streams (taken as 100%).

3.5 Discussion

The biogeochemical and the optical properties of the Tapajós River and its tributaries were presented, followed by an evaluation of the consequences of increased TSS concentrations derived from small-scale mining tailings on the underwater scalar irradiance. From this dataset, water masses subject to different mining impacts were categorized into TSS representative classes, and the associated underwater light characteristics were described. Measured and modeled optical properties indicated that the incoming light (PAR) is rapidly attenuated with increasing TSS concentration. Consequently, non-impacted tributaries (TSS < 6.0 $mg.L^{-1}$) presented a critical depth (Z_c) for phytoplankton productivity of 6.0 m, while for high turbidity waters (TSS > 100.0 $mg.L^{-1}$) light was highly attenuated, and the critical depth was reduced to 1.6 m. The optical data also indicated that light attenuation was wavelength dependent and higher at blue wavelengths. The remaining underwater available light for both impacted and non-impacted waters was mostly at green and red wavelengths. In both water classes, analysis of *in situ* specific absorption coefficient (a^*_{ph}) for two major phytoplankton groups (cyanobacteria and diatoms) suggested that the absorption system of cyanobacteria would be more efficient than that of diatoms given an underwater environment dominated by red wavelengths. Since no difference of phytoplankton biovolume and pigments among impacted and non-impacted rivers was observed (Figure 3.7), the results indicated that other physical/chemical factors, such as the interaction between critical and mixed layer depth, current velocity, and nutrient concentrations could also play an important role in controlling phytoplankton productivity and diversity in the rivers subjected to mine tailings impact.

3.5.1 Mining-derived TSS as the main factor changing the water optical properties and light field

The TSS concentrations in the mined rivers varies spatially and seasonally as a result of the annual dynamics of the flood pulse (Melack and Forsberg, 2001; Junk, 1997), the biogeochemistry and geology of the watershed (Junk, 1997; Sioli, 1984), and the gold mining activities (Telmer and Stapper, 2007; Lobo *et al.*, 2015). According to the common classification of rivers in the Amazon basin, the sampled upstream Tapajós River is classified as "clear water" (Sioli, 1984; Junk, 1997; Telmer *et al.*, 2006) with low TSS (~ 5.0 $mg.L^{-1}$), low dissolved organic matter (a_{cdom} < 2.5 m^{-1}), and low *chl-a* (< 1.0 $\mu g.L^{-1}$). In spite of a few mining operations in the upstream area (see Figure 3.2), the measured sediment concentration is very low, thus resulting in a relatively deep euphotic zone (~ 5.5 m). In these waters, the suspended sediment has a considerable amount of organic matter (~ 30 % of TSS), composed mostly of allochthonous plant debris (Roulet *et al.*, 1998; Bernardes *et al.*, 2004). The characteristics and concentration of the suspended sediments change abruptly as the Tapajós River receives clay-rich tributaries, such as the heavily-mined Crepori River (TSS~111.3 $mg.L^{-1}$ and organic matter < 3%, euphotic depth ~ 2.0 m). Similarly, TSS at the Jamanxim River increases (*Class 1* and *Class 2*) as it receives sediment-rich discharge from the Novo and the Tocantins sub-basins (Figure 3.6) subject to mining operations. The sediment plume from the Crepori River only fully mixes with the Tapajós River waters after receiving the Jamanxim River discharge and passing through rapids about 200 km downstream (Telmer *et al.*, 2006; Lobo *et al.*, 2015). After the rapids, as the sediment load dilutes and the water velocity decreases, the TSS concentration decreases to values similar to those of the upstream Tapajós River.

Seasonally, the increase of TSS from ebbing to rising water periods is in part a result of the suspended solids input carried during rain events as the water rises (Melack and Forsberg, 2001; Junk, 1997). Gold mining activities are also temporally dynamic, that is, during the rainy season most of the gold mining activity discontinues (Bezerra *et al.*, 1998), and dilution due to an increase in volume of water in the rivers causes the sediment concentration to decrease. When the rainy season ends, mining activities intensify, and together with the lower water volume in the dry season, increased concentrations of sediment to levels above 100 $mg.L^{-1}$ are typical (Figure 3.6).

Sediment flushed into the rivers from small-scale mining operations is composed of an agglomeration of fine clay particles (Telmer *et al.*, 2006; Veiga, 1997), mostly kaolinite (CPRM, 2009). These mine-derived clay particles cause general changes in magnitude and spectral dependency of IOPs and AOPs compared with water under less or no influence of mined rivers (Figures 3.9 and 3.10). This is mostly because fine inorganic clay particles tend to be more effective at scattering light due to their lower specific absorption coefficient and higher refractive indexes compared to large inorganic particulates (silt, medium sand), organic particulates such as *flocs* (agglomeration of particles), and phytoplankton (Bowers and Binding, 2006; Binding *et al.*, 2005). The absorption curves for particulate matter showed a typical power-law function (Mobley, 1994), and the characteristic *chl-a* absorption peak at 675 nm was not clearly observed in the samples taken, thus indicating that suspended matter, mostly of inorganic nature, and dissolved organic matter are the main optical components absorbing light in the non-impacted (*Class 1*) and impacted tributaries (*Classes 3-5*), respectively. Similarly, Carvalho *et al.* (2015) have shown that in the waters of Curuai Lake, adjacent to the

lower Tapajós River, where inorganic content was dominant on *chl-a*, absorption curves follow a power-law function. However, as mineral content decreased or *chl-a* increased up to 91.0 µg.L^{-1}, the prominent *chl-a* absorption peak at 675 nm was observed.

Measured b_{660} values increased one order of magnitude from *Class 1* (2.1 m^{-1}) to *Class 4* (20.8 m^{-1}), and are comparable with other scattering coefficients reported for turbid inland waters. For example, Sun *et al.* (2009) reported b_{660} acquired in Taihu Lake, a turbid lake in China, up to 22.0 m^{-1} with increasing inorganic concentration (around 33.0 mg.L^{-1}, which corresponds to *Class 4* in our study for which b_{660} is on average 20.8 m^{-1}). Similar to scattering, b_{b660} showed high values (e.g., 0.65 m^{-1} for *Class 3*), which are comparable to the average backscattering (b_{b700}) of 0.80 m^{-1} reported for waters where TSS reached 18.9 mg.L^{-1} in Curuai Lake, adjacent to the Tapajós 'Lake' (Carvalho *et al.*, 2015). In Estonian lakes, b_{b500} up to 0.50 m^{-1} in waters with 18.0 mg.L^{-1} of TSS (Kutser *et al.*, 2009), and which corresponds approximately to our *Class 3* (TSS = 14.0 mg.L^{-1}; b_{b532} = 0.5 m^{-1}), have been reported.

Both scattering and backscattering coefficients are primarily controlled by mineral concentration (TSS), as reported by several authors (Sun *et al.*, 2009a; Boss and Pegau, 2001; Stramski *et al.*, 2004; Bergmann, 2004; Doxaran *et al.*, 2012; Lorthiois *et al.*, 2012). Increasing TSS concentration yielded positive and significant ($p < 0.05$) correlation with $b_{p(660)}$, $b_{bp(660)}$, and $a_{p(440)}$. Correlations of optical properties with *chl-a* and $a_{cdom(440)}$ were not significant (see correlations on Table 3.4 and 3.5), which is explained by the inorganic nature of the soils subject to mining in the Tapajós watershed (CPRM, 2009; Rodrigues *et al.*, 1994).

Absorption by dissolved organic matter, $a_{cdom440}$, showed low variability among the defined water classes (~2.6 ± 0.6 m^{-1}), but its contribution to total absorption (a_{440}) is inversely correlated to TSS; it decreases from 60% in pristine streams to 40% in the Tapajós Lake, and 8% for *Class 4* (the Crepori River), for example. The modeled absorption coefficient by algal particles (a_{ph}) showed low contribution to the total absorption at 440 nm with values not higher than 3% for both mined and non-impacted rivers. This is similar to data reported for streams impacted by gold mining tailings in New Zealand, where TSS discharge is also the prevailing factor attenuating incoming light (Davies-Colley *et al.*, 1992).

The IOP of waters with high concentrations of fine sediment results in changes in the K_d, and consequently in the underwater light field. This is clearly represented by the defined five water classes representing increasing TSS (Figures 3.10 and 3.11). Measured $K_{d(PAR)}$ values varied from 2.0 m^{-1} for *Class 1* to 9.6 m^{-1} for *Class 5* (Table 3.2), which is similar to results reported for other mine-impacted areas in New Zealand, where $K_{d\ PAR}$ varied on average from 1.6 to 8.4 m^{-1} as average TSS increased from 1.2 to > 100.0 $mg.L^{-1}$ (Davies-Colley *et al.*, 1992). Other studies, specifically in the mine tailings of the Batata Lake, located in the Trombetas River watershed, showed that re-suspended inorganic particles derived from mining increased $K_{d(PAR)}$ by 35% when compared to non-impacted sections of the lake (Roland and Esteves, 1998; Guenther and Bozelli, 2004). Spectrally, the attenuation coefficient showed a similar trend: $K_{d(blue)}$, $K_{d(green)}$, and $K_{d(red)}$ varied from 2.0, 1.5, and 1.2 (*Class 1*) to 13.1, 8.0, and 7.0 m^{-1} (*Class 5*), respectively. The $K_{d(blue)}$ magnitudes are comparable to values found by Costa *et al.* (2013) for different waters in the Amazon Basin ($K_{d(blue)}$ up to 3.0 m^{-1} in clear and 15.1 m^{-1} in turbid waters). The

authors also reported $K_{d(red)}$ values lower than at our measured $K_{d(blue)}$, but still higher for white waters (9.5 m^{-1}, corresponding to *Class 5*) in comparison to clear waters (up to 1.7 m^{-1}, corresponding to *Class 1*).

The distinct spectral attenuation of the incoming light is a function of the variation on the scattering and absorption processes within the PAR range (400-700 nm). For tributaries with low or no influence of mine tailings, waters are relatively more absorbant (Figure 3.9), with a *b:a* ratio of 0.8 at the blue spectra and increasing towards the red spectra (*b:a* of 20.0 at 660 nm). The relatively lower scattering properties of these waters results in lower spectral K_d and, consequently, a more homogenous spectral light field with a significant amount of light at the green spectra (Figure 3.11a). In waters with an increase in TSS loadings from mining operations, the scattering coefficient increases, thus resulting in a *b:a* increase for *Class 4* from 7.0 to 100.0 at the blue and red spectra, respectively. In this case, the scattering process prevails over absorption specifically at the green and red wavelengths, thus explaining the observed higher underwater light availability at the green and, mainly, at the red wavelengths (Figure 3.11). This is especially true when analyzing E_o since both the upwelling and downwelling light fields are considered in the calculations (Figure 3.11a and b). In turbid waters where the *b:a* in the blue spectra is approximately 30.0, such as the case for *Class 4*, $E_{o(0.3m)}$ values became 50% higher than $E_{d(0+)}$ (Figure 3.11). In these waters, as the scattering coefficient increases relative to the absorption coefficient, the underwater light becomes more diffuse, as shown by the lower $\bar{\mu}_d$ of 0.3 (*Class 5*) compared to 0.8 (*Class 1*) (Figure 3.11d), thus constraining light to shallower depths in comparison to non-impacted waters (Figure 3.11c).

3.5.2 Assessment of light availability and other limiting factors for phytoplankton community

Having quantified the differences in the spectral E_o available for photosynthesis in impacted waters and non-impacted waters, we then investigated whether the light availability due to increased TSS tailing is limiting for phytoplankton productivity. To address this, two important points were considered: first, the relationship between the mixing layer and the critical depth, and second, the spectral quality of light and associated phytoplankton absorption efficiency. These points are discussed also considering other physical/chemical factors, such as nutrient availability and water velocity along the Tapajós River Basin.

To address the relationship between the mixing layer depth, Z_m, and the critical depth, Z_c, for a specific species was considered. This relationship indicates that for waters with $Z_m/Z_c <= 1$, light is not a limiting factor, and, in waters where $Z_m/Z_c > 1$, phytoplankton is exposed to low light levels for very long periods of time and light availability will become a limiting factor for primary productivity (Sverdrup, 1953; Reynolds *et al.*, 1994; Reynolds, 2006). For this analysis, first Z_c for a specific phytoplankton species needs to be defined. In this study, *Chlamydomonas sp.* (Chlorophyta) was considered as representing species with high light requirement for primary production (Deblois *et al.*, 2013). The scalar compensation irradiance, $E_{c(PAR)}$, required for *Chlamydomonas sp.* is ~14 $\mu Em^{-2}s^{-1}$ (Deblois *et al.*, 2013), and the depths where the $E_{o(PAR)}$ for each TSS class crosses the E_c for *Chlamydomonas* indicates the critical depth (Figure 3.13).

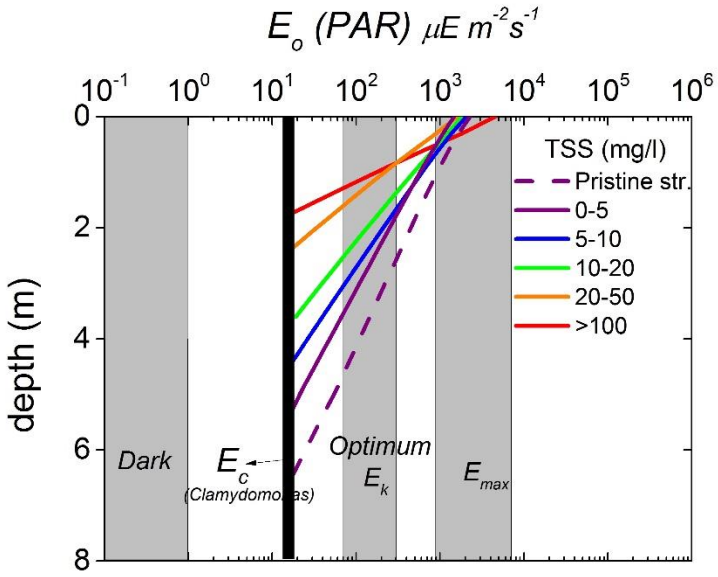

Figure 3.13: $E_{o(PAR)}$ availability from surface to bottom with depth. The compensation irradiance $E_{c(PAR)}$ for *Chlamydomonas sp.* is indicated (thick vertical black line). The correspondent critical depth, $Z_{c(PAR)}$, for each class can be drawn from the intersection of $E_{o(PAR)}$ with the $E_{c(PAR)}$ line.

The second needed parameter for this analysis is the depth of the mixing layer. In a river system, Z_m depends on the horizontal and vertical water circulation originated from bottom interaction (friction) and water flow (Robert, 2014). In the Amazon River, for example, a deep mixing layer due to turbulence and water flow has been reported (Dustan, 2009; Costa *et al.*, 2013). For the Tapajós River and tributaries, a deep mixing layer is also assumed due to the observed high turbulence and low water depth. For example, in the Jamanxim River, water flow measurements (ADCP) at the high water level showed an increase from the bottom (0.5 ms^{-1}) to the surface (2.0 ms^{-1}). On average, water velocity varies from 1.09 ms^{-1} in the high water level to 0.55 ms^{-1} in the low water level for several tributaries, such as the Crepori, Jamanxim, and Tocantins rivers (ANA, 2013). Since high homogeneity of the water quality from surface to $Z_{1\%}$ was observed

due to a lack of thermal stratification of the water column, in these rivers, Z_m was considered equivalent to the total water depth (Z) for the calculation of Z_m/Z_c.

For non-impacted tributaries, such as at upstream of the Tapajós and the Jamanxim rivers (*Class 1*), Z_m/Z_c is lower than 1.3; that is, enough light is available in approximately 75% of the water column. Pristine shallow rivers, for example, present Z_m/Z_c = 0.4 (see Table 3.2), and consequently, light availability is not a constraining factor for productivity. Impacted rivers, such as the Crepori (*Class 4*) and the Tocantins (*Class 3*), showed Z_m/Z_c of ~ 2.0 during the high water level period, which suggests a reduction of light availability to half of the mixing layer depth. Similar Z_m/Z_c values were calculated for the lower water level period given that the depth of the Crepori River, for example, is on average 4.0 m along its length (ANA, 2013). Analogous restriction of light availability has been reported in the Amazon River, and associated to the low *chl-a* concentration given that nutrients are not limiting in these waters (Costa *et al.*, 2013; Dustan, 2009; Melack and Forsberg, 2001; Junk, 1997). In the case of the Tapajós tributaries subject to mine tailings, the impact of the reduction of light availability (Z_m/Z_c ~ 2.0) on phytoplankton productivity would also diminish phytoplankton biovolume and *chl-a* when compared to non-impacted waters.

However, results indicated similar values of phytoplankton biovolume and *chl-a* for impacted and non-impacted rivers, for each specific water level period, suggesting that the light availability (PAR) reduction due to water siltation is not the only factor limiting phytoplankton growth in these tributaries. Differences are most pronounced seasonally, where the phytoplankton biovolume data and *chl-a* for both groups of rivers are higher during the low water level period, which is possibly related to the high irradiance regime

(~1300 mol.m^{-2}.mo^{-1}, Brando *et al.*, 2010). On the other hand, during the rainy season phytoplankton biovolume and *chl-a* decrease, likely because of PAR irradiance reduction of 30% (~950 mol.m^{-2}.mo^{-1}) when compared to sunny days during the dry season (Brando *et al.*, 2010; Casali *et al.*, 2011). The seasonal variation of downwelling irradiance can also explain the increase of auxiliary pigments relative to *chl-a* during the high water period (Figure 3.7b), as a physiological response to decreased light conditions in this period of the hydrological cycle (Stomp *et al.*, 2004).

The second point of the assessment of the light limitation for phytoplankton in the Tapajós River Basin is related to the spectral distribution of light. While the cell biovolume and *chl-a* did not suggest direct impact by light reduction, the observed available spectral light changes could promote changes in the phytoplankton community due to competition for the different spectral light conditions (Kirk, 2011). The usefulness of a given light field for photosynthesis is not simply a function of the total intensity of PAR, but also a function of the relationship between the spectral light availability and the specific absorption spectrum of the phytoplankton. The analysis of the relationship between the specific absorption coefficient and the $\bar{E}_o(z, \lambda)$ for the different TSS classes indicated that cyanobacteria (represented by *Synechocystis sp.*) can be more efficient than diatoms (*Chaetoceros sp.*) at harvesting the available light in the Tapajós tributaries (Figure 3.12). The higher efficiency of cyanobacteria is observed for all classes, and is accentuated in high turbidity waters (*Class 4*), where blue light is quickly attenuated and red wavelengths dominate with increasing TSS. This turbid water condition favours phytoplankton groups with pigments that has their absorption peak within the red spectra such as the light-harvesting pigment phycocyanin (620 nm), found in cyanobacteria

(Stomp *et al.*, 2004). Despite the higher cyanobacteria absorption efficiency for the Tapajós tributaries (Figure 3.12) differences among phytoplankton groups from impacted and non-impacted tributaries were not observed (Figure 3.7a). In fact, diatoms and cryptomonas similarly dominated the study rivers, suggesting that not only spectral light availability, but also other factors, such as nutrient availability and water velocity, are determinants for phytoplankton growth and diversity (Reynolds, 2006).

The upstream Tapajós waters are nutrient-poor, but the sediment-rich waters of impacted tributaries introduce high amounts of nutrients into the Tapajós River (Figure 3.8). The high nutrient concentration would favour phytoplankton growth in turbid waters as opposed to oligotrophic conditions found in clear waters such as the upstream Tapajós River. However, a higher phytoplankton biovolume was not observed in the nutrient-rich waters, thus suggesting that nutrient availability associated to low light conditions are not the only controlling factors of phytoplankton productivity. Water velocity can also limit phytoplankton growth in river systems due to phytoplankton flushing (Dokulil, 2014; Allan and Castillo, 2007; Salmaso and Zignin, 2010; Meade, 1994). For instance, in the Orinoco River Basin, the highest phytoplankton production and biomass was observed during the periods of low water levels associated with a combination of lower water velocity, increased light availability, and reduced mixing layer when compared to the high water season (Meade, 1994). In fast flowing waters with current velocity of approximately 0.5 $m.s^{-1}$ during the high water period, such as the study waters (impacted, non-impacted, and upstream Tapajós), the turbulence and high flushing rates prevent phytoplankton growth. In terms of planktonic group, even if at low concentration levels, diatoms are prevailing (*Tabelaria sp., Aulacosera granulate, and Urosolenia eriensis*) in

these fast flowing waters (Figure 3.7). The presence of siliceous exoskeleton increases diatom survival in high water flow rivers (Huisman *et al.*, 2004). The dominance of diatoms is an indicator that water velocity is also an important factor controlling phytoplankton growth and assemblage in these rivers, which is in agreement with other studies in the Amazon Basin (Kruk *et al.*, 2010; Junk, 1997). At the Tapajós main channel, where the river is wider than the tributaries, the presence of 'dead zones' (reduced water flow) at the margins (Tockner *et al.*, 2000) allows for higher phytoplankton production (> 1.0 $\mu g.L^{-1}$) when compared to the upstream tributaries (Figure 3.7a). The effects of water velocity reduction are even more evident in the calm waters of the Tapajós 'Lake' section, where the highest biovolume was measured (up to 6 $mm^3.L^{-1}$), composed mostly of cyanobacteria (Table 3.5).

At the lake section of the river, calm waters allow vertical migration and higher growth rate of phytoplankton. In this scenario, the cyanobacteria is more effective at absorbing the spectral light available as demonstrated for both impacted and non-impacted rivers (represented by TSS classes), explaining the high biovolume of cyanobacteria observed in the Tapajós 'Lake' area (Figure 3.7a). In fact, several cyanobacteria blooms have been reported at the margins of the Tapajós Lake area (Junk, 1997; Sá *et al.*, 2010), which often occurs during sunny days in the low water period, as a result of a combination of higher light and nutrient availability, and reduction of water flow.

Table 3.5 summarizes the main factors controlling phytoplankton groups and productivity in the Tapajós River Basin. It is important to mention that in this research top-down effects on phytoplankton, such as grazing, were not consider due to lack of data

but should be consider in future research. Generally, in the mined tributaries the water siltation decreases light availability, but introduces high nutrient content. However, the phytoplankton biovolume community and *chl-a* concentrations are low, and not different from non-impacted tributaries, where more light is available, but nutrient can be limiting. At the main channel (Itaituba region), slightly higher phytoplankton biovolume was observed, likely due to a combination of higher light availability (higher than impacted tributaries), nutrient availability (higher than original clear waters), and the presence of 'dead zones' with reduced water flow, allowing phytoplankton growth. The physical conditions become more favourable for phytoplankton at the Tapajós 'Lake,' where slow water velocity, associated with occasional higher nutrient and light availability, allows for optimum conditions for phytoplankton growth.

Table 3.5: Schematic representation of the main factors controlling phytoplankton group and productivity (*chl-a* and biovolume) from upstream tributaries to mouth.

	Tributaries		Tapajós - Itaituba (Main channel)	Tapajós-Lake
	not mined	mined		
Z_m/Z_c	~1.1	~ 2.0	~1.2	~ 0.4
Light availability	not limiting	reduced and possibly limiting	not limiting	Not limiting. Possibly, at deep mixed layers (>8m)
Nutrients	oligotrophic	eutrophic	oligo/meso	oligotrophic
chl-a	Low (<1.0 µg.L^{-1})	Low (<1.0 µg.L^{-1})	Med (<2.0 µg.L^{-1})	Med/high (<10.0 µg.L^{-1})
Taxon	diatoms	diatoms	diatoms/chrypto	cyanobacteria
Flushing (water velocity)	high (0.2 to 1 m.s^{-1})	high (0.2 to 1 m.s^{-1})	high with 'dead zones' (0.4 to 1.3 m.s^{-1})	low/med, allows buoyancy

3.6 Conclusions

This paper investigated the effects of water siltation on the underwater light field of different tributaries of the Tapajós River Basin, and its consequences to the phytoplankton community to fill the gap of knowledge related to ASGM impacts on water quality. The effects of introduced TSS derived from mining activities on both the inherent and apparent optical properties were quantified and E_o modeled using Hydrolight. Results showed that the inorganic nature of mine tailings is the main factor affecting the underwater scalar irradiance in the Tapajós River Basin. The TSS concentration varies seasonally during the year in a synergism between water level and mining activities: during low water level, mining activities intensify and, associated with low water volume, TSS rapidly increases, which in turn changes the optical characteristics of the water. For waters with low or no influence from mine tailings, light absorption dominates over scattering. With increased TSS loadings from mining operations, the scattering process prevails over absorption coefficient, and, at sub-surface, scalar irradiance is reduced, resulting in a shallower euphotic zone, and green and red wavelengths dominate.

Are the observed differences in light availability between mine-impacted and non-impacted rivers a limiting factor for phytoplankton? To answer this question, we first considered the relationship between the depth of the mixing layer and the critical depth for a specific *Chlamydomonas sp.* species. Impacted tributaries showed a Z_m/Z_c of approximately two times that found in the non-impacted tributaries, thus indicating a reduction of light availability to half of the mixing layer. Although a strong light reduction due to water siltation was observed in impacted tributaries, the effects on the

phytoplankton community was not clearly observed, which can be attributed to: i) low number of samples for proper comparison between impacted and non-impacted tributaries; and ii) general low phytoplankton productivity in all upstream tributaries due to a combination of high current velocity (flushing), and variable availability of nutrient and light conditions.

Secondly, we consider the efficiency of two phytoplankton groups to absorb available spectral light over the PAR range. Based on our *in situ* data and literature review, we demonstrate that cyanobacteria (*Synechocystis sp*.) could be more efficient at absorbing the spectral available light in both impacted and non-impacted waters in comparison to diatoms (*Chaetoceros sp.*). Given the high dominance of red wavelength in the modeled underwater light field, the higher efficiency of the cyanobacteria can be attributed to the presence of auxiliary pigments such as phycocyanin (with a peak of absorption centered at 620 nm). However, the dominance of diatoms in the tributaries suggests that the spatial and temporal distribution of phytoplankton in the Tapajós River Basin is not simply a function of light availability, but rather depends on a synergism of factors including flood pulse, water velocity, seasonal variation of incoming irradiance, and nutrient availability.

Chapter 4 - Time-series analysis of Landsat-MSS/TM/OLI images over Amazonian waters impacted by gold mining activities[2]

[2] Published in *Remote Sensing of Environment*, Vol. 157, 2015

4.1 Abstract

Water siltation caused by artisanal gold mining has impacted the Tapajós River Basin in Brazil for the past 40 years, however spatial-temporal information about changes in water quality and consequences to the aquatic environment is lacking. To address this, the Landsat satellite family of sensors were used to retrieve total suspended solids (TSS) in the water of the Tapajós River from 1973 to 2013. An image processing approach that includes atmospheric correction, based on the 6S model, and glint removing, based on shortwave infrared correction, was applied and validated with *in situ* radiometric data. An optimization of the atmospheric correction having dark dense forest spectra as reference was applied and allowed a robust correction of MSS, TM, and OLI signal to surface reflectance values. Sediment concentration was estimated based on a non-linear empirical regression between measured TSS and satellite surface reflectance at red band. The multi-temporal analysis of TSS showed that the sediment load in the Tapajós aquatic system is in synchrony with mining activities, and a constant seasonal variation of water siltation is observed throughout the time frame of this study. At the end of the rainy season, mining activities intensify and, coupled with low water flow, TSS increases. During the high water level, TSS concentrations were consistently lower because of high water dilution and low mining activity. In a decadal analysis, a peak of sediment concentration coincides with a peak of gold production in all sites analyzed during early 1990s. More recently, due to the current gold rush, an increase in suspended solids has been observed mainly in the Novo and Tocantins rivers, where industrial mining has been installed.

4.2 Introduction

The Tapajós River Basin, in the Amazon Basin, has been contaminated with mercury and impacted with water siltation due to discharges of artisanal gold-mining tailings into its tributaries since 1950s (Sousa and Veiga, 2009). The artisanal mining activities expanded in the 1980s when high gold prices stimulated around 30,000 workers to extract gold in this area (Bezerra *et al.*, 1998). The activity decreased in the following decades; however, due to current high gold prices, a new gold rush is taking place not only in the Amazon, but also in many other countries (Schueler *et al.*, 2011; Tudesque *et al.*, 2012).

Previous studies in the Tapajós Basin (Telmer *et al.*, 2006; Rodrigues *et al.*, 1994) reported that artisanal gold mining discharge into the rivers enormous amounts of fine inorganic sediment by removing top soil layers from the margins, and also by revolving sediment from the bottom. Because of its high scattering properties, inorganic suspended particles in the water backscatter part of the incoming light, thus reducing light availability in the water column (Kirk, 2011). (Roland and Esteves, 1998) have shown that an increase in suspended matter of nearly 34 mg/l in an Amazonian crystalline lake (Batata Lake) raises total light attenuation, and consequently reduces the phytoplankton density by approximately 50%. (Guenther and Bozelli, 2004) suggested that the decrease in phytoplankton densities recorded in Batata Lake may not be related to phytoplankton loss due to algal-clay aggregation, but rather is a consequence of decreasing growth rates because of light attenuation. The high light backscattering in turbid waters results in high water-leaving reflectance, easily detected by remote sensors as shown by Telmer and Stapper (2007) in the Tapajós River. Considering the large scale of the water siltation

impact, (Telmer and Stapper, 2007) have indicated the potential of using remote sensing data to monitor turbidity and to investigate its consequences to the ecosystems of the Tapajós River.

Although not designed for water body studies, Landsat MSS and TM have been effectively used to estimate total suspended solids (TSS) in coastal and inland waters (Binding *et al.*, 2005; Harrington Jr *et al.*, 1992). Detection of water leaving radiance from turbid waters with high confidence is possible, first because the sensor's spatial resolution (up to 80m on MSS) allows imaging rivers and estuarine areas, and second because of the signal-to-noise ratio of these sensors (250:1) (Dekker *et al.*, 2002). The use of these sensors for estimating suspended solids in the water generally follows two approaches: the empirical approach, which relies on direct correlation between measured TSS and satellite data (Mertes *et al.*, 1993; Hadjimitsis and Clayton, 2009); or analytical methods, which rely on measured water optical properties (Albert and Mobley, 2003; Doxaran *et al.*, 2012); semi-analytical approaches are also used. These studies show that green and red bands correlate well with TSS up to approximately 100 mg/l. Under higher concentrations, however, these bands saturate and NIR bands present a better predictor of TSS (Wang *et al.*, 2009).

Given the recently launched OLI (Operational Land Imager) sensor on board Landsat-8, with similar characteristics of a TM sensor, the capability of using time series based on Landsat imagery for evaluation of temporal changes and monitoring purposes is extended to the present; a time series of 40 years (1973-2013) of Landsat imagery is currently available. However, given differences in the sensor's resolution and in atmospheric conditions at the time of imagery acquisition, a proper comparison between

water leaving signals requires that all images have to be corrected for atmospheric effects and normalized to reference images or reference targets (Hadjimitsis and Clayton, 2009). Most of the images from the study area present at least 40% cloud cover. Atmospheric correction would be necessary to minimize the atmospheric effects on historical Landsat images that are not validated with *in situ* measurements.

This paper has a threefold objective: (i) define an image processing procedure that corrects Landsat digital numbers (DN) to surface reflectance ($\rho_{surf}(\lambda)$), allowing inter-comparison between Landsat data from 1973 (MSS) to 2013 (OLI); (ii) apply the procedure to build a reliable time series of water surface reflectance to retrieve TSS concentration from historical images in the Tapajós River Basin; (iii) use the retrieved suspended sediment concentrations for temporal and spatial analysis of sediment changes and gold mining activity in the Tapajós River Basin.

4.3 Theoretical background

4.3.1 Atmospheric effects and correction methods

When sensing a water body, the measured radiance, $L_{total}(\lambda)$, is the sum of the target radiance and radiance from atmospheric attenuation:

$$L_{total}(\lambda) = L_{path}(\lambda) + t \cdot L_{target}(\lambda) \quad \text{(Eq. 4.1)}$$

Where $L_{path}(\lambda)$ stands for radiance scattered by the atmosphere given a wavelength (λ), *t* is the diffuse transmittance from the target to the sensor and $L_{target}(\lambda)$ is the upwelling radiance from the water body.

Depending on the atmospheric conditions, more than 80% of the total signal can be attributed to atmospheric scattering processes (Hu *et al.*, 2001; Albert and Mobley, 2003). Note that the total radiance, $L_{total}(\lambda)$, can also include the surface reflection of the direct solar beam, $L_{glint}(\lambda)$, and, in shallow waters, the effect of light reflected from the bottom, $L_{bottom}(\lambda)$.

$$L_{total}(\lambda) = L_{path}(\lambda) + L_{glint}(\lambda) + t \cdot L_{bottom}(\lambda) + t \cdot L_{target}(\lambda) \qquad \text{(Eq. 4.2)}$$

Equation 4.2 is often normalized to incidental light to yield a dimensionless reflectance term, $\rho_{\mathrm{TOA}}(\lambda)$ (Gordon and Wang, 1994):

$$\rho_{TOA}(\lambda) = \pi \cdot L_{total}(\lambda)/E_{oTOA} \cdot cos\theta_0 \qquad \text{(Eq. 4.3)}$$

where E_{oTOA} is the top of atmosphere (TOA) solar irradiance and θ_0 is the solar zenith angle.

In order to correct $\rho_{TOA}(\lambda)$ to $\rho_{surf}(\lambda)$, atmospheric correction on Landsat-TM data over inland waters has been carried out using radiative transfer models (physically based), such as Lowtran and 6S, because of accurate outputs when local atmospheric conditions are known (Gong *et al.*, 2008). This method requires information about atmospheric conditions to model the effects and remove them from the sensor's signal. According to the 6S model, surface reflectance (ρ_{surf}) is derived from the following equation (Vermote *et al.*, 1997):

$$\rho_{TOA} = t_{gas}(O_3, O_2) \times \left[\rho_{r+a} + t_{H2O} \cdot t_{r+a} \cdot \rho_{surf}\right] \qquad \text{(Eq. 4.4)}$$

where ρ_{TOA} is the TOA reflectance; ρ_{r+a}, Rayleigh and aerosol reflectance; t_{r+a}, Rayleigh and aerosol transmittance; $t_{gas}(O_3, O_2)$, gases transmittance; and t_{H2O}, water vapour transmittance.

The 6S model provides pre-defined atmosphere conditions to be chosen according to scene location and altitude, atmospheric type, and relative humidity, to accommodate the common lack of input data about *in situ* gases and aerosol concentrations (Vermote *et al.*, 1997). For the Brazilian Amazon, for example, tropical atmospheric and continental aerosol conditions are commonly used (Lu *et al.*, 2002).

Besides atmospheric effects, surface specular reflectance, commonly called glint, has to be considered for deriving accurate water reflectance (Hedley *et al.*, 2005). The deglinting procedure as described by Hochberg *et al.* (2003) and Hedley *et al.* (2005) relies on two simple assumptions: (1) that the brightness in the infra-red is composed only of sun glint; and (2) that the amount of sun glint in the visible bands is linearly related to the brightness in the NIR band. The use of NIR for deglinting signal from turbid waters may overcorrect the visible bands (Le *et al.*, 2009) because it can present considerable signal (up to 5%) when TSS is up to 25.0 mg/l, as an example given by Bale *et al.* (1994). For that reason, Wang and Shi (2007) suggest the SWIR band (1600 nm), which is less affected or not affected by sediment-rich water bodies, to correct the VNIR bands from glinting effect by simple subtraction:

$$\rho_{deglint}(VNIR) = \rho_{surf}(VNIR) - \rho_{surf}(SWIR) \quad \text{(Eq. 4.5)}$$

4.3.2 Time-series for changes detection

The potential to use temporal series of satellite images to detect changes in surface water quality has been demonstrated, for example, by Wang *et al.*, (2004) and Dekker *et al.*, (2001). For an absolute multi-temporal analysis (i.e., detected changes have to attribute solely to variation on target`s signal), one has to perform radiometric correction (including atmospheric correction) followed by normalization of the images (Moran *et al.*, 2001; Hadjimitsis and Clayton, 2009). Normalization between images requires an application of histogram matching based on the signal from pseudo-invariant targets within the image. The assumption is that the spectra of these targets do not change over time and are therefore used to equalize histogram images (Moran *et al.*, 2001). The pseudo-invariant targets commonly used are concrete, sand and barren lands as highly reflective targets (Puttonen *et al.*, 2009), and water bodies as dark targets. However, concrete and barren lands are often not available for the study area, and using water bodies as dark objects can compromise the absolute surface reflectance of the water bodies of interest.

As an alternative to histogram matching (Liew *et al.*, 2009), an absolute atmospheric correction method is proposed based on the assumption that dense dark vegetation (DDV) is considered a spectrally invariant target, and can be used as a reference target to optimize atmospheric correction. This method was established having Amazonian dark dense forest spectra as reference targets, including spectra from the Tapajós area (Liew *et al.*, 2009), and postulates the relation, $\rho_{surf}(blue) = \ 0.33 * \rho_{surf}(SWIR)$, to estimate surface reflectance for the visible bands. Comparing the calculated ρ_{surf} to the TOA reflectance, aerosol optical thickness (AOT) can be estimated directly from the imagery.

(Masek *et al.*, 2006) show that AOT derived from Landsat TM imagery is highly correlated to *in situ* AOT measurements, and confirm the application of DDV as reference targets to optimize atmospheric correction for a multi-temporal analysis of ρ_{surf}.

4.4 Methods

Three main steps were conducted in order to define an image processing method for Landsat data that allows multi-temporal analysis of water surface reflectance and suspended solids in Tapajós River Basin (Figure 4.1): 4.4.1) field campaigns for *in situ* radiometric and TSS data collection (box (a) in Figure 4.1); 4.4.2) atmospheric correction of historical Landsat imagery based on reference images that were validated with *in situ* radiometric data (boxes (b), (c), and (d) in Figure 4.1); and 4.4.3) seasonal and decadal analysis of $\rho_{surf}(\lambda)$ and suspended solids (TSS) in the Tapajós River Basin (box (e) in Figure 4.1).

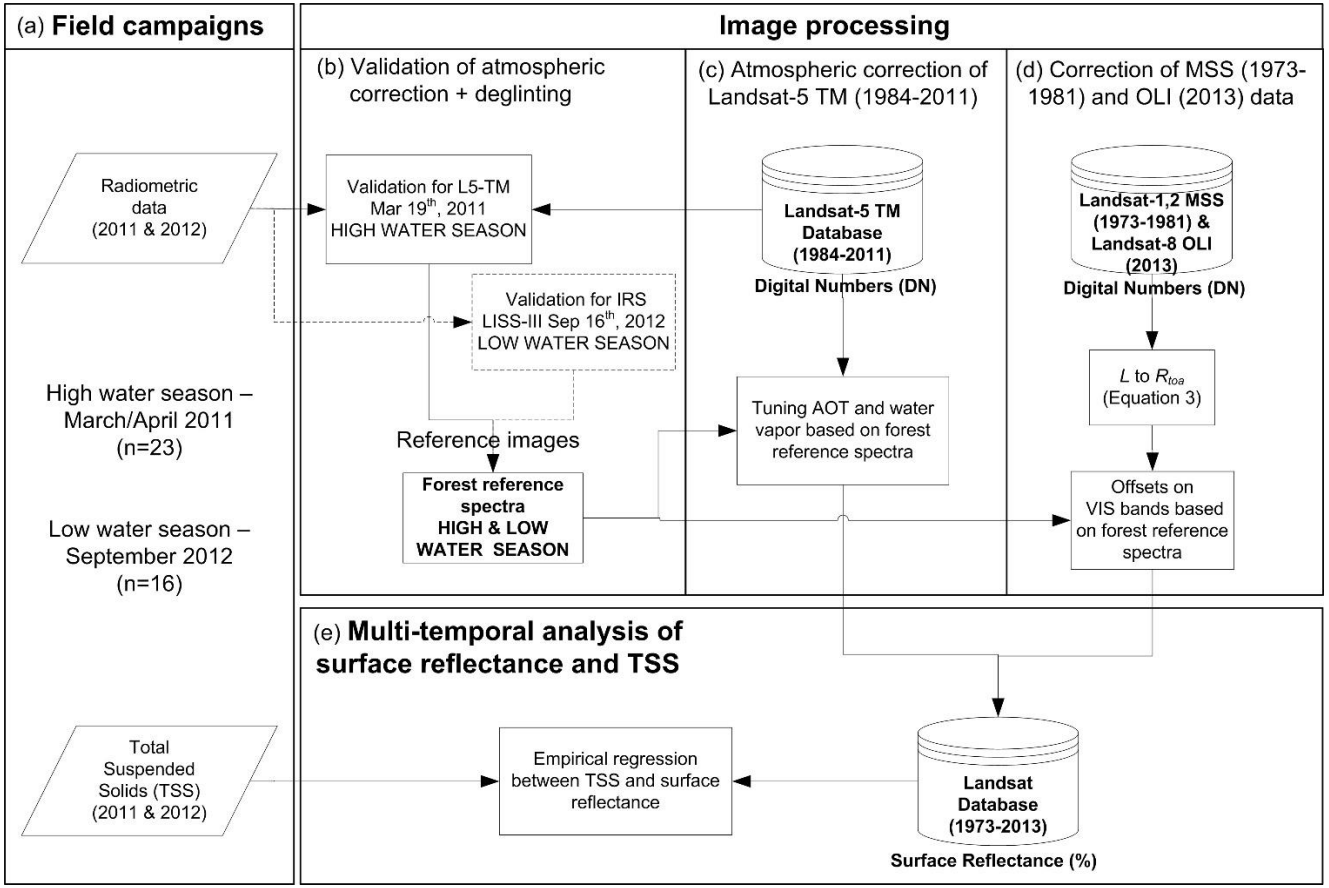

Figure 4.1: Flow-chart of the methodology applied in this study. Field data of two campaigns (a) was used to calibrate the atmospheric correction (b) that was applied to Landsat-5 TM database based on forest reference spectra (c). After incorporating corrected MSS and OLI surface reflectance into the database (d), a multi-temporal analysis of $\rho_{surf}(\lambda)$ and of TSS in 4 sub-basins and along the Tapajós River was performed (e).

4.4.1 Radiometric and TSS data

Two field campaigns were conducted in the Tapajós River Basin to measure radiometric quantities and TSS concentrations: March/April 2011, during high water level (23 sample points); and September 2012, during low water level (16 sample points) (see Figure 3.2 for sample point locations). The field campaigns were defined based on periods when the water system is less dynamic and changes in water quality are slower compared to receding or flooding periods. This choice would contribute to matching *in situ* data with concurrent satellite images. It would also help with the inter-annual comparison between images. The sample point locations were defined in order to cover the spatial distribution on the main Tapajós River tributaries before and after their discharge, and along the Tapajós River to cover its lengthwise variation. A few sample sites used for Chapter 3 (Biogeochemical approach) such as pristine tributaries were not used for the remote sensing approach (Chapter 4). Since there is no satellite data available for these streams, only 23 samples from high water level campaign were used, as opposed to 27 used in Chapter 3. During low water level, three other samples taken in large adjacent lakes during the low water level were useful for remote sensing approach but not for Chapter 3, thus resulting in n=16 samples as opposed to n=13 used in Chapter 3.

For each sample point, two water samples were taken at a depth of 0.3 m to determine TSS concentrations according to the gravimetric method (APHA, 2005). For each water sample taken, triplicates of pre-weighted (0.7 μm) filters were used to determine TSS average and standard deviations in the laboratory. By doing so, a total full

precision of TSS estimation is achieved by accounting for variability of filtering methods, and for heterogeneity of water samples.

To determine the *in situ* surface reflectance, above-water downward irradiance (E_s), and a continuous depth profile of in-water upwelling radiance, $L_{u,}$ were measured using Satlantic Hyper Pro (Satlantic Inc.). These optical sensors measure hyperspectral quantities in the interval from 396 to 800 nm with 10 nm resolution. The raw data were calibrated to sensor specification, corrected for tare conditions and binned to depth intervals. In order to minimize the wave focusing/defocusing effect (Hedley *et al.*, 2005), and uncertainties attributed to the L_u sensor tilt, triplicate measurements were taken at each sample point, and signals measured with a tilt higher than 15 degrees were removed from the dataset. After being corrected and binned to depth intervals, *Lu* values were then used to calculate upward irradiance, E_u, as follows:

$$E_u(0^+, \lambda) = 4.5 \cdot L_u(0^-, \lambda) \cdot (1 - f(\lambda, \theta)/n_w^2(\lambda)) \quad \text{(Eq. 4.6)}$$

where $f(\lambda, \theta)$ is Fresnel reflectance index of the water (0.021) and $n_w^2(\lambda)$ is Fresnel refractive index (1.34) which relates to the fraction of the incident irradiance of a collimated beam that is reflected by a level surface (Mobley, 1994). Next, surface reflectance values , $\rho_{surf}(\lambda)$, were calculated for each profile according to:

$$\rho_{surf}(\lambda) = E_u(0^+, \lambda)/E_s(0^+, \lambda) \quad \text{(Eq. 4.7)}$$

The physical quantity, $\rho_{surf}(\lambda)$, was chosen because it can be directly compared to atmospheric correction output, satellite $\rho_{surf}(\lambda)$.

4.4.2 Image processing

The image processing for atmospheric correction and normalization of all selected Landsat data (1973-2013) from DN to ρ_{surf} was performed in four steps: i) imagery selection and compilation into a database; ii) atmospheric correction of two image sets (from high water level and low water level seasons – called reference images) coincident with *in situ* radiometric measurements; iii) correction of atmospheric effects from all Landsat-5 TM images (1984-2011) using the references images and AERONET data to optimize the 6S input atmospheric parameters for each image; iv) correction of MSS and OLI data from DN to ρ_{TOA} followed by normalization to ρ_{surf} based on forest spectra derived from reference images.

Imagery database

The detectable water bodies in the Tapajós River Basin extend over six Landsat TM scenes . Landsat MSS and TM images acquired from 1973 to 2011 were downloaded from (DGI/INPE, 2013) for analysis of two specific seasons: high water level season (March to May) and low water level season (August to November). Recent cloud free images from the OLI sensor, on board Landsat-8, acquired in April and September 2013, were downloaded from Earth Explorer website (USGS, 2013a). A total of 77 images (31 from high season and 46 from low season) were incorporated into the database (Table 4.1).

Table 4.1: Number of satellite images of six orbit/rows acquired in wet and dry seasons between 1973 and 2013 used in the image processing. Note that only months that represent at least one image are shown.

		wet season			dry season			
		mar	**apr**	**may**	**ago**	**sep**	**oct**	**nov**
MSS	1973				4			
	1975				2			
	1979				2	1		
	1980				1	1		
	1981			3				
TM	1984		1	1	1	2		1
	1985			2			1	
	1986			1				
	1987		1	1			1	1
	1989				2	2		
	1990	1	1					
	1993			5	1	4		
	1995				1			
	1996		1					
	1997			3	2		1	
	1998				1			
	1999			1				
	2000				3			
	2001		1	1				
	2005		1	1		2	2	
	2011	3			1		1	
OLI	2013		2			5		

Atmospheric correction validation

To define images that can be used as references to correct historical Landsat data, two groups of satellite images corresponding to the field work periods were corrected for atmospheric effects, and validated with *in situ* radiometric data. The statistical parameters used for evaluation were the determination coefficient (R^2), regression slopes, and the RMSE (Root Mean Square Error). After atmospheric correction, glint effect was removed according to Eq. 4.6 and their statistical parameters were also compared.

For the field work performed in March/April 2011 during the high water level season, three Landsat-5 TM images (row/orbit: 227/63; 228/63; and 228/64) acquired on March 19th, 2011 were used in the validation process. However, for the campaign performed in September 2012, Landsat-5 was no longer active, which prevented full seasonal analysis of Landsat data. Alternatively, cloud-free images acquired by IRS LISS-III in the same period of the campaign were used as reference images for the low water level season.

The input data for the 6S model were provided by iteratively testing measured ranges of water vapour values and AOT from the closest AERONET (AErosol RObotic NETwork) station (NASA/GSFC, 2013), near Belterra (S 3°06', W 55°03', see Figure 3.2). Data available from 1999 to 2005 shows water vapour values of 4.2 ± 0.6 cm, and AOT of 550 nm varying from 0.1 up to 0.5 (dimensionless). For Landsat-5 TM (March 19th, 2011), a water vapour value of 3.8 cm and AOT equal to 0.22 were chosen, minimizing the average difference between *in situ* and image reflectance output. Using the same criteria, LISS images (September 16th, 2012) were atmospherically corrected by a physical-based method having water vapour value and AOT equal to 3.7 cm and 0.19,

respectively. An atmospheric correction based on Dark Object Subtraction (DOS) were also tested, but with results less satisfactory than 6S output (results not shown).

Atmospheric correction of historical Landsat-5 TM data (1984-2011)

Once the atmospheric corrections of the reference images were validated, they were used to iteratively define the set of input values for running the atmospheric correction on the 6S model. The set of water vapour values and AOT for each TM image were defined by minimizing the differences between forest spectra from the reference images and the image subjected to atmospheric correction.

The assumption is that densely forested areas present invariant spectra over decades that can be used as reference spectra to optimize atmospheric correction in individual scenes (Holben *et al.*, 1998; Liew *et al.*, 2009; Kaufman *et al.*, 1997). Although Amazonian forest spectra is very steady over decades, there are slight differences between spectra taken in rainy and dry seasons (Asner, 1998; Lu *et al.*, 2002; Lu *et al.*, 2004) that must be taken into account for proper imagery correction. As such, the images acquired during the high water level season (or rainy season) were optimized to forest spectra from Landsat 5-TM acquired in March 19th, 2011, while images acquired during the low water level season (or dry season) were optimized using LISS-III acquired in September, 2012 as reference. After optimizing the atmospheric parameters (water vapour and visibility) for each TM image, vegetation spectra were extracted and averaged differences compared with the reference images. Images that did not fall within an acceptable range (up to 50% difference at red band, which corresponds to a difference of

up to 1.5% in ρ_{surf} and have minimum impact on TSS estimation) were re-corrected with new atmospheric parameters.

Correction of MSS and OLI data

The 6S physical-based model does not have the functionality to correct MSS and OLI imagery; as such, an alternative procedure had to be adopted for atmospheric correction of these images. MSS images were first converted from DN to $L(\lambda)$ (Thome et al.,1997; Thome et al.,1994), and subsequently corrected to $\rho_{TOA}(\lambda)$ (see Eq. 3.3) according to the radiometric specifications and the date of image acquisition. OLI DN data were converted to $\rho_{TOA}(\lambda)$ according to USGS's website (USGS, 2013b). For both MSS and OLI $\rho_{TOA}(\lambda)$, the atmospheric effects were removed from VIS bands by applying an offset to match dense forest spectra with those from optimized surface reflectance (see Figure 4.3a) which resulted in $\rho_{surf}(\lambda)$. In this case, we assumed that the differences between the surface reflectance forest spectra extracted from reference images and the forest $\rho_{TOA}(\lambda)$ from MSS and OLI data can be attributed to atmospheric effects.

4.4.3 Multi-temporal analysis of surface reflectance and TSS concentration

Once surface reflectance at visible and NIR were derived from the imagery database (Landsat -MSS, Landsat-TM, and OLI), a temporal analysis was performed in four different sub-basins and along the Tapajós River (see Figure 3.2), for a total of eight different sites. The sites were chosen in order to cover the four main tributaries in terms of water discharge and mining activities (Crepori, Jamanxim, Tocantins, and Novo rivers) and also four other sites along the Tapajós River that represent the river's longitudinal

variation from upstream to the mouth (Jacareacanga, Itaituba, Aveiro, and Santarém). For each site, several pixels distributed in the sample area were selected and averaged to reduce the variability caused by adjacency or bottom effects, and also to diminish the natural variability of the water body. This procedure can also minimize the different spatial resolution of MSS (80m) and TM (30m) data. Furthermore, in order to avoid adjacency effect on the selected pixels, the analyses were restricted to rivers with at least 3 pixels width. For that reason, MSS data could not be extracted at rivers with widths up to 200 m (e.g., Jamanxim, Novo, and Tocantins rivers), for which analyses were restricted to TM and OLI data (1984 to 2013).

In order to retrieve TSS concentration from surface reflectance in the eight sample sites, a non-linear regression was established between TSS and $\rho_{surf}(red)$ derived from reference images (see Figure 4.5). The application of $\rho_{surf}(red)$ to estimate TSS in coastal and inland water using empirical regressions has been extensively reported for MSS (Harrington Jr *et al.*, 1992; Mertes *et al.*, 1993) and TM data (Masek *et al.*, 2006; Dekker *et al.*, 2002). Averaged TSS collected during the two field works (n = 39) were used to establish the empirical regression curve that allows retrieving TSS with associated error estimation (within 95% level of confidence).

4.5 Results

4.5.1 Validation of atmospheric and glint correction

The evaluation of the atmospheric and glint correction revealed that the satellite ρ_{surf} without glint correction was in close agreement with *in situ* ρ_{surf} values, especially on the red and green wavebands (Figure 4.2). High R^2 (>0.78) and low RMSE (<1.80 in

ρ_{surf} unit) were observed for both seasons where regression coefficient (slope) values were around 0.85 at these bands (Table 4.2 shows the statistical results for the linear regressions shown in Figure 4.2). At the blue (Landsat TM only) and NIR bands, the statistics show relatively poor results, with generally higher ρ_{surf} for satellite compared with *in situ* measurements (Figure 4.2a and b).

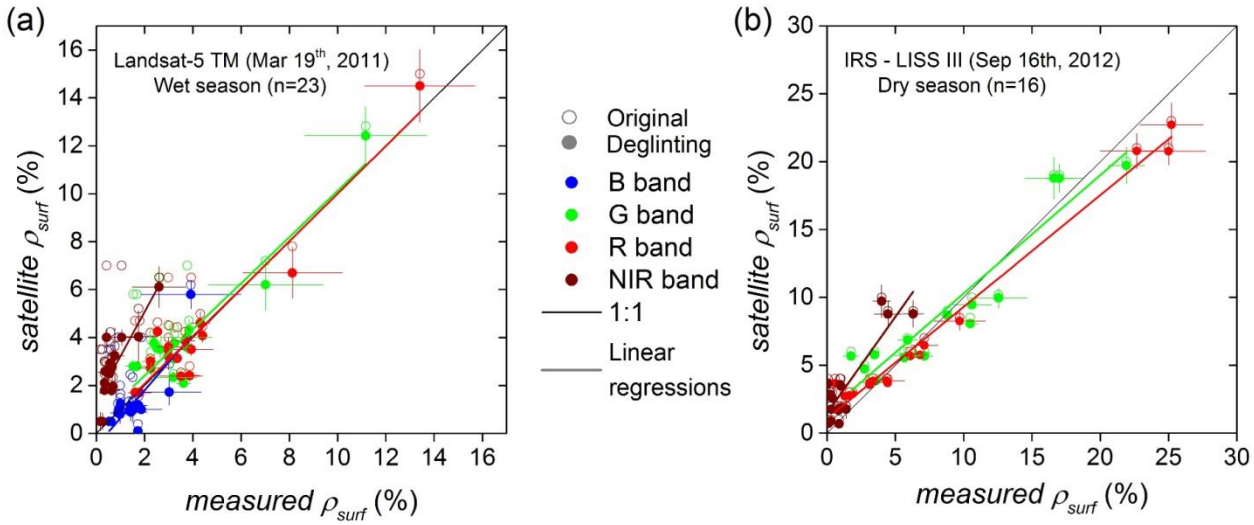

Figure 4.2: Scatter plots between measured ρ_{surf} and corrected satellite ρ_{surf} at VNIR channels for (a) Landsat-5 M, (b) IRS – LISS III. ρ_{surf} before (empty circles) and after (filled circles) glint removing is also shown. Linear regression and standard deviation (error bars) are plotted only for deglinted data. See Table 4.2 for statistical parameters of linear regressions. Note the different ρ_{surf} range between (a) and (b).

Table 4.2: Statistical parameters (intercept, slope, R2, RMSE) for linear regressions before and after deglinting between measured $\rho_{surf}(\lambda)$ and $\rho_{surf}(\lambda)$ derived from two imagery sets: Landsat-5 (wet season) and LISS (dry season). Determination coefficients highlighted in red are significant at 0.05 level.

		Landsat-5 TM (Mar, 19th 2011) - Wet season (n = 23)				IRS LISS-III (Sep, 16th 2012) - Dry season (n= 16)			
Channel		intercept	slope	R^2	RMSE	intercept	slope	R^2	RMSE
Blue		1.26	0.76	0.44	1.34	-	-	-	-
	deglint	-0.51	1.16	0.80	0.75				
Green		2.1	0.82	0.78	1.56	1.57	0.87	0.88	1.77
	deglint	0.5	0.96	0.93	0.85	1.31	0.87	0.88	1.79
Red		1.7	0.88	0.88	1.36	1.35	0.82	0.97	0.89
	deglint	0.8	0.99	0.93	0.87	1.06	0.82	0.97	0.89
NIR		2.8	1.4	0.27	1.36	1.77	1.41	0.75	1.46
	deglint	1.38	1.84	0.82	0.79	1.47	1.41	0.76	1.42

Figure 4.2 show examples of *in situ* ρ_{surf} spectra under different TSS concentrations plotted with glint corrected satellite $\rho_{surf}(\lambda)$ for the two field campaigns. High accordance between satellite and *in situ* $\rho_{surf}(\mathrm{red})$ is observed. According to Table 4.2, the correction for glint effect significantly improved the statistical results. At the blue band, R^2 values increased from 0.44 (without glint correction) to 0.80 (with glint correction), and RMSE decreased from 1.34 to 0.75 (in ρ_{surf} unit). Improvements were also observed for the green and red bands, where R^2 were higher than 0.88 and RMSE were lower than 1.0 (in ρ_{surf} unit) for both seasons. Because the images acquired in March 2011 (Landsat-5 TM) present high cloud coverage distributed unevenly over the scene, the SWIR signal can be attributed not only to glint effect, but also to atmospheric effects that have not been removed by the 6S model, and therefore minimizes the heterogeneity distribution of atmospheric conditions (Ruddick *et al.*, 2000). For LISS-III images, the $\rho_{surf}(SWIR)$ values were always lower than 1.0 (in ρ_{surf} unit), indicating that glint was not affecting the image quality. The statistical results corroborated this, however we followed the imagery analysis with the glint corrected LISS-III image given that the observed intercept values decreased when compared with no glint correction. All the linear regressions of deglinting data (shown in Figure 4.2) were tested for normal distribution of residuals at a 0.05 level of significance. The results confirm that high and low water level data were drawn from a normally distributed population (tests not shown), thus indicating no over or under estimation of reflectance values.

4.5.2 Atmospheric correction of historical Landsat-5 TM data (1984-2011)

Once the atmospheric correction for the reference images was validated with *in situ* data, the forest spectra extracted from these images (Figure 4.3a) were used as a reference to optimize the 6S atmospheric inputs (AOT, water vapour) for correction of the other 76 historical Landsat-5 TM images (Table 4.1). For this step, the imagery database was separated into two groups according to the time of imagery acquisition: high and low water level season. The rational for this division was the observed slightly higher forest spectra values at low water level (LISS-III) compared to forest spectra at high water level season (Landsat-5 TM). For example, $\rho_{surf}(green)$ reached values as high as 5.2% in the low water level, whereas for the images acquired during high water level season, values of 3.1% were observed (Figure 4.3a).

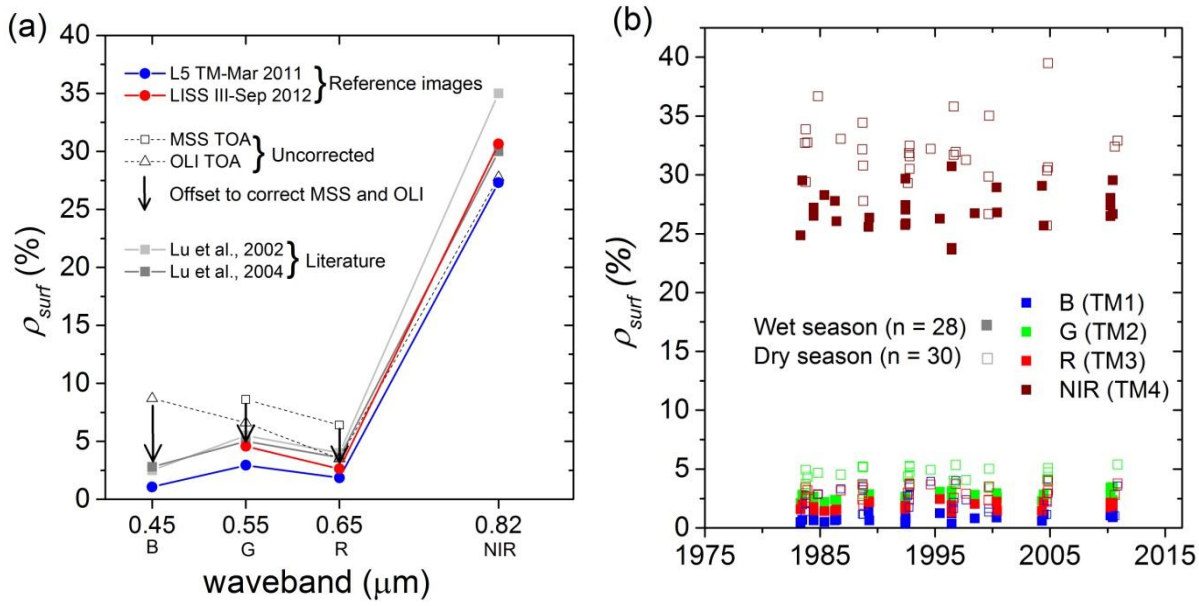

Figure 4.3: (a) Dense forest spectra extracted from wet season (Landsat) and dry season (LISS-III) used as reference for optimizing atmospheric parameters on Landsat historical data. Examples of uncorrected MSS and OLI TOA reflectances, and dense forest from the Brazilian Amazon found in literature (Lu et al., 2002 and 2004) are also shown. (b) Dense forest spectra for wet and dry seasons extracted from historical Landsat-5 TM images having spectra shown in (a) as reference. See Tables 4.3 and 4.4 for differences between reference images and historical TM data.

The forest ρ_{surf} extracted from the historical images (Figure 4.3b) was compared with the forest spectra from the reference images, again divided into low and high water level seasons (Tables 4.3 and 4.4). High accordance between forest spectra extracted from the corrected images and the reference images for both low (n=30) and high water levels= (n=28) periods was achieved. The highest differences between reference and individual images were observed at the blue band, where the average difference was about 33%. For the remaining bands, the differences were on average 9% for both low and high water level seasons.

Table 4.3: Differences between dense forest spectra ($\rho_{surf}(\lambda)$), extracted from wet season reference images (L5 TM March 2011) and historical images acquired at the same season. SD – standard deviation. NIR stands for Near Infra-Red.

					Blue	Green	Red	NIR
Reference image (Landsat 5 Mar 2011) ρ_{surf} ± SD					**1.2±0.2**	**3.1±0.3**	**2.0±0.3**	**27.3±2.3**
					Percentage difference from reference image			
	orbit	**row**	**date**	**season**	**(x_m-x_i/x_m).100**			
L5-TM	229	64	04/06/1984	wet	59%	9%	0%	-8%
L5-TM	228	64	30/05/1985	wet	27%	28%	27%	0%
L5-TM	227	64	10/05/1986	wet	79%	31%	31%	-4%
L5-TM	229	64	09/04/1987	wet	63%	25%	28%	-2%
L5-TM	228	64	09/03/1990	wet	-24%	12%	-14%	6%
L5-TM	229	64	11/05/1993	wet	77%	30%	17%	6%
L5-TM	229	64	19/05/1996	wet	-6%	-1%	-25%	4%
L5-TM	228	64	31/05/1997	wet	-4%	-2%	3%	-13%
L5-TM	227	64	30/05/1999	wet	44%	9%	-2%	2%
L5-TM	228	64	10/05/2001	wet	-27%	18%	28%	2%
L5-TM	228	64	03/04/2005	wet	68%	27%	29%	-6%
Historical average ρ_{surf} ± SD					**1.0±0.4**	**2.8±0.5**	**1.9±0.4**	**27.2±1.8**

Table 4.4: Differences between dense forest spectra ($\rho_{surf}(\lambda)$), extracted from dry season master images (LISS-III September 2012) and historical images acquired at the same season. LISS-III sensor does not have a blue band. SD – standard deviation. NIR stands for Near Infra-Red.

					Blue	Green	Red	NIR
Reference image (LISS-III Sept 2012) ρ_{surf} ± SD					**-**	**4.6±0.3**	**3.1±0.2**	**30.6±1.8**
					Percentage difference from reference image			
	orbit	**row**	**date**	**season**	**$(x_m-x_i/x_m).100$**			
L5-TM	228	64	16/09/1984	dry	-	-8%	-9%	-11%
L5-TM	227	64	14/10/1985	dry	-	-2%	8%	-20%
L5-TM	228	62	11/10/1987	dry	-	1%	-1%	-8%
L5-TM	229	64	21/09/1989	dry	-	37%	37%	9%
L5-TM	229	64	16/09/1993	dry	-	17%	24%	-4%
L5-TM	229	64	05/08/1995	dry	-	-8%	-18%	-5%
L5-TM	228	64	03/08/1997	dry	-	12%	18%	-4%
L5-TM	227	64	31/08/1998	dry	-	11%	7%	-2%
L5-TM	229	64	18/08/2000	dry	-	26%	25%	3%
L5-TM	229	64	19/10/2005	dry	-	-11%	-28%	0%
L5-TM	229	64	01/08/2011	dry	-	35%	11%	-6%
Historical average ρ_{surf} ± SD					**2.6±0.9**	**4.3±0.7**	**3.0±0.6**	**31.9±2.7**

4.5.3 MSS and OLI imagery correction

In total, 14 MSS and 7 OLI $\rho_{surf}(\lambda)$ images were incorporated into the database by applying offsets on uncorrected $\rho_{TOA}(\lambda)$ based on forest spectra. Because the atmospheric scattering effects are more prominent in the blue wavebands, the correction offset were consistently higher for blue band when compared to green and red bands. Figure 4.3a depicts MSS and OLI $\rho_{TOA}(\lambda)$ corrected to $\rho_{surf}(\lambda)$. For example, MSS and OLI $\rho_{TOA}(\text{green})$ were corrected from 8.1 and 6.2%, respectively, to $\rho_{surf}(\text{green})$ of 4.6%.

4.5.4 Spatial and temporal analysis of surface reflectance

Once the correction for imagery database (Landsat MSS, TM, and OLI) was validated, a multi-temporal analysis of $\rho_{surf}(\lambda)$, from 1973 to 2013, was performed for four tributaries (Jamanxim, Tocantins, Crepori, and Novo rivers) and along the Tapajós River. Given the coarse spatial resolution of the MSS data (80m), the Jamanxim, Tocantins, and Novo rivers were not sampled due to signal interferences from surrounding vegetation on the water reflectance from the narrow rivers. Therefore, for these rivers, time series analysis of $\rho_{surf}(\lambda)$ starts in 1984 with TM data.

In general, besides the signal differences among rivers, two major temporal variations of water $\rho_{surf}(\lambda)$ were observed: seasonal, between low and high water level season, and annual (Figure 4.4). Although differences in magnitude among the rivers were observed, $\rho_{surf}(VNIR)$ values from the low water season were consistently higher than those from the high water season, especially at red and green bands. In terms of inter-annual analysis, a clear peak of ρ_{surf} in all bands was observed between 1985 and 1995 for the eight sites analysed, with the least effect on Jacareacanga, located upstream of Tapajós River before the confluence with the heavily mined Crepori River.

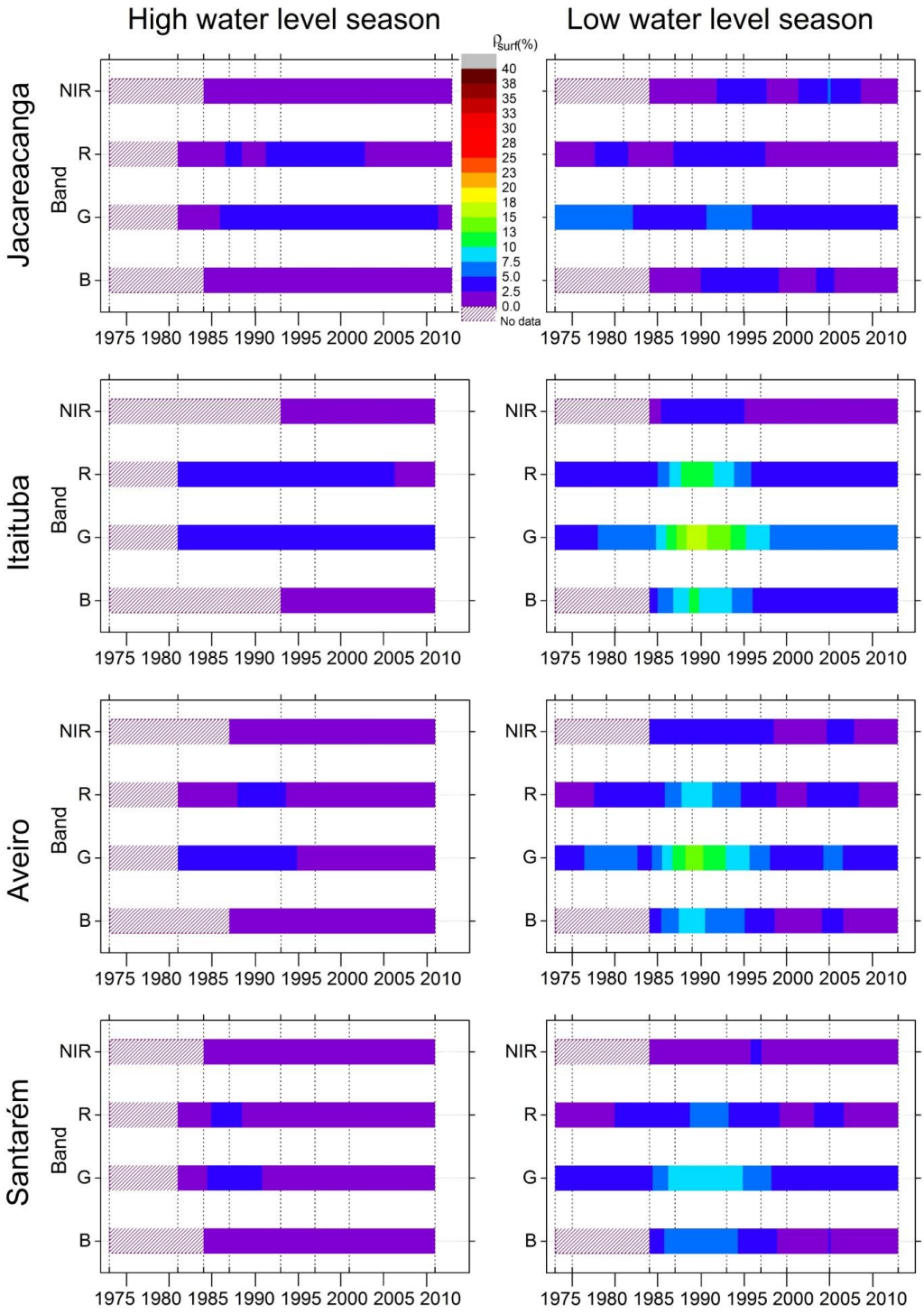

Figure 4.4: Seasonal and inter-annual variation of ρ_{surf}(VNIR) bands in four sub-basins: Jamanxim, Novo, Tocantins, and Crepori rivers; and along the Tapajós River: Jacareacanga, Itaituba, Aveiro, and Santarém cities used for location reference (see Figure 3.2).

For the Jamanxim River, located in a sub-basin with low mining activity, the $\rho_{surf}(\text{red})$ values were lower than 4.0% in both seasons, but a significant difference ($p<0.05$) was observed between high (1.7%) and low (3.0%) water level seasons from 1984 to 2013 (Figure 4.4). At the other extreme, in the Crepori sub-basin, characterized by intense mining activity, the $\rho_{surf}(\text{red})$ values increased from 4.0% in 1973 to 27.0% in 1984, reaching its maximum value in 1993 (36.0%), during low water level season. Although values decreased in the following decades, their magnitudes were still high (up to 20%) until 2013. The Tocantins and Novo rivers presented similar results, the highest of $\rho_{surf}(green)$ and $\rho_{surf}(\text{red})$ in the early 1990s. However, for the Tocantins and Novo rivers, a recent (2005-2013) increase of reflectance was observed for the same bands, indicating that considerable mining activity is currently taking place in these sub-basins.

The analysis of $\rho_{surf}(\lambda)$ along the Tapajós River (Jacareacanga, Itaituba, Aveiro, and Santarém) showed values not higher than 5% from the upstream (Jacareacanga) to the mouth (Santarém) at the high water period for the entire time series (1973-2013). During the low water period, however, significantly ($p<0.05$) higher values ($\rho_{surf}(\text{green}) = 5\%$ on average) were observed compared to the high water level season (3% on average). Although low $\rho_{surf}(\lambda)$ were observed upstream (Jacareacanga) at green and red bands, a considerable increase of reflectance was observed in Itaituba and, less pronounced, in Aveiro (which is 200km downstream from Itaituba), mainly in the period between 1985 and 1995. Taking into account the river's network and discharge, the $\rho_{surf}(\lambda)$ variation from upstream Tapajós (Jacareacanga) observed for both seasons is in accordance with the spatial variation of the tributaries shown in Figure 4.4a.

4.5.5 Spatial and temporal analysis of TSS

TSS concentrations were measured at 39 sample points and correlated with reflectance derived from satellite sensors (Landsat-5 TM data for high water level and LISS-III data for low water level season). Measured TSS concentrations were higher in those rivers with intense gold mining activity, such as the Crepori River. During high water level, TSS values of 35.3 mg/l were observed in this river, whereas in the low water period, concentrations up to 115.2 mg/l were measured. Minimum values are similar for both periods (Table 4.5).

Table 4.5: Descriptive statistics (average, standard deviation, minimum, and maximum values) of TSS concentration for the two field campaigns (high and low water level).

	TSS (mg/l)	
	high water	low water
average	9.3	24.4
SD	10.1	42.7
min	3.1	2.7
max	35.3	115.2
n	23	16

The best empirical correlation between TSS and $\rho_{surf}(\lambda)$ was given by a power function (R^2 = 0.94, RMSE = 1.33%, $p<0.05$) see Figure 4.5) using the red band. Although the curve is based on satellite $\rho_{surf}(\mathrm{red})$ up to 22%, we assumed that this function can be extended to values up to 35%, which corresponds to approximately 300 mg/l of TSS. It is worth noting the very similar correlation of TSS with in situ $\rho_{surf}(\mathrm{red})$ depicted by the dashed curve in Figure 4.5. The TSS range available during fieldwork was only up to 110 mg/l, which corresponds to approximately 24% of satellite surface reflectance data. Above 35%, the empirical regression curve does not provide reliable

TSS estimation because the regression's confidence range (confidence level = 95%) yields errors up to 50% (see confidence interval in Figure 4.5).

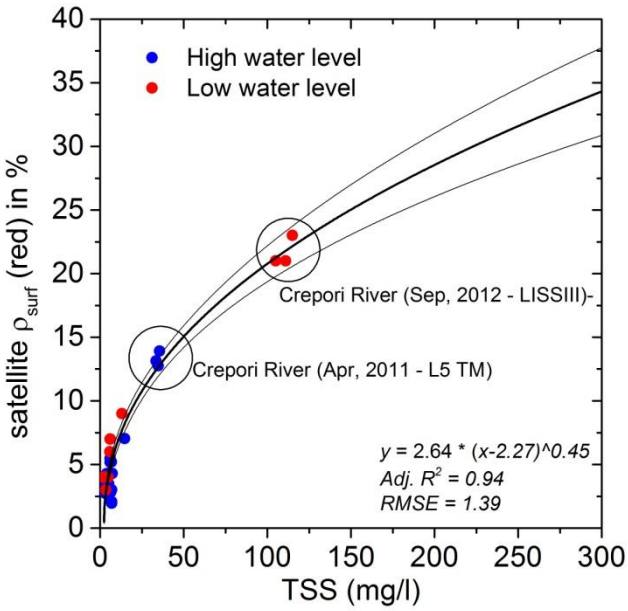

Figure 4.5: Non-linear fit between TSS (n=39) and reflectance (red band) derived from satellite sensors (TM data for wet season and LISS-III data for dry season).

Based on the defined power-law function (equation in Figure 4.5), TSS values from the historical Landsat imagery at the eight sites analysed were retrieved (Figure 4.6). Following similar observed $\rho_{surf}(red)$ dynamic (Figure 4.4), TSS exhibited higher concentrations at low water level than at high water level periods (Figure 4.6). In the low water level season of 1989, for example, TSS values of about 301.0 mg/l were estimated for the Crepori River. After the Crepori discharge into the Tapajós River, the high TSS is mixed with the relatively low TSS waters of the Tapajós, and at approximately 260 km downstream, the TSS concentration decreased to about 33.5 mg/l at Itaituba City and down to 6.6 mg/l at the Santarém area. Similar values were observed for the high water season, but at lower TSS concentrations (Figure 4.6); the Crepori River exhibited TSS

values up to 100.0 mg/l, and after the confluence with the Tapajós River, TSS values decreased to 4.4 mg/l in Itaituba and to 2.5 mg/l in Santarém.

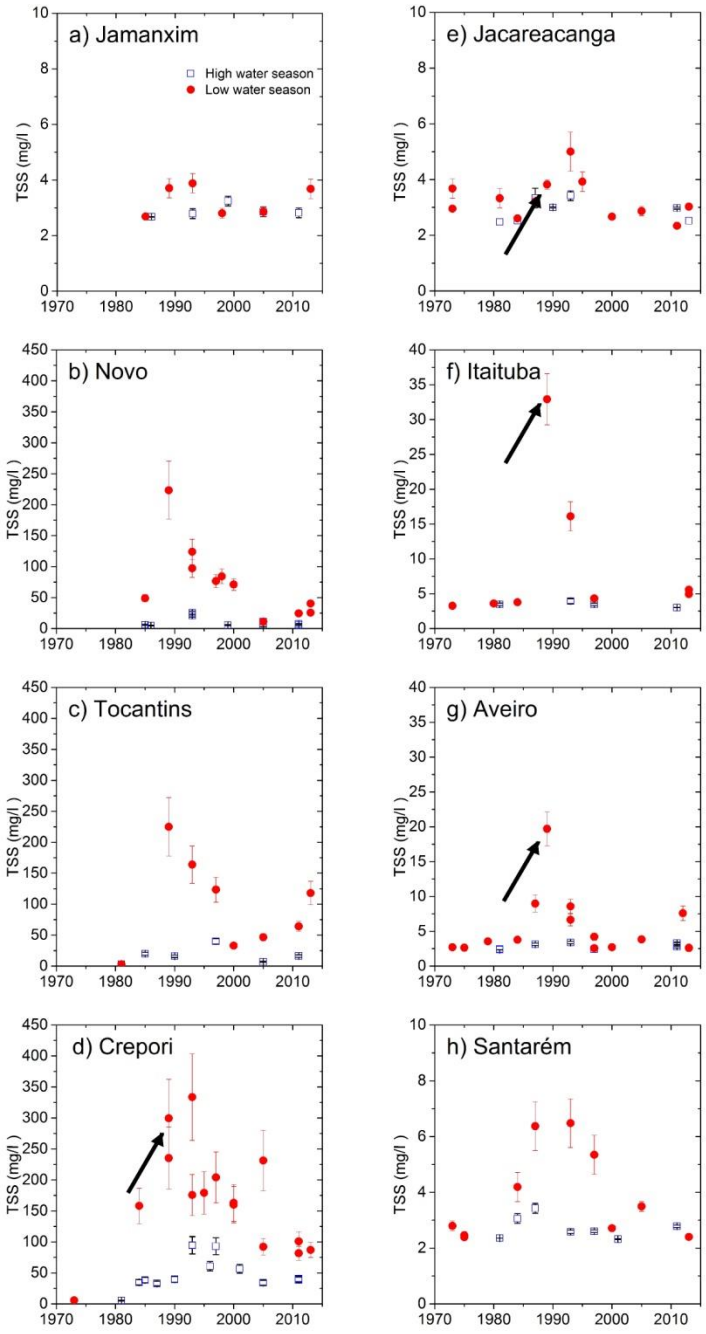

Figure 4.6: TSS concentrations at eight locations retrieved from Landsat database (1973 - 2013) using the regression shown in Figure 4.5. Examples given in the text are indicated by arrows. Note that the magnitude of the Y axis changes for the different rivers.

The spatial and seasonal dynamic is illustrated in Figure 4.7, which corresponds to the seasonal $\rho_{surf}(red)$-based TSS variation (equation in Figure 4.5) in the Crepori River and Tapajós River, from Landsat-8 images acquired on June 12th (high water) and September 16th (low water), 2013. An evident increase of TSS concentrations was observed from June 2013 (TSS = 38.0 mg/l) to September 2013 (96.0 mg/l). It is worth noting that the sediment plume in September reaches 100km downstream in the Tapajós River after the confluence with the Crepori River, at a concentration of approximately 45.0 mg/l, decreasing to about 15.0 mg/l at the river's confluence (indicated in the Figure 4.7).

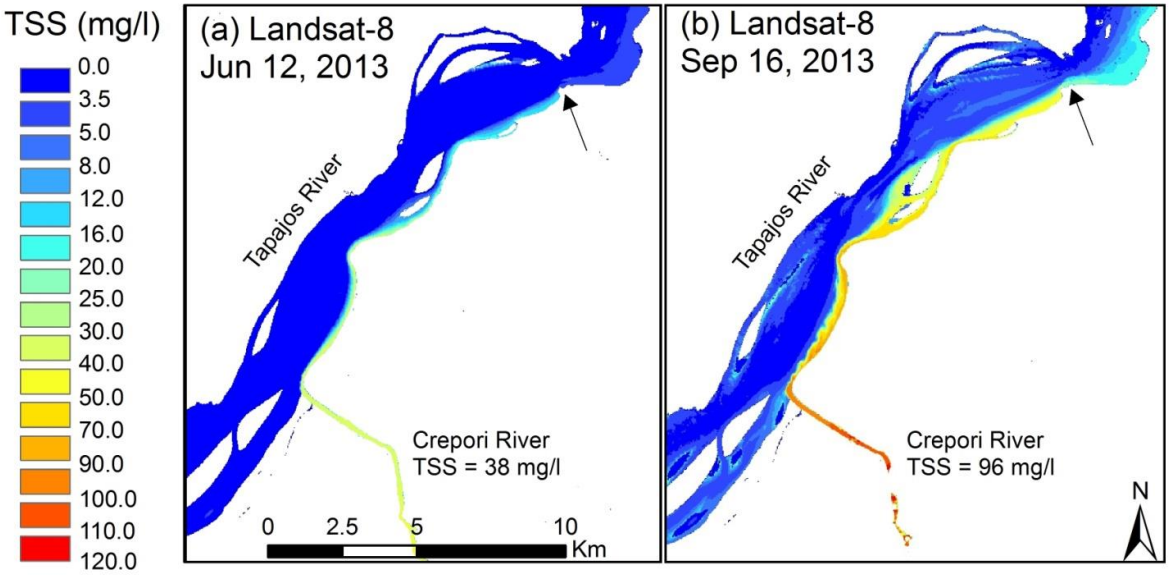

Figure 4.7: TSS concentration at the Crepori River mouth into the Tapajós River retrieved from two Landsat-8 images: (a) June 12th 2013, high water level and (b) September 16th 2013, low water level period using the regression shown in Figure 4.5. Arrows indicate the confluence in the river that mixes the water and TSS decreases.

4.6 Discussion

4.6.1 Atmospheric issues

Atmospheric correction is a key component prior to the analysis of satellite imagery time-series. However, difficulty rises due to the lack of information about past atmospheric conditions at the time of imagery acquisition, especially for remote areas such as the Amazon. To overcome the absence of information about atmospheric conditions required as input to physical-based atmospheric models, an approach that relies on initial validation of a set of 6S atmospheric-corrected satellite images acquired concurrently to *in situ* reflectance data was applied.

The *in situ* reflectance presented comparable values to those reported in literature for Amazonian waters (Rudorff *et al.*, 2009b; Barbosa, 2010; Lobo *et al.*, 2012) where *in situ* spectra data used for validation of the satellite images presented high variability at high magnitude values (see Figure 4.2). This is likely due to signal-to-noise ratio reduction related to measuring under-water radiance in high TSS conditions (Reinart *et al.*, 2004; Sun *et al.*, 2009b). In high turbidity Amazonian water conditions, the under-water light is intensively attenuated in the visible spectrum, reducing signal-to-noise ratio and increasing data variability. (Costa *et al.*, 2013), for instance, have shown that sediment-rich waters (TSS = 138.8 mg/l) present a diffuse attenuation coefficient ($K_{d\,(blue)}$) five times higher (15.3 m^{-1}) than in a clear water river (TSS=4.1 mg/l; $K_{d\,(blue)}$=3.0 m^{-1}).

Despite the variability of *in situ* reflectance, high correlations between *in situ* and satellite ρ_{surf} at the green and red bands indicate that the atmospheric correction approach was successful. Green and red bands also correspond to the spectrum where

suspended solids present a high scattering property, which increases the signal-to-noise ratio of the signal detected by remote sensors. On the other hand, for blue and NIR bands the atmospheric correction resulted in a general over estimation of ρ_{surf} when compared to *in situ* ρ_{surf}. The not significant correlation between measured and satellite $\rho_{surf}(\text{blue})$ suggests that the atmospheric method did not properly model the effects of aerosol and gases scattering (Guanter *et al.*, 2010) and absorption effects by nitrogen dioxide (Gao *et al.*, 2009; O'Neill and Costa, 2013). Studies that validated atmospheric correction with *in situ* radiometric measurements attributed the errors at blue wavelengths either to the inability of the physical-based approach to model aerosol and gases concentration (Bailey and Werdell, 2006; Ruddick *et al.*, 2000), or to unavailability of a suitable aerosol model (Guanter *et al.*, 2010). The effects will be more accentuated in moderate concentrations of absorbing aerosols as higher concentrations are often identified as clouds.

At the NIR region of the spectrum, the poor correlation between measured and corrected satellite $\rho_{surf}(NIR)$ is likely due to the low magnitude (up to 5%) and to the adjacency effect on the reflectance signal. The low magnitude and low variation of $\rho_{surf}(NIR)$ is mostly due to strong absorption of NIR radiation by water molecules (Mobley, 1994). Although considerable $\rho_{surf}(NIR)$ has been observed in turbid waters, as reported in literature (Dekker *et al.*, 2001; Liew *et al.*, 2009; Wang and Shi, 2007), the NIR spectrum from clear waters (TSS<7.0 mg/l) should be close to zero. Given the small width of the tributaries in this study, the overestimated satellite $\rho_{surf}(NIR)$ in the clear waters can thus be attributed mostly to the adjacency effect. (Santer and Schmechtig, 2000) investigated the contribution of the adjacency effect to the NIR water reflectance in the middle of a circular lake. For a lake with 5 km radius, the supplementary contribution

of the surrounding reflectance to the NIR water signal was roughly half of the water signal. The adjacency contribution can be even higher at lower distances, which is the case of the Tapajós River Basin, where some tributaries are no larger than 110 m in width (e.g., Tocantins and Novo rivers). The representation of the adjacency effect is minimal on VIS bands, because forest spectra present low ρ_{surf} (up to 5%) as opposed to NIR, where values are as high as 40%. As such, caution should be taken when using NIR bands to derive turbidity from narrow rivers, given the difficulty in defining the spatial contribution of the adjacency signal to the $\rho_{surf}(NIR)$ from water bodies.

The glint effect correction approach was successful, as shown by the improved correlations between measured and satellite reflectance for the whole spectral range. The improvement was more evident on Landsat-5 TM (March 2011), when considerable cloud cover was observed in these images. Besides the influence of a possible glint signal, the SWIR band (used in the deglinting process) might also contain atmospheric signal that was not totally removed in the atmospheric correction approach. Because the 6S correction method considers AOT and water vapour to be homogenous in the entire scene, this deglinting procedure can correct non-homogenous atmospheric effects within a satellite image, and as such provides a more accurate estimate of water ρ_{surf} (Wang and Shi, 2007; Kutser *et al.*, 2013). This is particularly important to remote sensing studies in the Amazon, where high humidity and high cloud cover introduces atmospheric variability within the same scene (Lu *et al.*, 2002).

4.6.2 Multi-temporal analysis of $\rho_{surf}(\lambda)$ and TSS in the Tapajós River Basin

The results of the corrections performed in historical Landsat imagery (1973-2013) demonstrated that forest spectra from historical Landsat-5 TM (1984-2011) behaved as an invariant spectral feature over decades, considering the seasonality. Therefore, any $\rho_{surf}(\lambda)$ variation in spectra extracted from water bodies can be attributed mostly to variation in optical constituents in the water and not to environmental conditions, such as atmospheric and glint effects. According to the validation procedure (section 5.1), the certainty of corrected ρ_{surf} is higher for the red and green bands compared to the blue and NIR, where satellite ρ_{surf} are overvalued.

The magnitude and spectral shape of $\rho_{surf}(\lambda)$ derived in this study is similar to other studies in the Amazonian waters (Rudorff *et al.*, 2009b; Lobo *et al.*, 2012). In general, increasing TSS concentration up to 50.0 mg/l affects primarily the green and red wavebands. Under very high turbidity conditions (TSS >100.0 mg/l), the light scattered by suspended particles also considerably affects the NIR spectrum region. For instance, spectra derived from sediment-rich waters in this study (TSS up to 110.0 mg/l) present values (up to 23.1% at red band) in accordance with other studies in the Amazon River floodplain (Barbosa *et al.*, 2010; Mertes *et al.*, 1993; Rudorff *et al.*, 2009b). The observed reflectance values are likely associated with the origin of the inorganic particles. TSS derived from mining activities in the Tapajós is composed mostly of silt/clay particles (Telmer and Stapper, 2007), which in turn are more efficient at scattering light than organic and sand particles (Gordon *et al.*, 2009). A recent laboratory investigation on the scattering properties of two suspended particle sizes has shown that clay/silt particles are 40% more efficient in scattering light than medium-sized sand

particles at 660 nm (Bowers and Binding, 2006; Lobo *et al.*, 2014). As a result, a high $\rho_{\text{surf}}(red)$ is expected from clay-rich water than from sand-rich waters, for example.

The imagery-derived surface reflectance from the Tapajós River Basin suggests that its variability is mainly affected by the scattering properties of suspended solids that vary seasonally and are also increased due to mining activities. Another possible source of inorganic matter to the water is deforestation (Neill *et al.*, 2011). However, the possible increase in TSS caused by deforestation is not at the same magnitude as the increase in TSS caused by mining activity. For example, the Jamanxim River, which is characterized by highly deforested areas but with low mining activity in the sub-basin area (see Figure 2.1), presents low $\rho_{\text{surf}}(\lambda)$ that are similar to those from Tapajós upstream (Jacareacanga), even in the low water level season when mining activity can be more intense. The natural clear water condition facilitates the detection of sediment plume caused by gold mining. The same rationale is likely not valid for white water (muddy water) rivers, such as the Madeira River in the Amazon. Because the Madeira River is naturally very turbid as a consequence of its drainage in the Andes, detection of gold mining tailings into the river is likely a more difficult task when comparing to the Tapajós clear water system.

Seasonal variation of water quality and optical properties have been investigated in Amazonian water bodies (Costa *et al.*, 2013; Casali, 2011; Novo *et al.*, 2006b; Barbosa, 2010; Kilham and Roberts, 2011). In general, differences between rising and ebbing periods in terms of TSS and light attenuation can be explained by factors such as hydrological regime flow, sediment transportation, and bio-geochemistry of the water (Costa *et al.*, 2013). In the Tapajós River Basin, the seasonal variation of TSS, and

consequently, $\rho_{surf}(\lambda)$ can be explained by the synergism between hydrology, biogeochemistry dynamics, and gold mining activities. In terms of hydrological dynamic, (Costa *et al.*, 2013) reported that the increase of TSS in the Tapajós River (Santarém area) from ebbing (1.6 mg/l) to rising (4.1 mg/l) water periods can be explained by the suspended solids input carried during rain events, and also by sediment input from the floodplains as the waters rises.

Gold mining activities are also temporally dynamic. During the rainy season, most of the gold mining activity stops (Bezerra *et al.*, 1998) and, associated with the increase in volume of water in the rivers, the sediment concentration dilutes. As a consequence, low reflectance caused by particle scattering is observed in this period. When the rainy season ends, the miners start working, and consequently high concentrations of sediment are observed in the rivers. This factor associated with low volume water results in TSS concentrations above 100 mg/l.

Besides seasonal variation, the results show a decadal change of TSS (Figure 4.6). The highest TSS concentration is observed at the end of the 1980s and beginning of the 1990s for all sites, except for the Jamanxim River where a quasi-constant decadal TSS is observed. During this period, the sediment plume derived from the Crepori, Novo, and Tocantinzinho rivers reached further downstream the Tapajós (Santarém site) where a TSS concentration above 6.0 mg/l was observed. The turbidity increment can be directly related to mining activity in the region. According to official estimates on gold production in the Tapajós region, the peak of gold production happened during this same period – end of the 1980s and beginning of the 1990s (Silva, 2012). (Bezerra *et al.*, 1998) reported that a total of 67 million m^3/year of sediment have been removed from the

margins of many tributaries in the 1980s because of mining activities. In addition to sediment discharge from the tributaries, (Telmer and Persaud, 2013) indicated that during that period, intense mining in the Tapajós River (Itaituba area) was performed by 'balsas' and pitch loaders, which are techniques that result in high TSS concentration in the water. Such activities were prohibited in the 1990s, which in turn directly reduced the TSS concentration (and $\rho_{surf}(\mathrm{red})$) in the following years, even with high TSS concentration discharges from Crepori River (see Figure 4.6- Itaituba).

Another important factor that has triggered gold mining activity is the price of gold. In the 1980s, the price jumped from US$500 to US$2,300/oz (adjusted for inflation, Figure 4.8), thus encouraging artisanal gold miners to explore the area in more than 2,000 mining sites. As a result, 30,000 people worked directly or indirectly with gold in this region during the 1980s (Bezerra *et al.*, 1998). In the following years, the price of gold dropped and, to compensate, miners had to intensify gold production, increasing water siltation in the Crepori and Tocantins rivers (Figure 4.8).

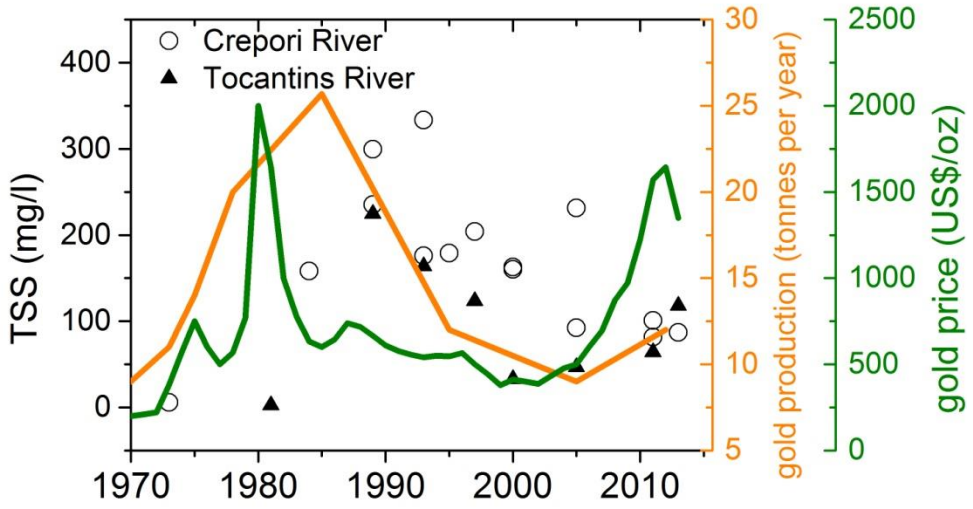

Figure 4.8: Plot of the TSS concentration at the Crepori and Tocantins rivers, gold production in tonnes/year (Silva, 2012) in the Tapajos Area, and gold price (US$/oz) adjusted for inflation from 1970 to 2013. Source: (DNPM, 2013).

The price of gold stabilized during the 1990s, and in an association with surface gold exploitation, a decrease in mining activity was observed. Due to gold price increases in the last 3 years, a new gold rush is taking place (Silva, 2012). At this time, however, a more mechanical and industrial mining approach is extracting gold in deeper layers than artisanal gold mining can reach. Gold production in the 2010s is not as high as in the 1980s, but a significant increase in TSS concentration is observed (Tocantins and Novo rivers), suggesting that even mechanical and industrial mining discharges high amounts of sediment into the rivers.

4.7 Conclusions

The availability of relatively high spatial resolution multispectral satellite imagery since the 1970s is a unique resource to enhance our capability for understanding the spatial and temporal changes in inland water bodies caused by natural and anthropogenic forces. However, the use of time series satellite imagery to derive quantitative variables from the aquatic environment requires atmospheric correction and radiometric normalization of the imagery database. This study provides an analysis of a time series (1970s to present) of satellite imagery acquired with the Landsat satellites for the purpose of evaluating the spatial temporal changes in sediment load from artisanal gold mining activities in the Tapajós River Basin, Amazon. An image processing method based on available models that corrects atmospheric effects, and, based on empirical relationship, estimates TSS concentration from historical Landsat data including MSS (1973-1981), TM (1984-2011), and OLI (2013) data was presented. This imagery analysis allowed some important conclusions and recommendations.

First, it was shown that the 6S model provide statistically significant results when compared to measured $\rho_{\text{surf}}(\lambda)$ from water bodies. The input AOT and water vapor were optimized based on ranges provided by AERONET, which is shown to be a reliable source of atmospheric information for the Amazon. In addition, it was demonstrated that subtracting $\rho_{\text{surf}}(SWIR)$ from $\rho_{\text{surf}}(VNIR)$ improves correlations between *in situ* and satellite $\rho_{\text{surf}}(VNIR)$ by taking into account the effects of sun-glint and possible heterogeneous distribution of aerosol and gases within the scene. Errors observed in the blue band are likely due to aerosol scattering and gases (e.g. NO_2) absorption not fully simulated by the 6S model. Also, adjacency effects of surrounding vegetation can explain

the overestimated satellite $\rho_{surf}(NIR)$. To minimize these effects, we suggest the use of models that take into account adjacency effects and allow better simulation of the gases effects.

For the atmospheric correction on historical Landsat imagery, we have shown that the use of dense forest spectra as reference to optimize atmospheric parameters for 6S is a sound alternative in areas with no information for atmospheric correction models. Similarly, by matching dense forest spectra as an alternative to the absence of 6S code, MSS and OLI surface reflectance imagery were incorporated in the analysis. This study demonstrates significant seasonality effects on forest spectra that must be taken into account for studies on temporal series in the Amazon, especially if using forest spectra as reference for image inter-calibration or histogram matching.

Second, a robust empirical model between *in situ* TSS and concurrent satellite $\rho_{surf}(red)$ was established. The regression estimates TSS with high confidence from $\rho_{surf}(red)$ up to 25%. Above this value the uncertainty increases, suggesting further investigation on other methods to estimate TSS, such as bio-optical models. The combination of the atmospheric correction and the robust reflectance-based TSS model allowed the estimates of TSS independent of date of imagery acquisition.

Third, in regards to environmental changes, this study shows that the majority of the sediment load in the Tapajós River Basin is derived from mining activities, which results in an increase of high light scattering TSS of a silt/clay nature. Further, a seasonal variation of water siltation is observed throughout the time frame of this study (1973-2013). During high water levels, TSS concentrations are consistently lower than those from the low water period. The combination of high dilution and low mining activity

explains lower TSS observed. During low water level periods, mining activities intensifies and thus combined with low volume of water, the TSS increases. In a decadal analysis, a peak of sediment concentration coincides with a peak of gold production in all sites analyzed motivated by high gold prices during the early 1990s. More recently, due to the current gold rush, a TSS increase has been observed mainly in the Novo and Tocantins rivers where industrial mining has been installed.

The $\rho_{\mathrm{surf}}(VNIR)$ and TSS time series established in this paper provide valuable information about water quality changes over time and space in the Tapajós River Basin. Now, for this region, there is a quantified baseline of TSS, which represents the conditions in the 1970s before gold mining activities intensified to the current status. This article reports the seasonal and decadal variation of TSS in the most important tributaries, and indicates current hot spots of mining activity in the region.

The product derived from this paper can support further investigation on how the sediment plume affects, for example, the depth/size of the euphotic zone available for primary production or further investigation on sediment transportation and precipitation process along the Tapajós River. Furthermore, as part of a multi-institute research project, the results will provide information for water quality monitoring and mining regulatory purposes. Lastly, the results show that current high-tech mining techniques cause similar water siltation impacts as artisanal gold mining. Therefore, it is important to adopt mining techniques that minimize the amount of TSS in the water if gold mining is to provide livelihoods for thousands of people in the Amazon.

Chapter 5 - Spatial analysis of Artisanal Small-scale Gold Mining over the past 40-years and relationships with water siltation in the Tapajós River Basin (Brazil)[3]

[3] To be submitted to *Journal of Environmental Management*

5.1 Abstract

This research contributes to a comprehensive evaluation of the impacts of Artisanal and Small-scale Gold Mining (ASGM) activities on the water quality of the Tapajós River Basin by evaluating the mining expansion over the past 40 years and the source of mining tailings. First, the spatial distribution of ASGM was quantified based on satellite images in 2012 (261.7 km2), 2001 (171.7 km2), 1993 (166.3 km2), 1984 (47.5 km2), and 1973 (15.4 km2), distributed mainly over three sub-basins: Crepori, Novo, and Tocantins. Second, analysis of ASGM areas and water quality revealed that Total Suspended Solids (TSS) increased with ASGM expansion. This association, however, also depends on several other factors regarding ASGM activities, such as the applied mining technique, type of exploited gold deposits, and intensity of gold mining. Overall, four main periods of ASGM in the Tapajós region were identified: i) 1958 to 1977, characterized by the first mining activities and low water impacts; ii) 1978 to 1993, characterized by the introduction of low-budget mechanization associated with very high gold prices, resulting in a substantial increase in mining areas and water siltation; iii) 1994 to 2003, characterized by a general recession of ASGM activities due to a reduction of gold prices and exhaustion of secondary, easy-access gold deposits, resulting in decreased TSS concentrations; iv) 2004 to present, characterized by intensification of ASGM encouraged by high gold prices, resulting in an increase of TSS. The current gold rush raises awareness for implementing better mining techniques to achieve water quality control in the present and near future.

5.2 Introduction

Artisanal small-scale gold mining (ASGM) refers to the mining practised using rudimentary technology by individuals, groups, or communities, usually in developing countries of South America, Asia, and Africa (Veiga, 1997; Sousa and Veiga, 2009; Telmer and Stapper, 2007). In the Amazon, substantial ASGM activities started in the 1950s at a few sites, called 'garimpos.' The mining activities increased during the 1970s due to a combination of efficient, low-budget technique and a rise in the gold price (adjusted to inflation) to US$2100/oz in 1980 (Araújo Neto, 2009). The gold mining activities, however, decreased during the late 1990s and early 2000s due to a reduction in the gold price (US$430/oz). Currently, hundreds of thousands of people are directly involved in ASGM in the Amazon Basin because of the relatively high gold price (US$1100/oz) (Sousa and Veiga, 2009; Silva, 2012; Fernandes *et al.*, 2014). In Brazil only, ASGM gold production is responsible for 30 tonnes per year, of which approximately 26% is produced in the Tapajós River Basin by approximately 50,000 miners distributed in more than 300 mining sites (CPRM, 2009; Araújo Neto, 2009; Silva, 2012; Fernandes *et al.*, 2014).

Despite its contribution to the local economy, ASGM causes several environmental impacts, such as mercury contamination, water siltation, and landscape degradation (Rodrigues *et al.*, 1994; Roulet *et al.*, 2001; Sousa and Veiga, 2009). In terms of mercury use, for every ounce of gold produced, two ounces of mercury is used in the grinding and amalgamation process, and is mostly released into the environment (Telmer and Veiga, 2009). The released mercury has been shown to impact the food web, as well as local community health (Coelho-Souza *et al.*, 2011; Rabitto *et al.*, 2011). In addition to

mercury contamination, the ASGM local practice results in high water siltation due to the discharge of sediment from the margins of the rivers, where exploitation of alluvial deposits usually takes place (Nery and Silva, 2002; Silva, 2012). As the miners exploit a particular area of the alluvial plain, new pits are opened, and the mining tailings (water + sediment) are usually discharged back into the river drainage, or to adjacent small ponds/lakes. In those cases, water siltation is caused not only during the mining operations, but also after the mining operation ends as the mining tailings left behind can be transported into the rivers and increase water siltation (Sousa and Veiga, 2009). The discharge of sediment into the water has severe impacts on the water quality, such as decreasing light availability for primary production (Roland and Esteves, 1998; Guenther and Bozelli, 2004; Davies-Colley *et al.*, 1992), and changing benthic (Tudesque *et al.*, 2012) and fish communities (Mol and Ouboter, 2004).

Despite the environmental impacts caused by ASGM, quantification of mining-related areas in the Amazon has yet to be achieved (Telmer *et al.*, 2006; Sousa and Veiga, 2009; Telmer and Veiga, 2009). Mapping historical mining areas using satellite images is of great interest to local managers, since several *garimpos* are informally operating inside protected areas and indigenous lands, causing social conflicts. Moreover, knowing the distribution of the gold mining areas allows us to associate this information with water siltation/water quality data such as total suspended solids (TSS) concentration, as ASGM distribution is highly linked to the river network (Câmara and Corey, 1992; Rodrigues *et al.*, 1994; Fernandes *et al.*, 2014).

Therefore, as part of a comprehensive evaluation of the impacts of ASGM on water quality in the Tapajós River Basin, the objectives of this paper are: 1) quantify the mining

area (km^2) along four main sub-basins − the Jamanxim, Crepori, Tocantinzinho, and Novo river basins − within five time frames based on cloud-free satellite images (1973, 1984, 1993, 2001, and 2012); and 2) investigate whether historical mining area extension is associated with historical water siltation data for the four tributaries. To address these objectives, a spatial map of mining areas based on satellite imagery acquired in 2012; map validation was conducted with 2012 aerial photos (ICMBio, personal communication) were produced. Second, the validated map was then used as a reference to generate the chronological maps based on the classification of Landsat historical images, starting from 2001 followed by 1993, 1984, and 1973. Next, the temporal maps were intersected with secondary information such as soil type and river network buffer, aiming to understand sediment transport from terrestrial sources to aquatic systems. Finally, possible relationships between mining areas, sediment transport, and water siltation based on satellite-based historical TSS from Lobo *et al.* (2015) were investigated.

5.3 Methods

The methods consist of three steps: 1) First, the small-scale gold mining area in 2012 over four sub-basins were mapped, followed by a validation of this classification with aerial photos, and subsequently historical maps of mining area distribution using historical Landsat images (2001, 1993, 1984 and 1973) were generated; 2) Second, historical maps were intersected with the river network, elevation, soil type, and geology thematic maps to assess the possible sources of the sediment discharged into the rivers as

ASGM occurs; 3) Third, the influence of the historical mining area on the historical water siltation, based on TSS data from Lobo *et al.* (2015) was investigated.

5.3.1 Mapping mining areas

Mapping mining areas in 2012

To map the area of the most current (2012) small-scale gold mining in the four sub-basins (Crepori, Novo, Tocantins, and Jamanxim), the *Terraclass* maps (*http://www.inpe.br/cra*) were used as an initial spatial guideline for identification of mining areas. The *Terraclass* maps provide the total deforested area in 2010 for the whole Brazilian Amazon (PRODES database, (INPE, 2011)), with several land cover classes, such as mining, pasture fields, and secondary forest. Although the *Terraclass-2010* indicates the main mining areas, it lacks in identifying small mining polygons (<20 ha). Nonetheless, it was used as a base map for guiding the manual classification of the satellite image LISS-III acquired on September 16th, 2012. The generated map, *MapASGM-2012,* and the *TerraClass-2010* map were validated with aerial-photographs taken in 2012 considering 70 validating polygons corresponding to mining and deforested areas (Table 5.1 and 5.2). The classification of ASGM includes all land use related to mining operations, such as mining areas themselves, airstrips, degraded areas, mining-related ponds, and mining settlements, as indicated in Figure 5.1.

According to the validation matrix (Table 5.1), the *TerraClass-2010* clearly underestimated the mining area. *TerraClass-2010* did not classify mining in 20 out of 53 polygons that are identified as ASGM on the photos, with omission errors totalling 51%.

The validation of the *MapAGSM-2012* classification showed that the overall accuracy increased to 93%, since manual editing included mining areas of different sizes from very small (5 ha) to large (1,000 ha). Omission errors total 6% (3/53), whereas commission errors are less than 4% (Table 5.2). Along with users' expertise in visual identification of mining areas in the LISS-III image, the mapping process used auxiliary information such as '*garimpos'* distribution, roads, and other secondary information for a more accurate classification (example in Figure 5.1).

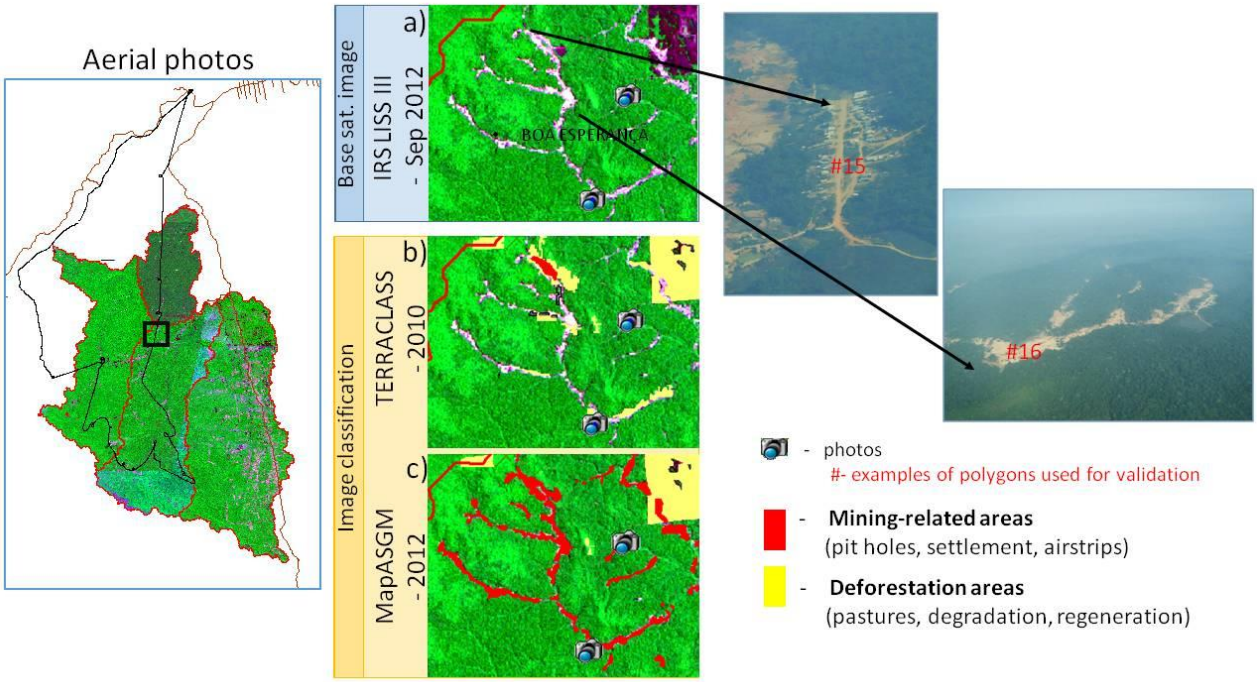

Figure 5.1: Example of land-cover classification for *Terraclass-2010* (b) and *MapAGSM-2012* (c). The latter is based on LISS-III image (a). The aerial-photos track is indicated on the left along with the location of the example.

Table 5.1: Matrix of validation of *Terraclass-2010* land use classification taking aerial photos as ground-truth. Overall accuracy is 55%.

		Classification - *Terraclass 2010*				
		Mining	Deforestation	Others	Not classified	Total
photos	Mining	26	5	2	20	53
	Deforestation	2	10		2	14
	Others			3		3
	Total	28	15	5	22	70

Table 5.2: Matrix of validation of *MapAGSM-2012* land use classification taking aerial photos as ground-truth. Overall accuracy is 93%.

		Classification – *MapASGM-2012*				
		Mining	Deforestation	Others	Not classified	Total
photos	Mining	50			3	53
	Deforestation	2	12			14
	Others			3		3
	Total	52	12	3	3	70

Mapping mining areas in 2001, 1993, 1984, and 1973

After mapping and validating ASGM areas in the Tapajós River in 2012, the MapASGM-2012 was used as a reference map for classification of mining areas in 2001. Landsat-TM (2001) images were downloaded from the INPE website (dgi.inpe.br), geometrically corrected, and classified into one class (mask) that includes all deforested areas, such as pasture, mining, and roads. In order to map mining areas exclusively, this new mask (2001) was intersected with the MapASGM-2012. Next, a precise manual editing of mining areas was performed to incorporate mining areas that were not included in the intersection with 2012, thus resulting in the MapASGM-2001 (Figure 5.2). This

process was repeated for the remaining years (1993, 1984, and 1973) for the sub-basins of study: Crepori, Novo, Tocantins, and Jamanxim.

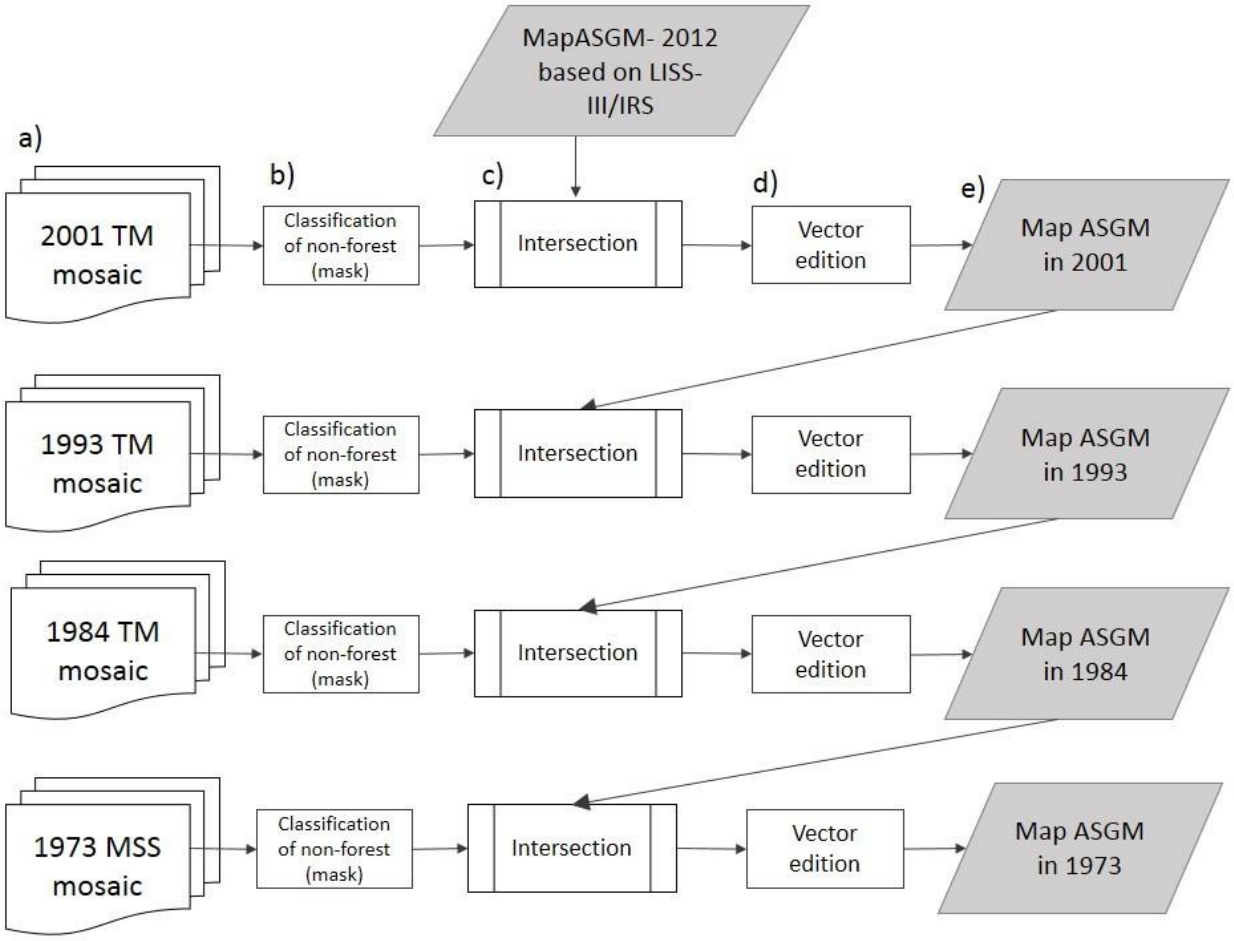

Figure 5.2: Flowchart of the procedure taken for mapping historical mining settlements using Landsat historical images (2001, 1993, 1984, and 1973). Satellite image database in 2001 (a) was submitted to a classification where all land cover classes, except forest, are included into one class, creating a vector data called mask (b). This mask was then intersected with the *MapASGM-2012* (c) followed by a vector edition in order to include all mining areas in 2001 (d), resulting in the *MapASGM-2001* (e). The same procedure was applied to the imagery Landsat-TM database in 1993, 1984, and Landsat-MSS data in 1973. See imagery database information in Lobo *et al.* (2015).

5.3.2 Investigating the source of the sediment derived from ASGM

To assess the source of the sediment where mining was taking place, the gold mining areas (3.1) were tabulated with thematic maps of particular interest for sediment transport such as soil type (SiBCS, 2006), geology (CPRM, 2009), and digital elevation model (INPE, 2008) (Figure 5.3). Further, buffer ring-zones (100; 250; 500; 1,000m) along the river network (ANA, 2013) (Figure 5.3) were created to define proximity of mining area to the river network. According to the recent New Forest Code (National Law nº12.651/2012), a buffer distance of at least 100 m from rivers with a width between 50 and 200 m are permanently protected by law and no kind of land use is allowed because it directly affects water quality. Similarly, buffer ring-zones were created along roads (MMA, 2010) in order to investigate their relevance to water siltation.

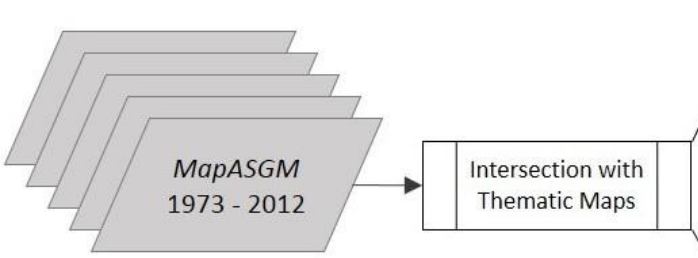

Thematic map	Scale	Source
Soil Type	1:250,000	SiBCS, 2006
Geology	1:250,000	CPRM, 2009
Elevation	-	INPE, 2008
River Network Buffer	1:250,000	ANA, 2013
Roads buffer	1:250,000	MMA, 2010

Figure 5.3: The historical *MapASGM* database (1973-1984-1993-2001-2012) was intersected with thematic maps including: soil type, geology units, elevation, river network buffer, and roads buffer. Scale of production (metadata) and source of thematic maps are shown. Elevation map based on SRTM images with pixel resolution of 90 m.

5.3.3 Relation between historical mining areas and water siltation

Since neither historical nor present data on sediment transportation of mining tailings discharged into the river network is available, the historical mapped mining areas were spatially associated with corresponding satellite-based water siltation from Lobo *et al.* (2015) for the tributaries, Jamanxim, Crepori, Novo, and the Tocantins. The water siltation data corresponds to the low water level period, as that is the time of year when mining activities are more intense (Lobo *et al.*, 2015). The TSS historical data was defined based on satellite images at the mouth of each tributary. These subsets were corrected for atmospheric and sun-glint effects, and used to retrieve TSS values ($mg.L^{-1}$) based on an empirical equation ($r^2=0.94$; $p<0.05$; $n=39$) detailed in Lobo *et al.* (2015). Further investigation of spatial and temporal effects of ASGM on water siltation were conducted based on the land-cover dynamic, general mining techniques, and socio-economic framework throughout the decades.

5.4 Results

5.4.1 Gold mining area from 1973 to 2012

The quantification of the mining area in the four sub-basins of study during the past 40 years – 1973, 1984, 1993, 2001, and 2012 – are presented in Figure 5.4 and Table 5.3. In 1973, land cover pristine conditions were observed with a mining area of 15.4 km^2 (0.03% of the total area of study), mainly limited to Crepori (6.3 km^2) and Novo (7.0 km^2) sub-basins. Eleven years later, the mining area increased to 47.5 km^2 (0.09% of the total area), and again the Crepori and the Novo sub-basins showed the largest mining areas with 22.8 and 16.1 km^2, respectively. In 1993, the mining area tripled to 166.3 km^2 (0.30% of the total area), with the Crepori sub-basin alone showing 77.0 km^2, followed by the Novo (69.2), the Tocantins (11.9), and the Jamanxim (8.2 km^2). Contrary to the trend in previous years, in the next decade (to 2001), the total mining area increased only slightly to 171.7 km^2 (0.31% of the total area). Interestingly, a reduction in mining area was observed in the Novo sub-basin. The stagnation period during the late 1990s and early 2000s rapidly changed within the following 11 years, resulting in an increase in the mining area to 261.7 km^2 (0.48% of the total area) in 2012. It is interesting to point out that the Jamanxim sub-basin, while presenting the lowest mining area, had the greatest deforestation rates throughout the five decade period (20% of the total area in 2012), mostly along the BR-163 (South-North) highway.

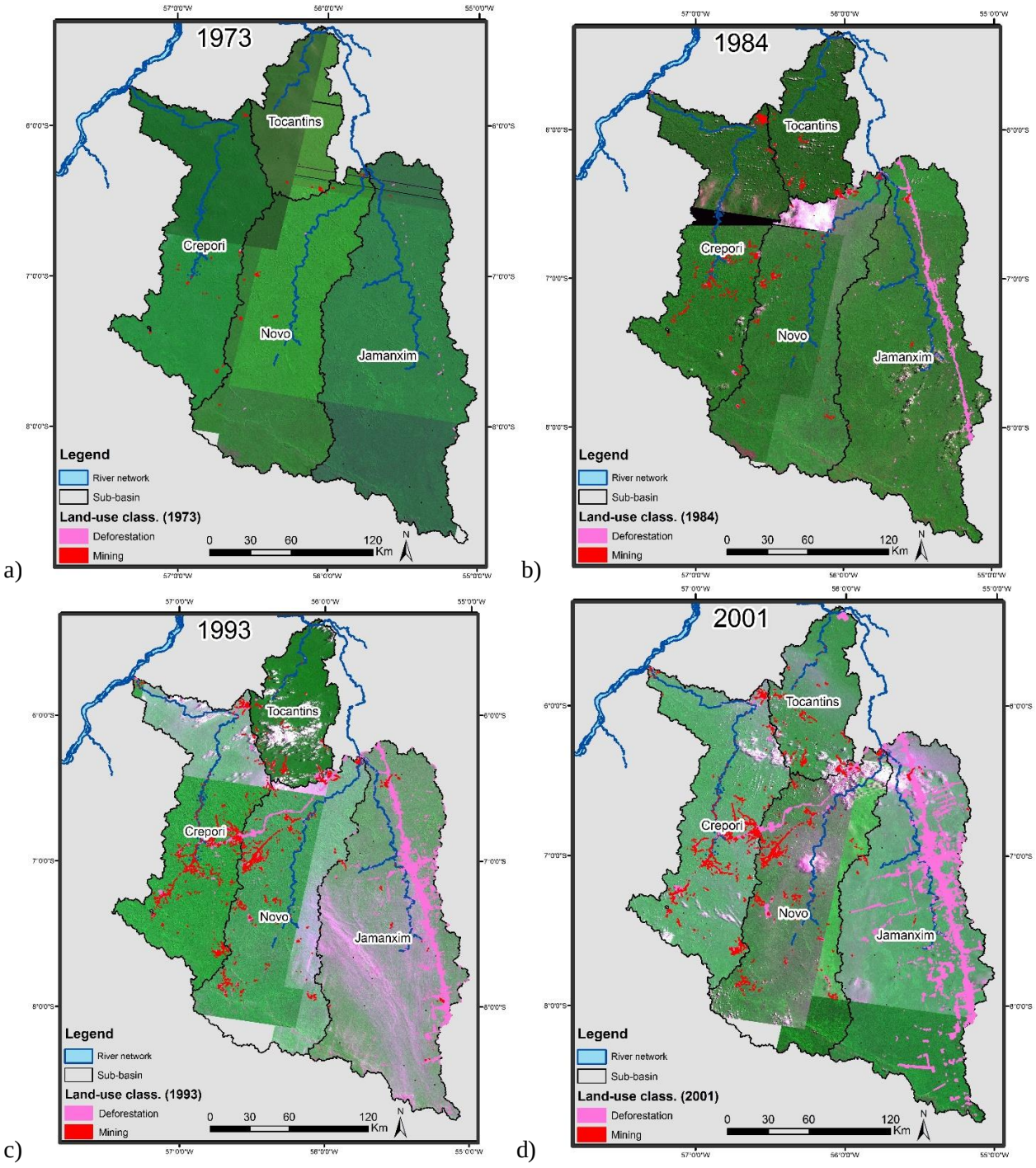
a)
1973
Tocantins
Crepori
Novo
Jamanxim
Legend
River network
Sub-basin
Land-use class. (1973)
Deforestation
Mining
0 30 60 120 Km
N
b)
1984
Tocantins
Crepori
Novo
Jamanxim
Legend
River network
Sub-basin
Land-use class. (1984)
Deforestation
Mining
0 30 60 120 Km
N
c)
1993
Tocantins
Crepori
Novo
Jamanxim
Legend
River network
Sub-basin
Land-use class. (1993)
Deforestation
Mining
0 30 60 120 Km
N
d)
2001
Tocantins
Crepori
Novo
Jamanxim
Legend
River network
Sub-basin
Land-use class. (2001)
Deforestation
Mining
0 30 60 120 Km
N

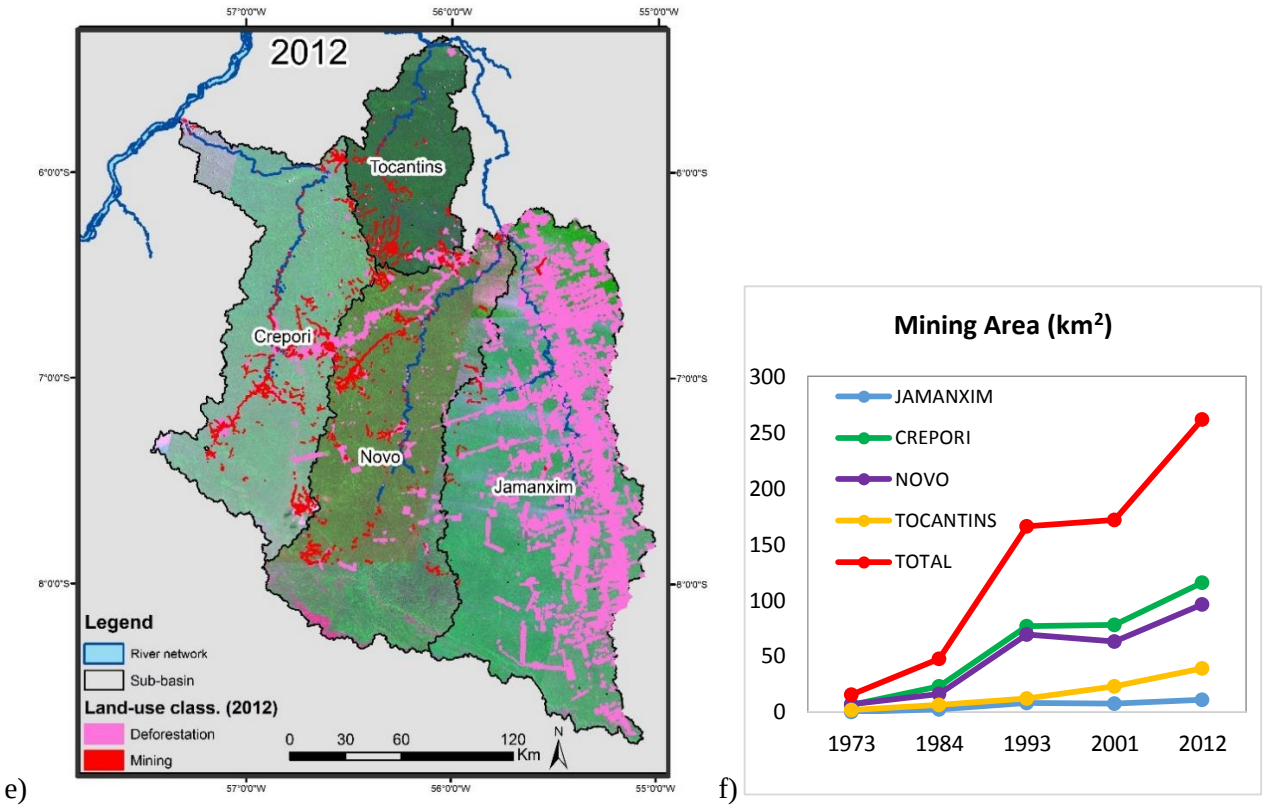

e) f)

Figure 5.4: Mining areas mapped in 1973 (a), 1984 (b), 1993 (c), 2001 (d), amd 2012 (e). All variations of green correspond to forest cover. Tabulated areas are plotted in the graph (f) for the four sub-basins of study: Crepori, Novo, Tocantins, and Jamanxim.

Table 5.3: Tabulation of historical ASGM (a) and deforestation area (b) for the four sub-basins of study: Crepori, Novo, Tocantins and Jamanxim.

a) Mining area (km^2)

	Jamanxim	Crepori	Novo	Tocantins	TOTAL
1973	0.1	6.3	7.0	2.0	15.4
1984	2.2	22.8	16.1	6.3	47.5
1993	8.2	77.0	69.2	11.9	166.3
2001	7.3	77.9	63.1	23.3	171.7
2012	10.9	115.5	96.2	39.1	261.7

b) Deforestation area (km^2)

	Jamanxim	Crepori	Novo	Tocantins	TOTAL
1973	3.8	0.5	0.5	0.0	4.8
1984	185.1	11.7	10.2	2.9	209.9
1993	579.2	52.5	62.8	14.6	709.1
2001	1338.2	69.2	107.3	38.8	1553.5
2012	4212.0	192.2	365.7	54.9	4824.8

5.4.2 Characterization and distribution of gold mining area: proximity to river and road, topography and geology

The quantification of the mining area along the river network buffer zones showed that, in 2012, 40% of total mining areas were within a 500 m distance from the river network (Figure 5.5). Moreover, within the first 100 m, which is considered fully protected by law (Law nº12.651/12), ~9% of the total mining area was mapped in 2012. Together with the increment of the total mining area over the years (Figure 5.4), the percentage along the river network also increased from 1973 to 2012. As an example, within the first 500 m from the river network, we found 12% of ASGM in 1973, and 31% in 1984. In 1993 and 2001, the percentage was similar to that of 2012 (40%), which indicates that the mining area increment in 2012 followed a pattern of gold exploitation similar to that of the previous two decades (Figure 5.5). Mapped mining areas are not predominantly located along the road network. For instance, approximately 5% of the total mining area in 2012 was mapped within a buffer of 1,000 m along the roads, mostly along the 'Trans-Garimpeira' road (East-West). On the other hand, the area of deforestation is highly associated with the road distribution as shown in the Jamanxim basin (Figure 5.5) with deforestation areas along the BR-163 (North-South).

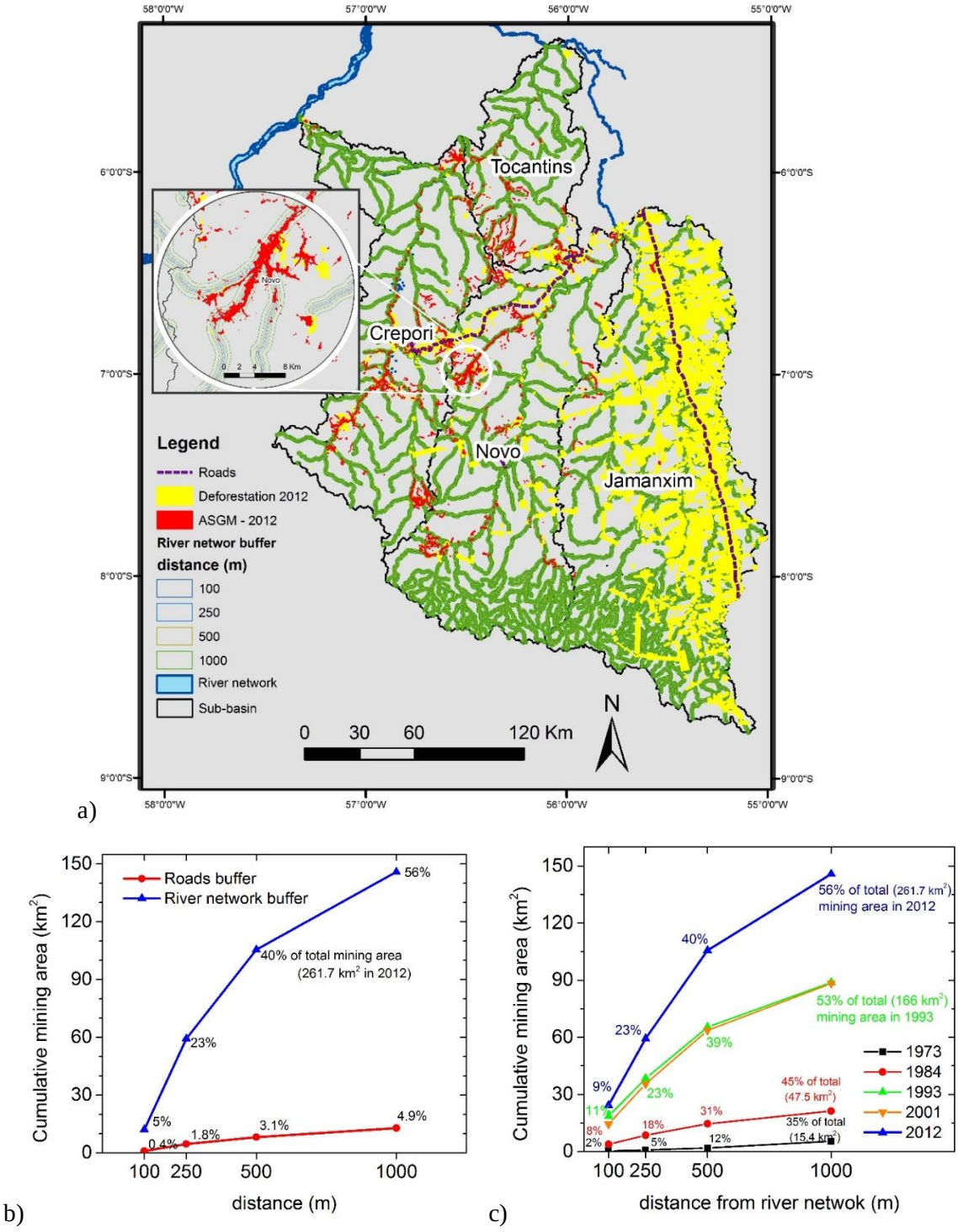

Figure 5.5: Quantification of mining area along river network buffer (ANA, 2013) for 100, 250, 500, and 1,000 m. a (millions years). Map of mining and deforestation area for 2012 along river and road buffer zones. b) Cumulative mining area with increasing distance from rivers and roads. c) Decadal cumulative mining area with increasing distance from river network.

Figure 5.6 shows that the locations of the mining areas are predominantly in lower altitudes of the sub-basin. Note that in the Crepori basin there are two main areas of high gold production, one located in the lower altitude, named Cuiú-Cuiú Gold Mining, and the other at higher altitude, named Creporizão (Figure 5.6 and Appendix A, for details). From the analysis, it is clear that until 1984 most of the mining was located in the lower altitudes of all the sub-basins. However, in the following decades, not only the mining areas increased, but also new mining areas were settled at higher altitudes, as observed at Novo and, mainly, at Crepori Basin (Figure 5.6).

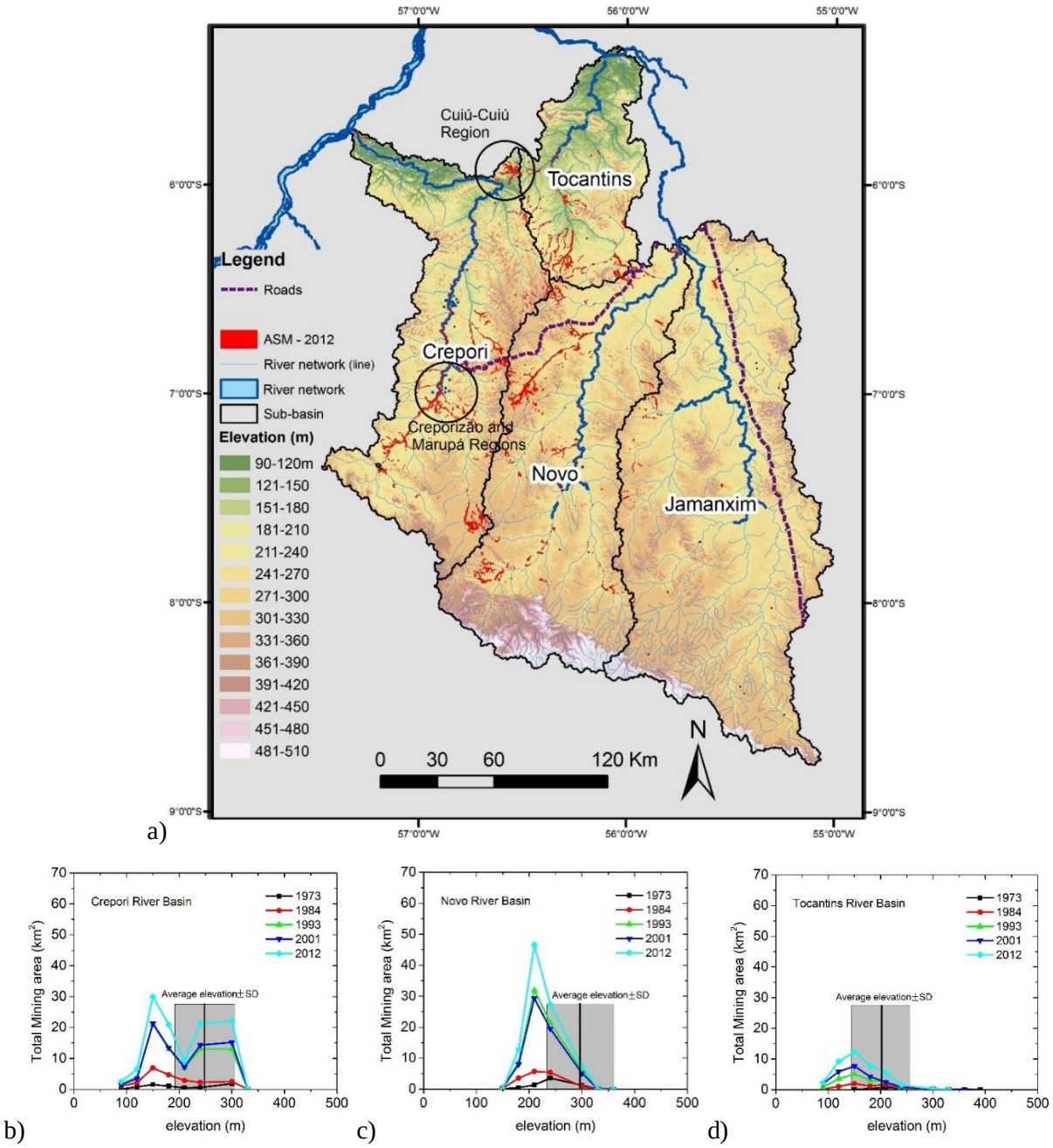

Figure 5.6: ASGM in 2012 plotted over elevation map (a). Tabulation of ASGM for three sub-basins: the Crepori (b), Novo (c), and Tocantins (d) from 1973 to 2012 shows that most mining took place on the lower section of the sub-basins. Average and standard deviation elevation for each sub-basin is indicated. Two peaks of mining area in the Crepori with increasing elevation correspond to Cuiú-Cuiú Region and Creporizçao Region, respectively. Interesting to point out that in 1993 ASGM started mining at higher elevations, as shown at the Crepori sub-basin.

The distribution of gold mining over the soil type map (SiBCS, 2006) shows that mining predominantly occurs in latosol soils (Figure 5.7). Different types of latosol were identified, varying from yellow, red, to brownish in colour, depending on the amount of ferric oxides (SiBCS, 2006). Overall, all latosols are characterized with high clay content (up to 70% of total weight), and the disposal of these soils into the drainage often occurs with the use of the water-jet technique. Another highly mined area in gleysol soils, which relates to alluvial systems. Gleysols are generally also clay-rich, but with higher water content as they are subject to flooding several months a year. This type of soil can be transported into the rivers mainly with the use of raft or dredge techniques.

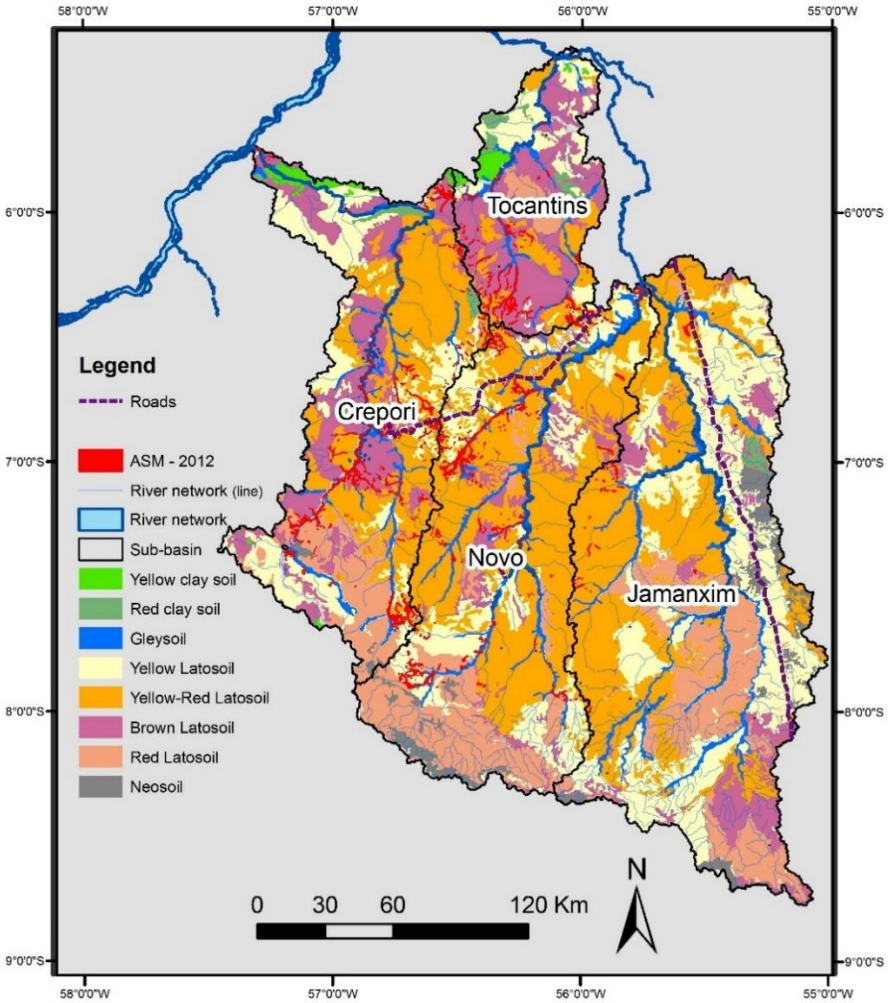

Soil Type (SiBCS, 2006)	Soil Type (World Reference Base, 1998)	Mining in 2012 (km^2)
Yellow Claysol	Acrisol	0.7
Red Claysol	Acrisol	0.5
Gleysol	Gleysol	53.7
Yellow Latosol	Ferrasol	56.1
Yellow/red Latosol	Ferrasol	69.0
Brown Latosol	Ferrasol	46.6
Red Latosol	Ferrasol	8.8
Neosol	Arenosol	2.6

Figure 5.7: Tabulated mining area in 2012 over different soil types according to Brazilian System for Soil Classification (SiBCS, 2006) and the international classification (WRB/FAO, 1998).

While secondary deposits of gold are mainly exploited with water-jet or draft techniques, the mineralized primary gold often requires some degree of mechanization for ore extraction and processing (Silva, 2012). Normally, the primary deposits of gold occuring above the fresh rock, approximately 15 to 120 m thick, are mined by open pit, and processed with the use of pit-loaders and hammer mills (Santos *et al.*, 2001). Deposits of primary gold within the granitoid Tapajós-Parauari orogenic belt are highly related to discrete magmatic arc formations, such as Cuiú-Cuiú, Creporizão, and Parauari, formed between 2,010 and 1,880 Ma. Geological surveys indicated that gold deposits associated with quartz-veins in these formations often occur in two types: orogenic deposition (Cuiú-Cuiú), and intrusions-centred (Creporizão and Parauari formations) (Santos *et al.*, 2001). Several other geological formations are described within the Tapajós Region. Nonetheless, the presence of quartz-veins occur with less intensity or do not occur at all. Thus, the probability of gold deposits in those formations is lower than the formations characterized by magmatic arcs. Not coincidently, the association between geological formation and mined areas indicated that the mining areas are distributed over

three main geological formations with magmatic arcs: Parauari (total mining area of 100.5 km^2), Creporizão (92.8 km^2), and the Cuiú-Cuiú (48.7 km^2) (Figure 5.8).

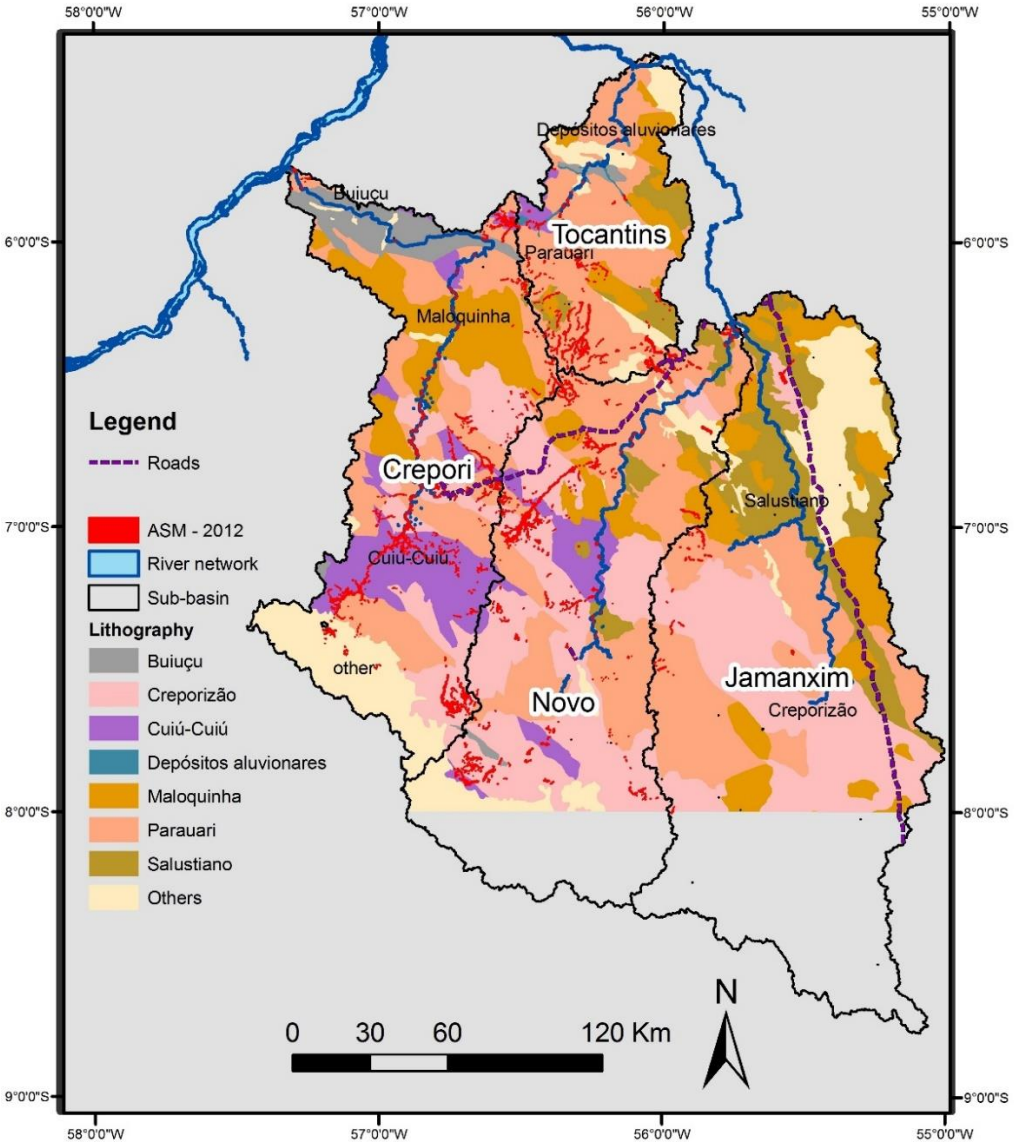

Geology	Crepori	Tocantins	Novo	Jamanxim	Total (km^2)
Parauari	31.8	32.0	31.3	5.4	100.5
Creporizão	38.8	0.0	49.5	4.3	92.8
Cuiú-cuiú	37.1	0.8	10.7	0.0	48.7
Others	7.4	6.2	4.6	0.9	19.3

Figure 5.8: Distribution of mining area (km^2) in 2012 over different geological formations (CPRM, 2009).

5.4.3 Historical gold mining area and water siltation

The historical gold mining area maps (section 4.1) along with historical TSS concentration from Lobo *et al.* (2015) (Figure 5.9) were combined for investigating the temporal relationship between mining area expansion and water siltation in the four tributaries: Jamanxim, Crepori, Novo, and the Tocantins sub-basins. These four sub-basins are categorized into non-impacted (Jamanxim) and impacted by gold mining (Crepori, Novo, and the Tocantins). Although mining does occur in the Jamanxim River sub-basin, it is relatively minor compared to the other basins, and even with a high deforestation rate, TSS remains under 5 mg/L (Figure 5.9d). These TSS values are similar to those from upstream Tapajós River (Figure 5.9e), where ASGM also occurs with less intensity (Santos *et al.*, 2001), and can be used as a baseline for comparison among the sub-basins.

For the impacted sub-basins, Figure 5.9 (a-c) shows an association of TSS ($mg.L^{-1}$) with increasing area of ASGM (km^2). The consequences to water optical properties of the historical expansion of gold mining area are notorious for the Crepori and the Novo rivers. In these rivers, the ASGM started with a few mining locations in 1973, with no resultant perceived impact on water turbidity; TSS concentrations were <5.0 mg/L, similar to upstream Tapajós (Jacareacanga, Figure 5.9e). However, in the following decade mining activities (represented by the mining area) increased by about three and two times for the Crepori and Novo rivers, respectively, and thus resulted in increased TSS concentration (>50 mg/L for Crepori, and >15 mg/L for Novo) (Figure 5.9a and b). In the subsequent decade, the Crepori and the Novo rivers exhibited a similar trend; TSS

concentration were above 100 mg/L, while mining area increased from around 20.0 km^2 to 75.0 km^2 in both sub-basins. In the Tocantins sub-basin, the increase in mining area was less abrupt than in the Crepori and Novo sub-basins until the late 1980s. However, in 1989 the TSS concentration increased to concentrations as high as 220.0 mg/L, indicating significant mining activities in the Tocantins sub-basin during this period (Figure 5.9, also see Figure 5.10 and 5.11 for TSS maps).

The period between 1993 and 2001 is characterized by a recession in ASGM activities (according to Rodrigues *et al.*, 1994), and consequently low mining area expansion in the sub-basins. For all impacted sub-basins, a tendency of TSS reduction was observed during this period of ASGM recession. However, the recent gold rush that has been occurring for the past 7 years (represented by the increment of gold mining area from 2001 to 2012) has influenced TSS concentrations. The Novo and the Tocantins rivers showed increasing TSS concentrations (mg/L) in this period (Figure 5.9 and 5.11). This tendency was not observed for the Crepori, but this tributary still presented high TSS concentrations (around 100 mg/L) throughout the past decade (see Figure 5.9 and 5.10).

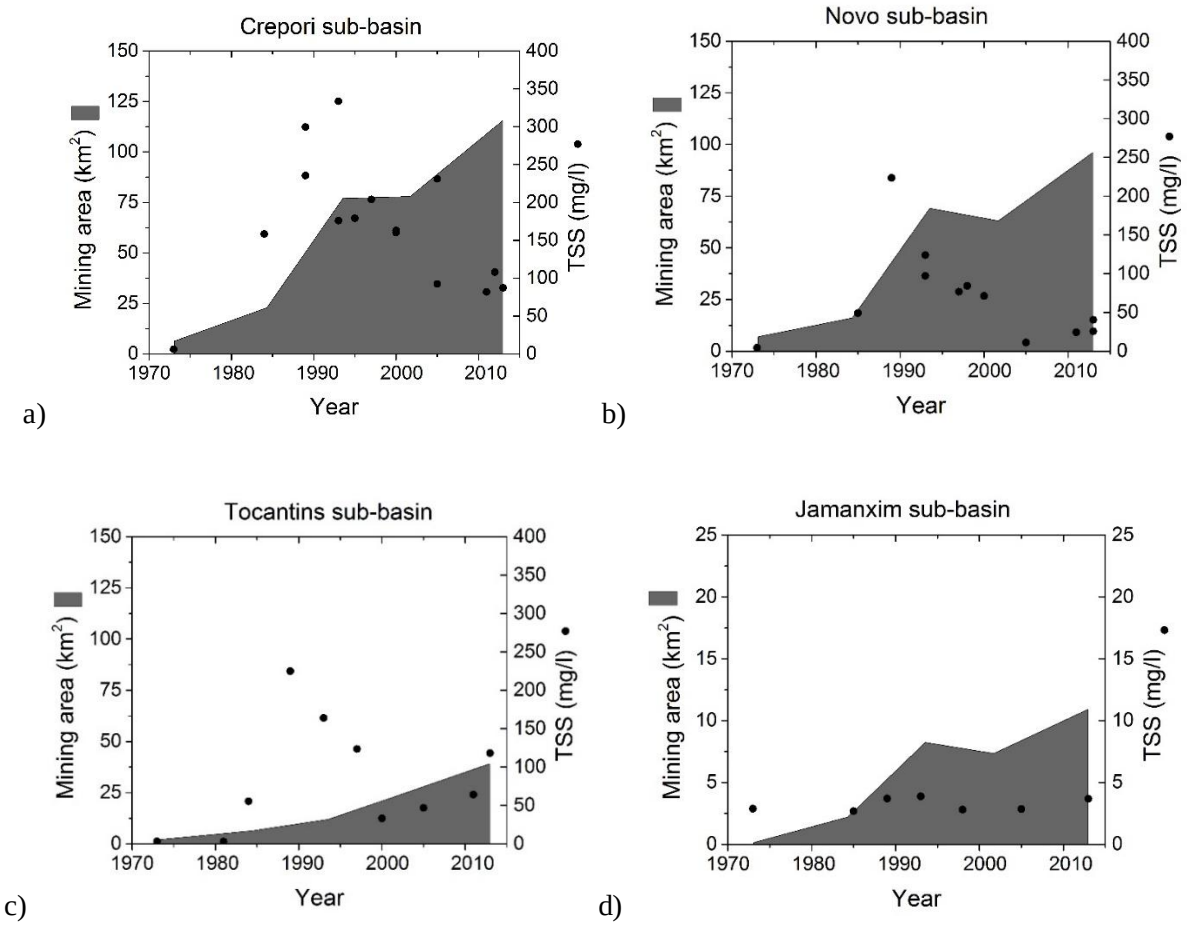

Figure 5.9: Historical TSS at the four rivers plotted along mining areas at respective sub-basins (a-d). Note different TSS scale for the Jamanxim River Basin. (e) Shows the upper Tapajós River as a general baseline for TSS concentration.

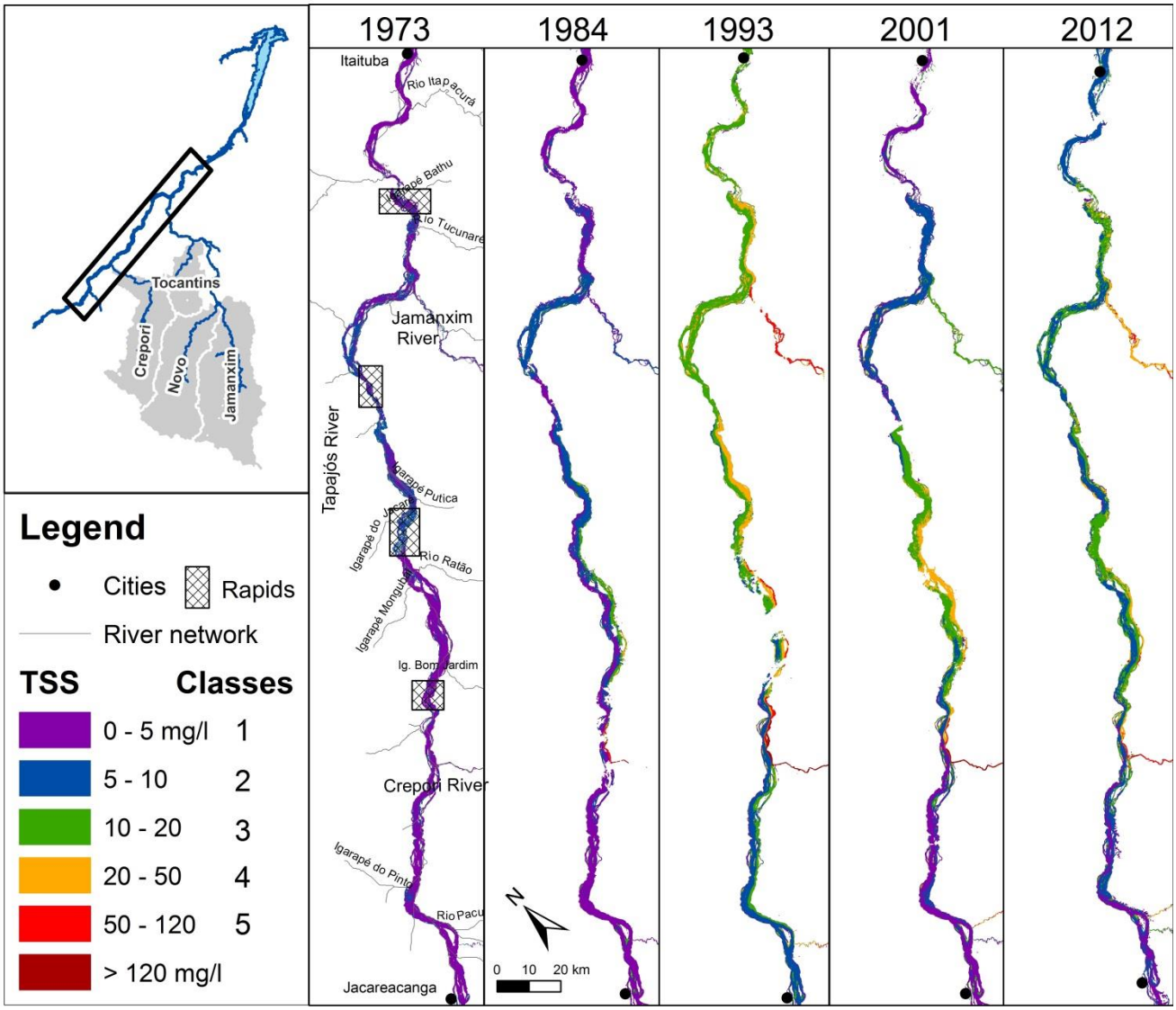

Figure 5.10: Spatial and temporal distribution of TSS along the Tapajós River Basin (between Jacareacanga and Itaituba cities) and main tributaries: Crepori and Jamanxim River. Sections of the river with rapids that often cause water mixing are also indicated. TSS maps based on five mosaics of satellite images: 1973 (Landsat-MSS), 1984, 1993, 2001(Landsat-TM), and 2012 (IRS/LISS-III). All images from the dry season (August to October).

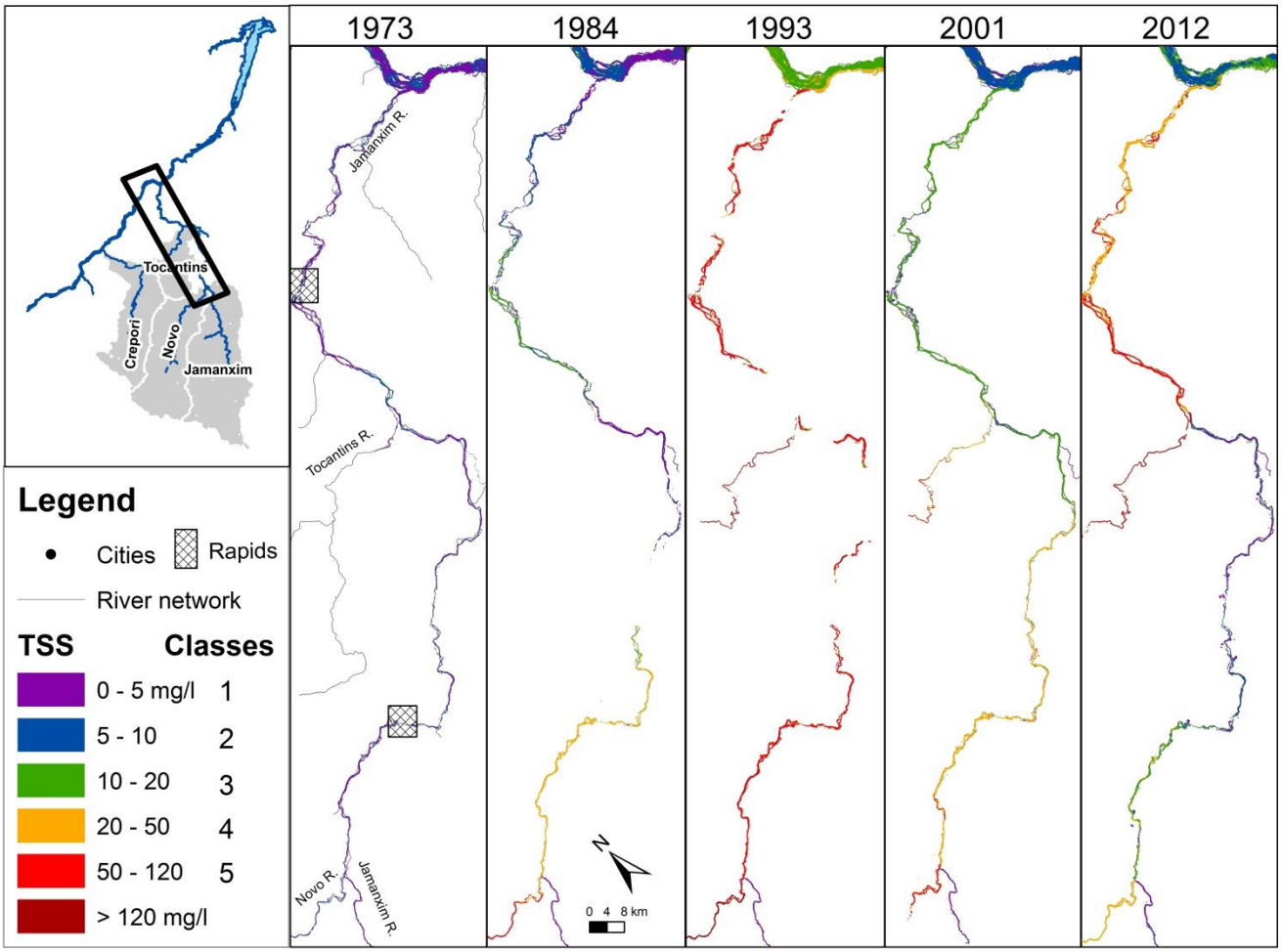

Figure 5.11: Spatial and temporal distribution of TSS along the Jamanxim River Basin and main tributaries: Novo and Tocantins River. Sections of the river with rapids that often cause water mixing are also indicated. TSS maps based on five mosaics of satellite images: 1973 (Landsat-MSS), 1984, 1993, 2001(Landsat-TM), and 2012 (IRS/LISS-III). All images from the dry season (August to October).

5.5 Discussion

The spatial temporal extent of ASGM and its relationship with river water siltation is discussed in a chronological order considering the history of gold exploitation and the physical processes of sediment transportation (mining methods, geology, and topography) that affect water siltation of the Tapajós River system. Combining the historical context of mining activities (Câmara and Corey, 1992; Rodrigues *et al.*, 1994; Fernandes *et al.*, 2014) and data from this research, four main periods of ASGM in this region were identified:

(1) Period from 1958 to 1977 – As an alternative to the decline of latex production, the first ASGMs were established around 1958 along the Tropas and the Crepori rivers (Bezerra *et al.*, 1998). Following the National Integrative Program, the next decade experienced the construction of several highways crossing the Brazilian Amazon, such as Cuiabá-Santarém Highway (BR-163) (see Figure 2.1 for location). These investments encouraged a significant migration from the north-east region of Brazil to the Tapajós River basin to start new mining pits (Rodrigues *et al.*, 1994; Fernandes *et al.*, 2014). As a result, in the early 1970s the estimated area of ASGM was approximately 15.4 km^2 (Figure 5.4), which correlates with the reports in the literature (Rodrigues *et al.*, 1994; Araújo Neto, 2009; Fernandes *et al.*, 2014). Some of the identified mining locations in 1973 became large ‘garimpos’ in the following decades, specifically in the Creporizão area, the Cuiú-Cuiú, and the Marupá within the Crepori sub-basin. The ‘garimpos’ Palito, Patrocínio, and São Domingos were identified in the Novo sub-basin. The ‘garimpo’ Água Branca in the Tocantins sub-basin, and in the Jamanxim sub-basin, the ‘garimpo’ São Jorge was identified based on Landsat/MSS images from 1973.

Until 1977, ASGM exploited mostly the alluvial deposits of secondary gold ore by manual and rudimentary methods, such as pans and picks (Bezerra *et al.*, 1998). In fact, our results indicate that most ASGM occurred at lower sections of the sub-basins, which roughly corresponds to alluvial sections (Figure 5.6). The low capacity of ore processing during this period explains the low water siltation impact observed. TSS concentrations lower than 5 mg/L were estimated for the Crepori River (Figure 5.9a), similar to expected concentrations for 'clear water' according to the Amazonian water classification scheme (Sioli, 1984; Junk, 1997). Estimated TSS data for the remaining tributaries were contaminated by radiance adjacency effect (Lobo *et al.*, 2015) due to MSS image pixel size (80 m). Despite the uncertainty of those estimates, they were similar to those of Crepori and upstream Tapajós River. Those findings indicate that the establishment of ASGM from 1958 to 1973 likely resulted in low water siltation impact.

(2) Period from 1978 to 1993 – The low impact scenario depicted in 1973 was radically changed in the following two decades due to the ASGM booming in the Tapajós Basin. During this period, there was an increase in both the extent of ASGM and sediment concentrations in the rivers (Figure 5.9 to 5.11). 1978 was a turning point in the ASGM, when small machines such as water-jets and drafts/dredges were introduced, aiming to enhance the capacity of ore processing, and consequently increase gold production (Araújo Neto, 2009; Câmara and Corey, 1992; Sousa and Veiga, 2009). Although the use of rafts results in a major impact on water siltation (Figure 2.2) (Telmer *et al.*, 2006), their specific historical impact on TSS concentration in the water cannot be estimated based on historical satellite images. Nonetheless, literature and reports indicate that many rafts operated in the Tapajós River from 1978-1993 (Rodrigues *et al.*, 1994;

Telmer *et al.*, 2006), and likely had a severe impact on water turbidity, as indicated by satellite images acquired in 1989 and 1993 (Figure 5.10 and 5.11).

As a result of this new low-budget technology (water-jets and rafts), and a synergism of factors such as high gold prices and government support (Silva, 2012; Fernandes *et al.*, 2014), the 1984 (47.5 km^2) and 1993 (166.3 km^2) maps showed a spatial expansion of all mining locations compared with the 1973 map (15.4 km^2) (Figure 5.4 and Table 5.3). The period between 1983 and 1993 corresponds to the peak of gold mining production (on average, 20 tonnes a year), when approximately 100,000 'garimpeiros' over more than 500 'garimpos' were reported (Silva, 2012; Fernandes *et al.*, 2014). Most of this ASGM expansion occurred within the river network. In 1993, for example, 55% of the mining areas were located within 1,000 m of the river network (Figure 5.5), mostly on alluvial deposits. It is worth noting that the soil type in the alluvial is mostly gleysol (Figure 5.7), with high amounts of clay (>70%) and inorganic fine particles that remain suspended in the water for many kilometres (Telmer *et al.*, 2006). The other 45% of the mining area is distributed beyond the range of 1,000 m from the river network (Figure 5.5), indicating that colluvial deposits of secondary gold were heavily exploited as well. The increase in exploitation of colluvial deposits found at higher elevations is evident by the increase in the ASGM area at higher elevations from 1984 to 1993 (Figure 5.6). Although not inside the 1,000 m river buffer, these areas can also represent a direct impact to the riverine system, since most of the mining areas connect to the river drainage network. Consequently, direct disposal of mining tailings associated to degraded landscape have a significant influence on increased sediment transport into the river drainage (Sousa and Veiga, 2009).

In the sub-basins where the ASGM area increased, the TSS increased more than one order of magnitude. For example, in the Crepori River, TSS increased from 6.5 mg/L in 1973 to over 200.0 mg/L between 1989 and 1993 (Figure 5.9). The effects of ASGM were also observed for the Novo and the Tocantins rivers, where TSS increased to levels above 100 mg/L during the same period (Figures 5.8 and 5.10). Although the Novo and the Crepori sub-basins have similar areas (~14,000 km^2, see Figure 2.1 and Appendix A), we identified more mining centres at the Crepori sub-basin, such as the Marupá, the Cuiú-Cuiú, the Creporizão, and the Creporizinho areas, when compared to the Novo River with only two major areas, the 'garimpos' Palito, and Patrocínio. The larger number of mining areas indicates higher capacity of ore processing and, consequently, explains the observed higher TSS concentrations. It is worth noting that, in the Jamanxin sub-basin, high deforestation rates were observed, increasing from 1973 (3.8 km^2) to 1993 (579.2 km^2), but impacts on the TSS were not identified, since concentrations were lower than 5.0 mg/L for all years (Figure 5.9). In the Amazon, changes in the land cover from forest to pastureland have resulted in an evident increase in water turbidity only in small streams during/after rain events, when surficial water flow carries higher dissolved and particulate matter (Neill *et al.*, 2006). In the rivers studied by Neill *et al.* (2006), the water siltation due to deforestation/pasture are not at the same magnitude as impacts caused by mining tailings observed in this study. In the case of Tapajós River Basin, the water siltation caused by deforestation can therefore be disregarded when compared to water siltation caused by ASGM.

Overall, a combination of new mining techniques (rafts and water-jets) with exploitation of primary and secondary gold from alluvial and colluvial deposits

contributed to the transport of high sediment loads, mostly clay in nature (Figure 5.7), to the river's drainage system during the boom of ASGM from 1978 to 1993. According to (Bezerra *et al.*, 1998), a total of 67.0 million m^3/year of sediment was removed from the margins of many tributaries of the Tapajós River in the 1980s due to gold mining activities. Most of this sediment was transported to the rivers, as shown by the retrieved TSS in all tributaries (Figure 5.9 to 5.11), except for the Jamanxim sub-basin, where low rates of mining were observed. The ASGM boom was so intense during the period between 1989 and 1993 that even the upstream Tapajós (Jacaraeacanga), used as a TSS baseline, presented an increase in TSS (Figure 5.10) as a result of mining operations in the Teles Pires River Basin (upper Tapajós), reported by Santos *et al.* (2001).

(3) Period from 1994 to 2003 – The high spatial extension of ASGM areas and associated increase in TSS concentrations in the rivers observed in the previous period changed to a more stagnant condition in the following decade (Figure 5.4). From 1990 to 2000, gold production in this region decreased gradually from approximately 20 to 8 tonnes per year due to a reduction in the international gold price in the principal stock markets around the world (Rodrigues *et al.*, 1994). In addition, the exhaustion of easy-access alluvial and colluvial gold deposits forced the miners to start exploiting primary deposits of gold, which require high mechanization levels and an increase in the costs of production (Rodrigues *et al.*, 1994*)*. These factors contributed to the observed minimal change in ASGM area and the decrease in suspended sediment in the riverine waters. Consequently, TSS reduced by half or more in comparison with the previous decade in all impacted rivers (Figure 5.9). Estimated TSS concentrations were still much higher than the initial period (Figure 5.9), and this is likely a result of, although reduced, still

active ASGM, as suggested by Telmer (2013), as well as a result of mining tailings derived from abandoned mining areas (degraded areas). For the Jamanxim River, neither the sparse ASGM nor the very high deforestation rate from 1993 to 2001 showed any significant effects on TSS concentrations.

(4) Period from 2004 to present – A new gold mining rush characterizes this period, when an increase of 50% in ASGM was observed from 2001 (171.7 km^2) to 2012 (261.7 km^2). Encouraged by the new rise in the price of gold, the Tapajós region has attracted significant investments by medium/large national and foreign companies to extract primary gold in rock deposits with the use of pit-loaders and heavy mills, and trucks, characterizing a new period of 'industrial' mining (Bezerra *et al.*, 1998). The first 'industrial' mines to exploit primary gold are located in the Palito, the Creporizão, and the Marupá areas, characterized by geological formation with higher gold content (CPRM, 2009). Presently, about 35 negotiations have been conducted (joint ventures) involving 19 mining companies (Silva, 2012). This type of mining operation requires higher mechanization levels with the use of several load pitchers (approximately 50, according to the local environment protection agency, ICMBio) and cyanide tanks (Appendix 1). The highly mechanized operation increases the capacity of mineral processing, and potentially increases the impact of water siltation if preventive actions are not taken.

In this period, the economic scenario has been very favourable, not only for companies exploiting primary deposits, but also for ASGM to take place over unexploited alluvial and colluvial deposits. Therefore, the total mining area increase from 2001 to 2012 is possibly a result of a combination of the increase in primary ore

(industrial), and an increase in mining operations using water-jets systems on hillsides. The increase in ASGM area, associated with the new mining techniques, resulted in a TSS increase from about 30.0 to above 100 mg/L in the Tocantins River, for example (Figure 5.9). The change in the Novo River was smaller, but high TSS values were also observed (~50.0 mg/L). In the Crepori River, the large extent of the mining area has a direct impact on the TSS concentrations throughout the decades, however, the TSS concentrations in 2012 (~75 mg/L) were not as high as in 1993 (>300 mg/L) (Figure 5.9a and 5.10). This can be attributed to a few factors: i) reduced numbers of miners ('garimpeiros'), and thus fewer active mining sites ('garimpos'); ii) presence of medium-sized mining companies that have more control over their tailings, thus avoiding high sediment/tailing release into the waters; and iii) reduced numbers of rafts along the tributaries in 2012, which are currently prohibited (Silva, 2012; Fernandes *et al.*, 2014). Although the current TSS concentrations are not as high as in 1993, the high sediment concentration, mainly in the Tocantins and Novo rivers, raises awareness for better water quality control in the present and near future.

5.6 Conclusions

This research aimed to contribute to a comprehensive evaluation of the impacts of ASGM activities on the water quality of the Tapajós River Basin by evaluating the associated temporal changes (1973, 1984, 1993, 2001, and 2012) on the mining area in the Jamanxim, Crepori, Tocantins, and Novo sub-basins. First, the spatial and temporal distribution of ASGM in four sub-basins of the Tapajós River Basin over a 40-year period based on satellite images were quantified. To map the current mining area, the

land cover product from the *Terraclass* project (INPE, 2011) was validated with aerial photos, and showed an approximately 50% omission of mining areas. The same classification after precise vector edition showed a better performance with an overall accuracy of 93%. As a result, a total mining area of 261.7 km^2 was quantified in 2012, distributed mainly over three sub-basins: Crepori, Novo, and Tocantins. Secondly, this classification was used as a reference for a backward Landsat-based chronological classification of mining areas in 2001 (171.7 km^2), 1993 (166.3 km^2), 1984 (47.5 km^2), and 1973 (15.4 km^2). The temporally quantified mining areas were subsequently correlated with satellite-based temporal TSS concentrations for each specific sub-basin as defined in Lobo *et al.* (2015).

In general, as mining area increased so did TSS concentrations for all sub-basins with significant ASGM. However, this association also depends on several other factors regarding ASGM activities, such as the applied mining technique (pans, drafts, water-jets, industrial methods), type of exploited gold deposits (alluvial, colluvial, quartz veins deposits), and intensity of gold mining, represented by number of miners and gold production. The combination of these factors define four main chronological periods of changes in the water quality of the studied rivers. The period from 1958 to 1977, characterized by the first mining activities, started employing rudimentary techniques with low sediment processing capacity, resulting in low or non-impacts to water turbidity. The period from 1978 to 1993, characterized by the introduction of low-budget mechanization such as water jets and rafts, associated with very high gold prices, resulted in a substantial increase in mining areas. The majority of the increase in ASGM in this period took place over colluvial deposits located at higher elevations when compared to

alluvial deposits. Overall, exploitation of gold deposits, from both alluvial and colluvial deposits, generates a high volume of clay-rich mining tailings, increasing water siltation to very high levels. The period from 1994 to 2003 was characterized by a general recession of ASGM activities due to a reduction in the price of gold and the exhaustion of easy-access secondary gold deposits. This stagnation period resulted in a general decrease in the TSS concentrations. The period from 2004 to present is characterized by a major intensification of ASGM encouraged by high gold prices, with the presence of mining companies (industrial mining) exploiting primary deposits. The impact of this recent gold rush on water quality is evident, mainly in the Tocantins and Novo tributaries, which raises awareness for implementation of better mining techniques for water quality control in the present and near future.

Chapter 6 – Conclusions

This research investigated the spatial and temporal impacts of Artisanal Small-scale Gold Mining (ASGM) on water siltation, and associated changes in the underwater light field of the Tapajós River and main tributaries. This region has been subjected to ASGM activities since the 1950s, followed by a significant gold rush in the 1980s. Today, after a recession period in the late 1990s, a new gold rush is occurring encouraged by elevated gold prices and supported by the introduction of high mechanization techniques. The results derived from field studies in 2011 (high water) and 2012 (low water level) showed that tributaries draining areas with more extensive ASGM, such as Crepori, Novo, and Tocantins, have higher Total Suspended Solids (TSS) concentration. With increasing TSS, the scattering process prevails over absorption coefficient, reducing critical depth (Z_c) from 7.0 m in pristine tributaries to approximately 1.5 m in highly impacted rivers. Moreover, higher TSS values, and therefore higher light attenuation, were observed during the dry period, when the water level is low and ASGM activities are more intense. Within a 40-year period, two gold rushes have occurred due to increasing gold prices, and with some governmental support. The first started in the late 1980s, and the current gold rush started in 2005. Extending the optical changes caused by water siltation in 2011/2012 (Chapter 3) to the historical water quality derived from satellite images (Chapter 4), it is approximated that in the 1970s the pristine condition of the waters had critical depth >6.0 m over the whole water basin. During the first gold rush (late 1980s and early 1990s), the sediment derived from ASGM (TSS >200 mg/L) reduced critical depth to less than 2.0 m in all mined tributaries. In the following decade (2000s), a recession of ASGM allowed water quality to recover, reducing TSS to at least half of that

in the previous decade and, consequently, increasing light availability. Today, with the current gold rush, water siltation has increased, reducing light availability to 1.5 m in highly impacted rivers such as the Crepori and Tocantins. This research provides the first comprehensive analysis of the impacts of ASGM on water quality and light fields on relatively large spatial and temporal scales.

In Chapter 3, the *in situ* biogeochemical and optical data provided information for quantifying the underwater light field of rivers that are subject to a gradient of mining tailings intensity, clustered into five major classes varying from 3.0 to 120.0 mg/L of TSS. This dataset shows that the TSS concentration varies seasonally in a synergism between water level and mining activities, whereby mining activities intensify during low water level periods and, associated with low water volume, TSS rapidly increases. Associated with the intensified mining activities, and consequently higher TSS concentrations, the inherent and apparent optical properties showed that the inorganic nature of mine tailings is the main factor affecting the underwater scalar irradiance in the Tapajós River Basin. Specifically, for waters with low or no influence from mine tailings, light absorption dominates over scattering. With increased TSS loadings from mining operations, the scattering process prevails over absorption coefficient, and, at sub-surface, scalar irradiance is reduced, resulting in a shallower euphotic zone, where green and red wavelengths dominate. A quantifiable association of the effects of this light reduction on the phytoplankton community was not clearly observed, which might be attributable to a low number of samples for proper comparison between impacted and non-impacted tributaries, and/or to generally low phytoplankton productivity in all upstream tributaries. The overall low phytoplankton productivity observed can be a

result of the oligotrophic nature of the biogeochemistry characteristics of the drainage area of these rivers, associated with other factors, including flood pulse, water velocity, and seasonal variation of incoming irradiance.

In Chapter 4, the spatial and temporal distribution of TSS concentrations over the past 40 years based on satellite imagery was presented. The dataset showed two time scale trends. The first demonstrated that during the high water period, TSS concentrations are consistently lower than those during the low water period due to a combination of high dilution and low mining activity (similar to results from Chapter 3, based on *in situ* data). The larger scale analysis showed that, in a four decade period, the peak of sediment concentration coincides with the peak of gold production in all sites, likely motivated by high gold prices during the early 1990s. More recently, due to the current gold rush, a TSS increase has been observed mainly in the Novo and Tocantins rivers, where industrial mining has been installed.

Chapter 5 provides an analysis of satellite-based land cover change due to the historical ASGM and consequent impacts on water quality for the past 40 years of mining operations based on mining techniques, gold price, government support, and seasonal variation. The analyzed dataset shows that the effects of ASGM on water siltation depends on several factors regarding ASGM activities, such as the type of mining techniques, type of gold deposits, and intensity of gold mining, represented by the number of miners and gold production. Overall, four main periods of ASGM were identified in the Tapajós Region:

- 1958 - 1977, characterized by the first mining activities and low water impacts (total ASGM land-cover area in 1973 = 15.4 km^2);

- 1978 - 1993, characterized by the introduction of low-budget mechanization, associated with very high gold prices, resulted in a substantial increase in mining areas and water siltation (ASGM land-cover area in 1993 = 166.5 km^2);
- 1994 - 2003, characterized by a general recession in ASGM activities due to reduction of gold prices and exhaustion of secondary, easy-access gold deposits, decreasing TSS concentrations (ASGM land-cover area in 2001 = 171.1 km^2);
- 2004 to present, intensification of ASGM encouraged by high gold prices, resulting in an increase of TSS (ASGM land-cover area in 2012 = 266.1 km^2).

The variation of water siltation and consequential changes in the in-water light field in the Tapajós River Basin is highly associated with ASGM activities in time and space. In the 1970s, mining activities had just begun in the Crepori and Novo rivers (Total ASGM = 15.4 km^2), resulting in clear water condition (TSS ~ 5 mg/L) for all tributaries analyzed in this study. Extending optical information from water classes (Chapter 3) to the historical TSS database (Chapter 4), I suggest that the critical depth in the 1970s was above 6.0 m for all tributaries and the Tapajós main channel, and no sediment plume was observed. In the following decade, when gold prices reached the highest value observed to date, a new modern gold rush started, encouraging thousands of miners into the Tapajós region, mostly the Crepori, Novo, and Tocantins sub-basins (Total ASGM area = 166.5 km^2). As a consequence of intense mining operations using dredges and water-jet systems in alluvial deposits during this decade, a large amount of sediment (mostly clay) was discharged into the drainage system, increasing TSS concentrations to the highest value historically observed (based on the imagery, TSS >200.0 mg/L for impacted

tributaries). These TSS levels suggest that critical depth for phytoplankton was likely less than 1.0 m of depth for all mined tributaries. From 1994 to 2003, a recession of ASGM occurred due to a reduction in gold prices. The ASGM areas stopped expanding (Total ASGM area = 171.7 km^2), and water quality improved for all tributaries analyzed (TSS concentrations decreased to at least half of those from the previous decades), increasing light availability and critical depth. However, the gold price increase in the past 10 years has triggered a new gold rush in this region (Total ASGM area = 261.7 km^2). Medium-sized companies with high ore-processing capacity started to exploit primary deposits with the use of pit-loaders and cyanide-tanks. The combination of medium-sized and ASGM activities resulted in an increase of TSS, especially in Tocantins River, where TSS values increased from ~30.0 (2001) to 130.0 mg/L (2012), reducing critical depth from approximately 3.75 m to 1.5 m in this river.

This research provided a quantified baseline of TSS, which represents the conditions in the 1970s before gold mining activities intensified to the current status, and an analysis of the possible changes in the in-water light environment as a result of mining activities. This research also showed the changes in land cover due to mining activities, and associated temporal variation of TSS in the most important tributaries, which also indicates current mining activity hot spots in the region. Considering the importance of water quality for aquatic systems and for local people (water supply, fish markets, and tourism), the results derived from this paper can support further investigation on sediment transportation and precipitation process along the Tapajós River Basin.

Lastly, the ASGM historical maps reported here, and the developed analytical framework, can be used not only for water siltation investigations, but also for land

management studies as several conflicts have emerged from ASGM activities in protected areas, and conflicts among miners about property claims (Rodrigues *et al.*, 1994; Araújo Neto, 2009; Fernandes *et al.*, 2014). This database will be shared with numerous governmental and non-governmental organizations that have contributed directly or indirectly to this project, or are interested in the information related to ASGM distribution in the Tapajós region. These organizations include environmental agencies (ICMBio, IBAMA, SEMA), mineral resources agencies (DNPM, CPRM, CETEM), federal institutes (INPE, IES/FUNASA, ANA), ASGM organizations (AMOT, all acronyms in Portuguese referring to Brazilian organizations), and international organizations (Artisanal Gold Council and Mining Institute at the University of British Columbia). Similar analytical frameworks incorporating historical satellite imagery, geological and topographical characteristics, and optical data can be applied to other mined areas of the world, for example, in the French-Guiana and Suriname. This would allow a better understanding of the impacts of ASGM on the water quality of rivers.

Bibliography

Albert, A. & Mobley, C. D. (2003). An analytical model for subsurface irradiance and remote sensing reflectance in deep and shallow case-2 waters. *Optics Express* 11(22): 2873-2890.

Allan, J. D. & Castillo, M. M. (2007). *Stream Ecology: Structure and function of running waters.* Springer.

ANA (2013). HidroWeb: sistemas de informações hidrológicas. *http://hidroweb.ana.gov.br/HidroWeb accessed in May, 2013*.

APHA (2005). *Standard methods for the examination of water and wastewater.* Washington, D.C.: APHA-AWWA-WEF.

Araújo Neto, H. (2009). *Perfil do Ouro.* Brasília: Ministério de Minas e Energia.

Asner, G. P. (1998). Biophysical and Biochemical Sources of Variability in Canopy Reflectance. *Remote Sensing of Environment* 64(3): 234-253.

Bailey, S. W. & Werdell, P. J. (2006). A multi-sensor approach for the on-orbit validation of ocean color satellite data products. *Remote Sensing of Environment* 102(1-2): 12-23.

Bale, A. J., Tocher, M. D., Weaver, R., Hudson, S. J. & Aiken, J. (1994). Laboratory measurements of the spectral properties of estuarine suspended particles. *Netherland Journal of Aquatic Ecology* 28(3-4): 237-244.

Barbosa, C., Moraes Novo, E., Melack, J., Gastil-Buhl, M. & Filho, W. (2010). Geospatial analysis of spatiotemporal patterns of pH, total suspended sediment and chlorophyll-a on the Amazon floodplain. *Limnology* 11(2): 155-166.

Bergmann, T. (2004). Impacts of a recurrent resuspension event and variable phytoplankton community composition on remote sensing reflectance. *Journal of Geophysical Research* 109(C10).

Bernardes, M. C., Martinelli, L. A., Krusche, A. V., Gudeman, J., Moreira, M., Victoria, R. L., Ometto, J., Ballester, M. V. R., Aufdenkampe, A. K., Richey, J. E. & Hedges, J. I. (2004). Riverine organic matter composition as a function of land use changes, Southwest Amazon. *Ecological Applications* 14(4): S263-S279.

Bezerra, O., Veríssimo, A. & Uhl, C. (1998). *Impactos da garimpagem de ouro na Amazônia Oriental.* Belém/PA: Imazon.

Binding, C. E., Bowers, D. G. & Mitchelson-Jacob, E. G. (2005). Estimating suspended sediment concentrations from ocean colour measurements in moderately turbid waters; the impact of variable particle scattering properties. *Remote Sensing of Environment* 94(3): 373-383.

Boss, E. & Pegau, W. S. (2001). Relationship of light scattering at an angle in the backward direction to the backscattering coefficient. *Applied Optics* 40(30): 5503-5507.

Bowers, D. G. & Binding, C. E. (2006). The optical properties of mineral suspended particles: A review and synthesis. *Estuarine Coastal and Shelf Science* 67(1-2): 219-230.

Brando, P. M., Goetz, S. J., Baccini, A., Nepstad, D. C., Beck, P. S. A., Christman, M. C. & DeFries, R. S. (2010). Seasonal and interannual variability of climate and vegetation indices across the Amazon.

Proceedings of the National Academy of Sciences of the United States of America 107(33): 14685-14690.

Bricaud, A., Bédhomme, A.-L. & Morel, A. (1988). Optical properties of diverse phytoplanktonic species: experimental results and theoretical interpretation. *Journal of Plankton Research* 10(5): 851-873.

Buchaca, T. (2004). A comparison of HPLC pigment analyses and biovolume estimates of phytoplankton groups in an oligotrophic lake. *Journal of Plankton Research* 27(1): 91-101.

Câmara, V. d. & Corey, G. (1992). *O caso dos garimpos de ouro no Brasil.* Metepec, Mexico: Pan American Center For Human Ecology and Health, WHO.

Campbell, G., Phinn, S. R. & Daniel, P. (2011). The specific inherent optical properties of three sub-tropical and tropical water reservoirs in Queensland, Australia. *Hydrobiologia* 658(1): 233-252.

Carvalho, L. A. S. d., Barbosa, C. C. F., Novo, E. M. L. d. M. & Rudorff, C. d. M. (2015). Implications of scatter corrections for absorption measurements on optical closure of Amazon floodplain lakes using the Spectral Absorption and Attenuation Meter (AC-S-WETLabs). *Remote Sensing of Environment* 157(0): 123-137.

Casali, S., Calijuri, M. d. C., Barbarisi, B., Renó, V. F., Affonso, A. G., Barbosa, C., Silva, T. S. F. & Novo, E. M. L. d. M. (2011). Impact of the 2009 extreme water level variation on phytoplankton community structure in Lower Amazon floodplain lakes. *Acta limnológica brasiliensia* 23: 260-270.

Castilla, J. C. (1983). Environmental-Impact in Sandy Beaches of Copper Mine Tailings at Chanaral, Chile. *Marine pollution bulletin* 14(12): 459-464.

Coelho-Souza, S. A., Guimarães, J. R. D., Miranda, M. R., Poirier, H., Mauro, J. B. N., Lucotte, M. & Mergler, D. (2011). Mercury and flooding cycles in the Tapajós river basin, Brazilian Amazon: The role of periphyton of a floating macrophyte (Paspalum repens). *Science of the Total Environment* 409(14): 2746-2753.

Costa, M. P. F., Novo, E. M. L. M. & Telmer, K. H. (2013). Spatial and temporal variability of light attenuation in large rivers of the Amazon. *Hydrobiologia* 702(1): 171-190.

CPRM (2009). Província mineral do Tapajós: geologia, metalogenia e mapa previsional para ouro em SIG. *http://www.cprm.gov.br accessed in April, 2013.*

Davies-Colley, R., Hickey, C., Quinn, J. & Ryan, P. (1992). Effects of clay discharges on streams. *Hydrobiologia* 248(3): 215-234.

Deblois, C. P., Marchand, A. & Juneau, P. (2013). Comparison of Photoacclimation in Twelve Freshwater Photoautotrophs (Chlorophyte, Bacillaryophyte, Cryptophyte and Cyanophyte) Isolated from a Natural Community. *PLoS ONE* 8(3): e57139.

Dekker, A. G., Vos, R. J. & Peters, S. W. M. (2001). Comparison of remote sensing data, model results and in situ data for total suspended matter (TSM) in the southern Frisian lakes. *Science of the Total Environment* 268(1-3): 197-214.

Dekker, A. G., Vos, R. J. & Peters, S. W. M. (2002). Analytical algorithms for lake water TSM estimation for retrospective analyses of TM and SPOT sensor data. *International Journal of Remote Sensing* 23(1): 15-35.

DGI/INPE (2013). Divisão de Geração de Imagens. *www.dgi.inpe.br accessed in May, 2013.*

DNPM (2013). Sumário Mineral, 32. *http://www.dnpm.gov.br/ accessed in April, 2013.*

Dokulil, M. T. (2014). Potamoplankton and primary productivity in the River Danube. *Hydrobiologia* 729(1): 209-227.

Dorea, J. G. & Barbosa, A. C. (2007). Anthropogenic impact of mercury accumulation in fish from the Rio Madeira and Rio Negro rivers (Amazonia). *Biological Trace Element Research* 115(3): 243-254.

Doxaran, D., Ehn, J., Bélanger, S., Matsuoka, A., Hooker, S. & Babin, M. (2012). Optical characterisation of suspended particles in the Mackenzie River plume (Canadian Arctic Ocean) and implications for ocean colour remote sensing. *Biogeosciences* 9(8): 3213-3229.

Dustan, P. (2009). Terrestrial limitation of Amazon River productivity: why the Amazon River is not green. *Evolutionary ecology research* 11(3): 421.

Farella, N., Lucotte, M., Louchouarn, P. & Roulet, M. (2001). Deforestation modifying terrestrial organic transport in the Rio Tapajós, Brazilian Amazon. *Organic Geochemistry* 32(12): 1443-1458.

Fernandes, F. R. C., Alamino, R. d. C. J. & Araújo, E. R. (2014). *Recursos minerais e comunidade: impactos humanos, socioambientais e econômicos.* Rio de Janeiro: CETEM/MCTI.

Fujiki, T. & Taguchi, S. (2002). Variability in chlorophyll a specific absorption coefficient in marine phytoplankton as a function of cell size and irradiance. *Journal of Plankton Research* 24(9): 859-874.

Gao, B.-C., Montes, M. J., Davis, C. O. & Goetz, A. F. H. (2009). Atmospheric correction algorithms for hyperspectral remote sensing data of land and ocean. *Remote Sensing of Environment* 113, Supplement 1(0): S17-S24.

Gibbs, R. J. (1967). Amazon river: environmental factors that control its dissolved and suspended load. *Science (New York, N.Y.)* 156(3783): 1734-1737.

Gong, S., Huang, J., Li, Y. & Wang, H. (2008). Comparison of atmospheric correction algorithms for TM image in inland waters. *International Journal of Remote Sensing* 29(8): 2199-2210.

Gordon, H. R. & Wang, M. (1994). Retrieval of water-leaving radiance and aerosol optical thickness over the oceans with SeaWiFS: a preliminary algorithm. *Applied Optics* 33(3): 443-452.

Gordon, H. R., Lewis, M. R., McLean, S. D., Twardowski, M. S., Freeman, S. A., Voss, K. J. & Boynton, G. C. (2009). Spectra of particulate backscattering in natural waters. *Optics Express* 17(18): 16192-16208.

Grätz, T. (2009). Moralities, risk and rules in West African artisanal gold mining communities: A case study of Northern Benin. *Resources Policy* 34(1-2): 12-17.

Guanter, L., Ruiz-Verdú, A., Odermatt, D., Giardino, C., Simis, S., Estellés, V., Heege, T., Domínguez-Gómez, J. A. & Moreno, J. (2010). Atmospheric correction of ENVISAT/MERIS data over inland waters: Validation for European lakes. *Remote Sensing of Environment* 114(3): 467-480.

Guenther, M. & Bozelli, R. (2004). Effects of inorganic turbidity on the phytoplankton of an Amazonian Lake impacted by bauxite tailings. *Hydrobiologia* 511(1): 151-159.

Guyot, J. L., Jouanneau, J. M., Soares, L., Boaventura, G. R., Maillet, N. & Lagane, C. (2007). Clay mineral composition of river sediments in the Amazon Basin. *Catena* 71(2): 340-356.

Hadjimitsis, D. G. & Clayton, C. (2009). Assessment of temporal variations of water quality in inland water bodies using atmospheric corrected satellite remotely sensed image data. *Environmental Monitoring and Assessment* 159(1-4): 281-292.

Hansell, D. A. (2001). Biogeochemistry of total organic carbon and nitrogen in the Sargasso Sea: control by convective overturn. *Deep-sea research. Part II, Topical studies in oceanography* 48(8-9): 1649-1667.

Harrington Jr, J. A., Schiebe, F. R. & Nix, J. F. (1992). Remote sensing of Lake Chicot, Arkansas: Monitoring suspended sediments, turbidity, and Secchi depth with Landsat MSS data. *Remote Sensing of Environment* 39(1): 15-27.

Hedley, J. D., Harborne, A. R. & Mumby, P. J. (2005). Technical note: Simple and robust removal of sun glint for mapping shallow-water benthos. *International Journal of Remote Sensing* 26(10): 2107-2112.

Hillebrand, H., Dürselen, C., Kirschtel, D., Pollingher, U. & Zohary, T. (1999). Biovolume calculation for pelagic and benthic algae. *Journal of phycology* 35(2): 403-424.

Hochberg, E. J., Andrefouet, S. & Tyler, M. R. (2003). Sea surface correction of high spatial resolution ikonos images to improve bottom mapping in near-shore environments. *IEEE transactions on geoscience and remote sensing* 41(7): 1724-1729.

Holben, B. N., Eck, T. F., Slutsker, I., Tanré, D., Buis, J. P., Setzer, A., Vermote, E., Reagan, J. A., Kaufman, Y. J., Nakajima, T., Lavenu, F., Jankowiak, I. & Smirnov, A. (1998). AERONET—A Federated Instrument Network and Data Archive for Aerosol Characterization. *Remote Sensing of Environment* 66(1): 1-16.

Hu, C., Muller-Karger, F. E., Andrefouet, S. & Carder, K. L. (2001). Atmospheric correction and cross-calibration of LANDSAT-7/ETM+ imagery over aquatic environments: A multiplatform approach using SeaWiFS/MODIS. *Remote Sensing of Environment* 78(1–2): 99-107.

Huisman, J., Sharples, J., Stroom, J. M., Visser, P. M., Kardinaal, W. E. A., Verspagen, J. M. H. & Sommeijer, B. (2004). Changes in turbulent mixing shift competition for light between phytoplankton species. *Ecology* 85(11): 2960-2970.

ICMBIO (2010).Plano de Manejo - Floresta Nacional do Crepori - State of Pará. Vol. 1, 56 (Ed I. C. M. d. C. d. Biodiversidade). Curitiba., Brazil: Resumo Executivo.

INPE (2008).Topodata: Banco de dados geomorfométricos do Brasil. Vol. 2014São José dos Campos/SP.

INPE (2011). PRODES Project. *www.obt.inpe.br/prodes accessed in Jun, 2011.*

Junk, W. (1997).General Aspects of Floodplain Ecology with Special Reference to Amazonian Floodplains. In *The Central Amazon Floodplain*, Vol. 126, 3-20 (Ed W. Junk). Springer Berlin Heidelberg.

Kaufman, Y. J., Wald, A. E., Remer, L. A., Bo-Cai, G., Rong-Rong, L. & Flynn, L. (1997). The MODIS 2.1-μm channel-correlation with visible reflectance for use in remote sensing of aerosol. *Geoscience and Remote Sensing, IEEE Transactions on* 35(5): 1286-1298.

Kilham, N. E. & Roberts, D. (2011). Amazon River time series of surface sediment concentration from MODIS. *International Journal of Remote Sensing* 32(10): 2659-2679.

Kirk, J. T. O. (2011). *Light and photosynthesis in aquatic ecosystems.* Cambridge, Cambs, UK ; New York: Cambridge University Press.

Kishino, M. (1986). Light utilization efficiency and quantum yield of phytoplankton in a thermally stratified sea. *Limnology and Oceanography* 31(3): 557-566.

Kruk, C., Huszar, V. L. M., Peeters, E. T. H. M., Bonilla, S., Costa, L., LÜRling, M., Reynolds, C. S. & Scheffer, M. (2010). A morphological classification capturing functional variation in phytoplankton. *Freshwater Biology* 55(3): 614-627.

Kutser, T., Hire, M., Metsamaa, L., Vahtmaee, E., Paavel, B. & Aps, R. (2009). Field measurements of spectral backscattering coefficient of the Baltic Sea and boreal lakes. *Boreal Environment Research* 14(2): 305-312.

Kutser, T., Vahtmäe, E., Paavel, B. & Kauer, T. (2013). Removing glint effects from field radiometry data measured in optically complex coastal and inland waters. *Remote Sensing of Environment* 133: 85-89.

Le, C. F., Li, Y. M., Zha, Y., Sun, D. & Yin, B. (2009). Validation of a Quasi-Analytical Algorithm for Highly Turbid Eutrophic Water of Meiliang Bay in Taihu Lake, China. *Geoscience and Remote Sensing, IEEE Transactions on* 47(8): 2492-2500.

Li, L., Li, L., Song, K., Li, Y., Tedesco, L. P., Shi, K. & Li, Z. (2013). An inversion model for deriving inherent optical properties of inland waters: Establishment, validation and application. *Remote Sensing of Environment* 135: 150-166.

Liew, S. C., Saengtuksin, B. & Kwoh, L. K. (2009).Monitoring turbidity and suspended sediment concentration of coastal and inland waters using satellite data. In *Geoscience and Remote Sensing Symposium,2009 IEEE International,IGARSS 2009*, Vol. 2, II-837-II-839.

Lobo, F., Costa, M. P. F., Phillips, S., Young, E. & McCregor, C. (2014). Light backscattering in turbid freshwater: A laboratory investigation. *Journal of Applied Remote Sensing*.

Lobo, F. d. L., Novo, E. M. L. d. M., Barbosa, C. C. F. & Galvão, L. S. (2012). Reference spectra to classify Amazon water types. *International Journal of Remote Sensing* 33(11): 3422-3442.

Lobo, F. L., Costa, M. P. F. & Novo, E. M. (2015). Time-series analysis of Landsat-MSS/TM/OLI images over Amazonian waters impacted by gold mining activities. *Remote Sensing of Environment* 157(Special Issue: Remote Sensing of Inland Waters): 170-184.

Lorthiois, T., Doxaran, D. & Chami, M. (2012). Daily and seasonal dynamics of suspended particles in the Rhône River plume based on remote sensing and field optical measurements. *Geo-Marine Letters* 32(2): 89-101.

Lu, D., Mausel, P., Brondizio, E. & Moran, E. (2002). Assessment of atmospheric correction methods for Landsat TM data applicable to Amazon basin LBA research. *International Journal of Remote Sensing* 23(13): 2651-2671.

Lu, D., Mausel, P., Brondízio, E. & Moran, E. (2004). Relationships between forest stand parameters and Landsat TM spectral responses in the Brazilian Amazon Basin. *Forest Ecology and Management* 198(1-3): 149-167.

Lund, J., Kipling, C. & LeCren, E. (1958). The inverted microscope method of estimating algal number and the statistical basis of estimation by count. *Hydrobiologia* 11: 143-170.

Markager, S. & Vincent, W. F. (2001). Light absorption by phytoplankton: development of a matching parameter for algal photosynthesis under different spectral regimes. *Journal of Plankton Research* 23(12): 1373-1384.

Masek, J. G., Vermote, E. F., Saleous, N. E., Wolfe, R., Hall, F. G., Huemmrich, K. F., Feng, G., Kutler, J. & Teng-Kui, L. (2006). A Landsat surface reflectance dataset for North America, 1990-2000. *Geoscience and Remote Sensing Letters, IEEE* 3(1): 68-72.

Meade, R. H. (1994). Suspended sediments of the modern Amazon and Orinoco rivers. *Quaternary International* 21(0): 29-39.

Melack, J. & Forsberg, B. (2001). Biogeochemistry of Amazon floodplain lakes and associated wetlands. *The biogeochemistry of the Amazon basin and its role in a changing world*: 235-276.

Mertes, L. A. K., Smith, M. O. & Adams, J. B. (1993). Estimating Suspended Sediment Concentrations in Surface Waters of the Amazon River Wetlands from Landsat Images. *Remote Sensing of Environment* 43(3): 281-301.

MMA (2010).Geographical Data: i3Geo. Vol. 2013Brasília: Ministério do Meio Ambiente.

Mobley, C. D. (1994). *Light and Water: Radiative Transfer in Natural Waters.* Academic Press.

Mobley, C. D., Boss, E. & Roesler, C. (2010).Ocean optics web book.

Mobley, C. D., Sundman, L. K. & Boss, E. (2002). Phase function effects on oceanic light fields. *Applied Optics* 41(6): 1035-1050.

Mol, J. H. & Ouboter, P. E. (2004). Downstream effects of erosion from small-scale gold mining on the instream habitat and fish community of a small neotropical rainforest stream. *Conservation Biology* 18(1): 201-214.

Moran, M. S., Bryant, R., Thome, K., Ni, W., Nouvellon, Y., Gonzalez-Dugo, M. P., Qi, J. & Clarke, T. R. (2001). A refined empirical line approach for reflectance factor retrieval from Landsat-5 TM and Landsat-7 ETM+. *Remote Sensing of Environment* 78(1–2): 71-82.

NASA/GSFC (2013). Aerosol Robotic Network (AERONET). *http://aeronet.gsfc.nasa.gov in Mar, 2013*.

Neill, C., Deegan, L. A., Thomas, S. M., Haupert, C. L., Krusche, A. V., Ballester, V. M. & Victoria, R. L. (2006). Deforestation alters the hydraulic and biogeochemical characteristics of small lowland Amazonian streams. *Hydrological Processes* 20(12): 2563-2580.

Neill, C., Chaves, J. E., Biggs, T., Deegan, L. A., Elsenbeer, H., Figueiredo, R. O., Germer, S., Johnson, M. S., Lehmann, J., Markewitz, D. & Piccolo, M. C. (2011). Runoff sources and land cover change in the Amazon: an end-member mixing analysis from small watersheds. *Biogeochemistry* 105(1-3): 7-18.

Nery, M. A. C. & Silva, E. A. d. (2002).Balanço Mineral Brasileiro: Ouro. In *Economia Mineral*: DNPM (Departamento Mineral de Produção Mineral).

Nevado, J. J. B., Martin-Doimeadios, R. C. R., Bernardo, F. J. G., Moreno, M. J., Herculano, A. M., do Nascimento, J. L. M. & Crespo-Lopez, M. E. (2010). Mercury in the Tapajos River basin, Brazilian Amazon: A review. *Environment International* 36(6): 593-608.

Novo, E., Barbosa, C. C. D., de Freitas, R. M., Shimabukuro, Y. E., Melack, J. M. & Pereira, W. (2006). Seasonal changes in chlorophyll distributions in Amazon floodplain lakes derived from MODIS images. *Limnology* 7(3): 153-161.

O'Neill, J. D. & Costa, M. (2013). Mapping eelgrass (Zostera marina) in the Gulf Islands National Park Reserve of Canada using high spatial resolution satellite and airborne imagery. *Remote Sensing of Environment* 133(0): 152-167.

Odermatt, D., Gitelson, A., Brando, V. E. & Schaepman, M. (2012). Review of constituent retrieval in optically deep and complex waters from satellite imagery. *Remote Sensing of Environment* 118: 116-126.

Pahlevan, N. & Schott, J. R. (2013). Leveraging EO-1 to Evaluate Capability of New Generation of Landsat Sensors for Coastal/Inland Water Studies. *Selected Topics in Applied Earth Observations and Remote Sensing, IEEE Journal of* 6(2): 360-374.

Puttonen, E., Suomalainen, J., Hakala, T. & Peltoniemi, J. (2009). Measurement of Reflectance Properties of Asphalt Surfaces and Their Usability as Reference Targets for Aerial Photos. *Geoscience and Remote Sensing, IEEE Transactions on* 47(7): 2330-2339.

Rabitto, I. d. S., Bastos, W. R., Almeida, R., Anjos, A., de Holanda, Í. B. B., Galvão, R. C. F., Neto, F. F., de Menezes, M. L., dos Santos, C. A. M. & de Oliveira Ribeiro, C. A. (2011). Mercury and DDT exposure risk to fish-eating human populations in Amazon. *Environment International* 37(1): 56-65.

Reinart, A., Paavel, B., Pierson, D. & Strombeck, N. (2004). Inherent and apparent optical properties of Lake Peipsi, Estonia. *Boreal Environment Research* 9(5): 429-445.

Reynolds, C. S. (2006). *The ecology of phytoplankton.* Cambridge, UK ; New York: Cambridge University Press.

Reynolds, C. S., Descy, J. P. & Padisák, J. (1994). Are phytoplankton dynamics in rivers so different from those in shallow lakes? *Hydrobiologia* 289(1-3): 1-7.

Robert, A. (2014). *River processes: an introduction to fluvial dynamics.* Routledge.

Rodrigues, R. M., Mascarenhas, A. F. S., Ichihara, A. H. & Souza, T. M. C. (1994). *Estudo dos impactos ambientais decorrentes do extrativismo mineral e poluição mercurial no Tapajós - Pré-Diagnóstico.* Rio de Janeiro: CETEM/CNPq.

Roland, F. & Esteves, F. D. (1998). Effects of bauxite tailing on PAR attenuation in an Amazonian crystalline water lake. *Hydrobiologia* 377(Journal Article): 1-7.

Roulet, M., Lucotte, M., Canuel, R., Rheault, I., Tran, S., Gog, Y. G. D., Farella, N., do Vale, R. S., Passos, C. J. S., da Silva, E. D., Mergler, D. & Amorim, M. (1998). Distribution and partition of total mercury in waters of the Tapajos River Basin, Brazilian Amazon. *Science of the Total Environment* 213(1-3): 203-211.

Roulet, M., Lucotte, M., Canuel, R., Farella, N., Goch, Y. G. D., Peleja, J. R. P., Guimaraes, J. R. D., Mergler, D. & Amorim, M. (2001). Spatio-temporal geochemistry of mercury in waters of the Tapajos and Amazon rivers, Brazil. *Limnology and Oceanography* 46(5): 1141-1157.

Ruddick, K. G., Ovidio, F. & Rijkeboer, M. (2000). Atmospheric Correction of SeaWiFS Imagery for Turbid Coastal and Inland Waters. *Applied Optics* 39(6): 897-912.

Rudorff, C. M., Galvao, L. S. & Novo, E. M. L. M. (2009a). Reflectance of floodplain waterbodies using EO-1 Hyperion data from high and receding flood periods of the Amazon River. *International Journal of Remote Sensing* 30(10): 2713-2720.

Sá, L. L. C. d., Vieira, J. M. d. S., Mendes, R. d. A., Pinheiro, S. C. C., Vale, E. R., Alves, F. A. d. S., Jesus, I. M. d., Santos, E. C. d. O. & Costa, V. B. d. (2010). Ocorrência de uma floração de cianobactérias tóxicas na margem direita do Rio Tapajós, no Município de Santarém (Pará, Brasil). *Revista Pan-Amazônica de Saúde* 1: 159-166.

Salmaso, N. & Zignin, A. (2010). At the extreme of physical gradients: phytoplankton in highly flushed, large rivers. *Hydrobiologia* 639(1): 21-36.

Santer, R. & Schmechtig, C. (2000). Adjacency Effects on Water Surfaces: Primary Scattering Approximation and Sensitivity Study. *Appl. Opt.* 39(3): 361-375.

Santos, J. O. S., Groves, D. & Hartmann, L. (2001). Gold deposits of the Tapajós and Alta Floresta Domains, Tapajós–Parima orogenic belt, Amazon Craton, Brazil. *Mineralium deposita* 36(3-4): 278-299.

Satlantic (2011).ProSoft 7.7 User Manual. In *SAT-DN-00228*(Ed http://satlantic.com/sites/default/files/documents/ProSoft-7.7-%20Manual.pdf). Halifax, Nova Scotia (Canada): Satlantic Inc.

Schueler, V., Kuemmerle, T. & Schroeder, H. (2011). Impacts of Surface Gold Mining on Land Use Systems in Western Ghana. *Ambio* 40(5): 528-539.

Seccatore, J. (2014). An estimation of the artisanal small-scale production of gold in the world. *The Science of the total environment*.

Seyler, P. T. & Boaventura, G. R. (2003). Distribution and partition of trace metals in the Amazon basin. *Hydrological Processes* 17(7): 1345-1361.

SiBCS (2006). *Sistema brasileiro de classificação de solos.* Rio de Janeiro: Embrapa Solos.

Siegel, D. A., Doney, S. C. & Yoder, J. A. (2002). The North Atlantic Spring Phytoplankton Bloom and Sverdrup's Critical Depth Hypothesis. *Science* 296(5568): 730-733.

Silva, A. R. (2012). *A indústria mineral no Pará.* Belém.

Sioli, H. (1984).The Amazon and its main affluents: Hydrography, morphology of the river courses, and river types. In *The Amazon*, Vol. 56, 127-165 (Ed H. Sioli). Springer Netherlands.

Sousa, R. N. & Veiga, M. M. (2009). Using Performance Indicators to Evaluate an Environmental Education Program in Artisanal Gold Mining Communities in the Brazilian Amazon. *Ambio* 38(1): 40-46.

Stomp, M., Huisman, J., de Jongh, F., Veraart, A. J., Gerla, D., Rijkeboer, M., Ibelings, B. W., Wollenzien, U. I. A. & Stal, L. J. (2004). Adaptive divergence in pigment composition promotes phytoplankton biodiversity. *Nature* 432(7013): 104-107.

Stramski, D., Bricaud, A. & Morel, A. (2001). Modeling the inherent optical properties of the ocean based on the detailed composition of the planktonic community. *Applied Optics* 40(18): 2929-2945.

Stramski, D., Boss, E., Bogucki, D. & Voss, K. J. (2004). The role of seawater constituents in light backscattering in the ocean. *Progress in Oceanography* 61(1): 27-56.

Sun, D., Li, Y., Wang, Q., Gao, J., Lv, H., Le, C. & Huang, C. (2009a). Light scattering properties and their relation to the biogeochemical composition of turbid productive waters: a case study of Lake Taihu. *Applied Optics* 48(11): 1979-1989.

Sun, D., Li, Y., Wang, Q., Le, C., Huang, C. & Wang, L. (2009b). Parameterization of water component absorption in an inland eutrophic lake and its seasonal variability: a case study in Lake Taihu. *International Journal of Remote Sensing* 30(13): 3549-3571.

Sun, D., Li, Y., Wang, Q., Le, C., Lv, H., Huang, C. & Gong, S. (2012). Specific inherent optical quantities of complex turbid inland waters, from the perspective of water classification. *Photochemical & Photobiological Sciences* 11(8): 1299.

Sverdrup, H. (1953). On conditions for the vernal blooming of phytoplankton. *Journal du Conseil* 18(3): 287-295.

Telmer, K., Costa, M., Simões Angélica, R., Araujo, E. S. & Maurice, Y. (2006). The source and fate of sediment and mercury in the Tapajós River, Pará, Brazilian Amazon: Ground- and space-based evidence. *Journal of environmental management* 81(2): 101-113.

Telmer, K. & Stapper, D. (2007). Evaluating and Monitoring Small Scale Gold Mining and Mercury Use: Building a Knowledge-base with Satellite Imagery and Field Work.

Telmer, K. & Veiga, M. (2009). Chapter 6: World Emissions of Mercury from Artisanal and Small Scale Gold Mining. In: N. Pirrone and R. Mason (eds.), *Mercury Fate and Transport in the Global Atmosphere*, 131, DOI: 10.1007/978-0-387-93958-2_6.

Telmer, K. H. (2013). The effect of changing gold prices on Artisanal Mining. http://artisanalgold.blogspot.ca/. *accessed in Jan/2015*. Victoria/BC.

Telmer, K. H. & Persaud, A. (2013). Historical and Modern Government Responses to Artisanal and Small Scale Gold Mining. *Rocky Mountain Mineral Law Foundation (RMMLF) and the International Bar Association, Special Institute on International Mining and Oil & Gas Law, Development, and Investment*. Cartagena, Colombia.

Tilstone, G. H., Peters, S. W. M., van der Woerd, H. J., Eleveld, M. A., Ruddick, K., Schönfeld, W., Krasemann, H., Martinez-Vicente, V., Blondeau-Patissier, D., Röttgers, R., Sørensen, K., Jørgensen, P. V. & Shutler, J. D. (2012). Variability in specific-absorption properties and their use in a semi-analytical ocean colour algorithm for MERIS in North Sea and Western English Channel Coastal Waters. *Remote Sensing of Environment* 118(0): 320-338.

Tockner, K., Malard, F. & Ward, J. V. (2000). An extension of the flood pulse concept. *Hydrological Processes* 14(16-17): 2861-2883.

Tudesque, L., Grenouillet, G., Gevrey, M., Khazraie, K. & Brosse, S. (2012). Influence of small-scale gold mining on French Guiana streams: Are diatom assemblages valid disturbance sensors? *Ecological Indicators* 14(1): 100-106.

USGS (2013a). Earth Explorer. *http://earthexplorer.usgs.gov accessed in Sep, 2013.*

USGS (2013b). Using the USGS Landsat 8 Product. *https://landsat.usgs.gov/Landsat8_Using_Product.php accessed in Sep, 2013.*

Utermöhl, H. (1958). Zur Vervollkommung der quantitative Phytoplankton - Methodik. *Mitteilungen der Internationalen Vereinigung für Theoretische und Angewandte Limnologie* 9: 1-38.

Veiga, M. M. (1997). Mercury in Artisanal Gold Mining in Latin America: Facts, Fantasies and Solutions. Vienna: UNIDO.

Vermote, E. F., Tanre, D., Deuze, J. L., Herman, M. & Morcette, J. J. (1997). Second Simulation of the Satellite Signal in the Solar Spectrum, 6S: an overview. *Geoscience and Remote Sensing, IEEE Transactions on* 35(3): 675-686.

Wang, J.-J., Lu, X. X., Liew, S. C. & Zhou, Y. (2009). Retrieval of suspended sediment concentrations in large turbid rivers using Landsat ETM+: an example from the Yangtze River, China. *Earth Surface Processes and Landforms* 34(8): 1082-1092.

Wang, M. & Shi, W. (2007). The NIR-SWIR combined atmospheric correction approach for MODIS ocean color data processing. *Optics Express* 15(24): 15722-15733.

Wang, Y., Xia, H., Fu, J. & Sheng, G. (2004). Water quality change in reservoirs of Shenzhen, China: detection using LANDSAT/TM data. *Science of the Total Environment* 328(1-3): 195-206.

Wet Labs, I. (2013).Spectral absorption and attenuation sensor (ac-S) user's guide. Vol. 1, 33 Philomath, OR, USA.

WRB/FAO (1998). *World reference base for soil resources.* Rome: International Soil Reference and Information Centre, ISRIC.

Appendix A – Thematic map of ASGM in Tapajós Region

File attached on the e-mail ("Appendix_A_ASGM_Map.pdf").

Small-scale gold mining (ASM) in the Tapajós Gold District

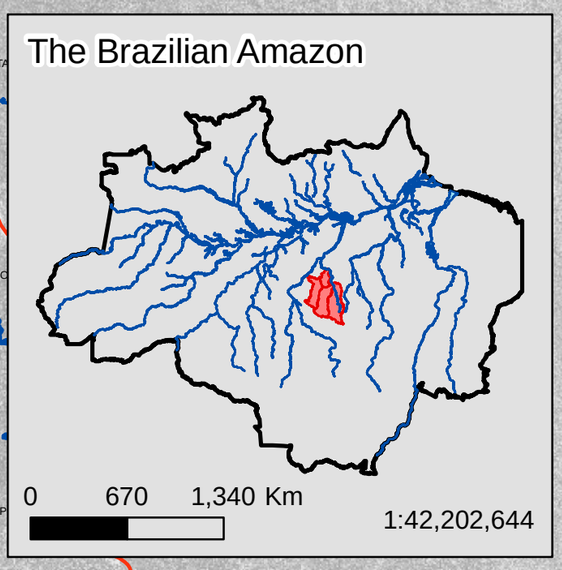

C) CUIU-CUIU AREA (Crepori River)

A) MARUPA RIVER AREA

B) CREPORIZÃO AREA

D) SURUBIM RIVER AREA (Novo River)

F) TOCANTINS AREA

E) PALITO AREA (Novo River)

Tocantins

Crepori

Novo

Jamanxim

Legend

- Mining (Garimpos)
- Roads
- River network
- Overflight (Photos)
- Gold Mining District
- Sub-basin
- Water mass
- GOLD MINING (km2)
  - 1973
  - 1993
  - 2012

Elevation (m)

90-120m, 121-150, 151-180, 181-210, 211-240, 241-270, 271-300, 301-330, 331-360, 361-390, 391-420, 421-450, 451-480, 481-510

1:908,534

0 15 30 60 Km

58°0'0"W 57°0'0"W 56°0'0"W 55°0'0"W

6°0'0"S 7°0'0"S 8°0'0"S 9°0'0"S